Institut für Physik **Universität Potsdam**

Fractal Fourier spectra in dynamical systems

Habilitationsschrift

der Mathematisch-Naturwissenschaftlichen Fakultät
der Universität Potsdam

vorgelegt von

Michael Zaks

Potsdam, August 2001

Foreword

Fourier analysis has long been a traditional tool in physics and other natural sciences. Usually, the distinction is made between the discrete (atomic, pure-point) and absolutely continuous spectra. Recently it became clear that spectral measures which belong to neither of these two classes but are supported by fractal sets, should not be viewed as exotic mathematical objects: examples of such processes, neither ordered nor strongly irregular, were detected in different physical situations. Several of such situations are described below; it is shown that temporal dynamics with fractal (singular continuous) power spectra can be found at virtually all levels of mathematical modeling of the real world: from partial differential equations to ordinary differential equations and further to mappings and symbolic sequences.

The first chapter demonstrates examples of dynamics with fractal sets of singularities in power spectra; they include certain dissipative flows as well as one-dimensional mappings and symbolic sequences related to these flows. Analysis shows that two basic mechanisms can be responsible for this phenomenon: the special geometry of the attracting set and the divergence of return times near the saddle point which belongs to the attractor.

Singular continuous power spectra are multifractal. In Chapter 2 the formalism of mutifractal analysis is applied to spectral measures of symbolic sequences built with the help of substitutions or concatenations. Exact algebraic expressions for generalized fractal dimensions of the spectral measure of the Thue-Morse sequence are obtained.

Divergence of return times can be a reason for the discrepancy between the spectral properties of the continuous flows and the Poincaré maps of these flows. In Chapter 3 this discrepancy between geometrical and dynamical characteristics is discussed, and a method is proposed which efficiently incorporates the information about return times into symbolic dynamics.

In Chapter 4 it is demonstrated that fractal power spectra can be found even in two-dimensional autonomous systems, namely in flows on 2-tori with points of equilibrium and irrational rotation numbers. As well as in the preceding Chapter, in this case continuous evolution can be reduced to symbolic dynamics; however due to unusual superexponential character of scaling of orbital returns, the different formalism should be applied.

Examples discussed in Chapter 5 refer to the situation in which phase space is a physical domain filled with fluid, and phase trajectories are orbits of tracer particles which move along the streamlines of a steady viscous flow. It is shown that for the observables built with the help of such tracers, presence of stagnation points in flow patterns can be a reason for the onset of fractal power spectra .

The listed examples of Fourier spectra which include only the singular con-

tinuous component, are restricted to purely deterministic dynamical systems. Nevertheless, as demonstrated in Chapter 6, the traces of multifractality of spectral measure can be detected also in the datasets of noisy origin. Influence of noise on the symbolic dynamics is illustrated with the help of the exactly solvable model of random binary substitutions.

Presentation of results is based on the papers [49], [57] and [77], [82], [122], [65], [123] and [124].

Acknowledgements

Results which constitute this thesis, were obtained during my work in the Max-Planck Arbeitsgruppe "Nichtlineare Dynamik" and in the Department of Nonlinear Dynamics at the University of Potsdam. I am much obliged to Arkady Pikovsky who introduced me to singular continuous spectra, and to Jürgen Kurths who maintains the creative atmosphere in the group, enabling the optimal research conditions. I am grateful to my colleagues from the department for friendly discussions and useful advice. Research activities were supported by Max-Planck Society.

Contents

Chapter 1

Singular continuous spectra in dissipative dynamics

1.1 Introduction

The dynamics of nonlinear systems may be described by means of different characteristics. One of the classical (and lately shadowed by more elaborate tools like Lyapunov exponents, dimensions, singularity spectra, etc.) ways to characterize the dynamics of the observable $f(t)$ is to compute its normalized autocorrelation function

$$C(\tau) = \frac{\langle\, f(t)f(t+\tau)\,\rangle - \langle f(t)\rangle^2}{\langle\, f^2(t)\,\rangle - \langle f(t)\rangle^2} \tag{1.1}$$

where averaging over time and/or the respective set of initial conditions is assumed. The dependence $C(\tau)$ provides the quantitative estimate of the system's ability to return to the same states after regular intervals of time [1, 2, 3, 4]. Usually, non-chaotic systems are well-correlated: the correlation function of the periodic motion reaches unity at all integer multiples of the basic period, whereas in the case of the quasiperiodic motion with an irrational ratio of frequencies, the largest peaks correspond to the times proportional to the denominators of successive rational approximations to this ratio, and the amplitudes of these peaks asymptotically approach 1. On the other hand, the eventually (not necessarily monotonically) decaying autocorrelation function of the chaotic motion reflects its property to forget the details of the initial state. As an intermediate stage one may imagine some "not perfectly regular" or "not entirely chaotic" motion for which the correlation function would be everywhere (except for $\tau = 0$) separated from 1, but at the same time would not entirely decay, displaying peaks of finite height for arbitrarily large values of τ and thus disclosing the ability of the system to remember "vaguely" its previous history.

Owing to the duality between the autocorrelation function and the Fourier power spectrum, the same statements can be retold in terms of the latter. For both periodic and quasiperiodic processes the Fourier spectrum is obviously composed of discrete delta-peaks only; in the former case the peaks are well separated whereas in the latter they are typically dense. The spectrum of the chaotic motion is marked by the presence of a continuous component. In most of

the known examples this component is absolutely continuous with respect to the Lebesgue measure (albeit some local singularities are possible, like in the case of $1/\omega$ spectrum), but in principle it may also be singular, i.e. be concentrated on a set of Lebesgue measure zero. This singular component might be viewed as some remnant of the discrete ordered-state spectrum in the following way: the response at the frequency corresponding to a singularity (such values must be dense in the spectrum), although not mighty enough to produce a delta-peak, is substantially stronger than in the immediate neighborhood. Therefore the singular continuous spectra occupy some intermediate position between the spectra of the well-ordered processes and those of the fully chaotic ones.

Singular continuous spatial spectra have been recently reported for the distributions of particles in systems with incommensurate scales[5, 6, 7]. They are also known to appear in quantum systems with quasiperiodic potentials[8] and quasiperiodic external forcing[9, 10]. Recently the singular continuous spectra have been observed in dissipative systems with quasiperiodic external forcing, where so-called "strange nonchaotic attractors" (sets which, like chaotic attractors, are not manifolds, but, contrary to them, are characterized by non-positive Lyapunov exponents) appear[11, 12]. However, to our knowledge no examples of this kind were reported for the conventional autonomous continuous-time dissipative systems.

In this Chapter we show that singular continuous spectra appear in the autonomous system of three ordinary differential equations [13] which resembles very much the Lorenz equations. After reviewing the basic properties of correlations and spectra in section 1.2, we describe the system in section 1.3 and present the data which show that singular continuous spectra can be observed at the accumulation points of the bifurcation scenarios in which the more and more complicated homoclinic orbits of the saddle points are progressively formed and destroyed. Although the scenarios themselves have been studied extensively [13, 14, 15, 16, 17], the related unusual correlation properties seem to have been overlooked.

It turns out, that in systems of this kind one encounters at least two different mechanisms, of which each one taken alone already supplies the singular continuous spectrum. One of them is due to the special symmetry (which may either be present or not) of the bifurcation scenario as expressed through the appertaining renormalization rules; as a consequence already the Fourier spectrum produced from the symbolic code of the corresponding orbit displays the required features. The simplest example of such a code is the so-called Thue-Morse [18, 19] sequence, for which there exists a rigorous proof of the singularity of the spectral measure. The other, more general mechanism producing a singular continuous spectrum, requires no symmetry and is associated with the logarithmic divergence of the return times for the trajectories approaching the homoclinicity. In physical language, variation of return times is tantamount to the phase modulation of the process. The corresponding mathematical model - the so-called special flow - is analyzed in section 1.4.

A curious and highly unusual peculiarity of the considered processes is a seeming discrepancy between the continuous flow and its discretization obtained with the help of the Poincaré mapping on a proper surface. As a kind of a counterexample to the conventional belief that the mapping mimics all the dynamical features of the flow, we present and discuss a situation in which the power spectrum of the attractor for the ODE system is singular continuous whereas the

Poincaré mapping yields a discrete spectrum. Another example demonstrates different spectral properties of return mappings obtained for two variables in the very same process: the power spectrum is singular continuous for one of them and discrete for the other one.

1.2 Basic properties of correlations and spectra

In this section we recall some facts about correlations and spectra (see [20, 21]). The autocorrelation function (1.1) can be represented as a Fourier transform of the spectral measure $\mu(\omega)$:

$$C(t) = \int e^{-i2\pi\omega t}\, d\mu(\omega). \tag{1.2}$$

In general, the spectral measure can be decomposed into the pure point and the continuous component (the possibilities for their simultaneous presence in the spectrum of a continuous-time dynamical system are discussed e.g. in [22]). In its turn the latter part can be further represented as a sum of the absolutely continuous, and the singular continuous components: $\mu = \mu_{p.p.} + \mu_{a.c.} + \mu_{s.c.}$. In the physical language, the pure point component is a set of delta-functions (discrete spectrum), while the absolutely continuous component has a spectral density (which is usually called power spectrum). The singular continuous component unites all what remains after both the pure point and the absolutely continuous components are removed, it sits on a set of zero Lebesgue measure, but is weaker than delta-peaks. To evaluate the intensity of the discrete spectrum it proves useful to introduce the averaged squared correlation function as (we assume that the time is discrete, a generalization to the continuous time is straightforward):

$$C_{\rm int}(t) = \frac{1}{t}\sum_{\tau=0}^{t-1} |C(\tau)|^2. \tag{1.3}$$

According to Wiener's lemma (see[20, 21]), the total intensity of the discrete component of the spectrum is $C_{\rm int}(\infty)$. From the other side, a necessary condition for the spectrum to be absolutely continuous is the decay of correlations:

$$\lim_{t\to\infty} C(t) = 0. \tag{1.4}$$

Hence, calculation of the autocorrelation function allows one (at least in simple cases) to detect singular continuous spectrum. Thus the power spectrum should be singular continuous if $C_{\rm int}(t)$ tends to 0 for large t, while $C(t)$ does not: the former requirement ensures the absence of the discrete component whereas the latter precludes the presence of the absolutely continuous one. We will make use of these criteria in our numerical studies below.

Recently it has been shown that the law of decay of the averaged squared correlation function (1.3) is related to the correlation dimension D_2 of the spectral measure μ [23, 24, 25]:

$$C_{\rm int}(t) \sim t^{-D_2}. \tag{1.5}$$

Indeed, one can expect that for an absolutely continuous spectral measure having dimension 1 the sum in (1.3) typically converges, so $C_{\rm int}(t) \sim t^{-1}$ and $D_2 = 1$, while for a discrete spectrum (zero dimension) $C_{\rm int}$ does not decay and relation (1.5) gives $D_2 = 0$.

1.3 The ODE system, its attractors and their spectra

To demonstrate the action of the mechanisms which produce "intermediate" spectral and correlation properties we use the 3-rd order ODE system which is reminiscent of the Lorenz equations:

$$\begin{aligned} \dot{x} &= \sigma(y-x)+\sigma Dy(z-R) \\ \dot{y} &= Rx-y-xz \\ \dot{z} &= xy-bz+ax \end{aligned} \tag{1.6}$$

but may have different scenarios of transition to chaos. This system (see [13] for the derivation and more detailed description) models the averaged thermal convection in the fluid layer subjected to the transversal high-frequency oscillations of gravity. Vibrations are known to suppress the small-scale fluid motions[26], which makes physically plausible the Lorenz-like truncation to one mode (x) for the velocity field and two modes (y and z) for the temperature distribution. Here σ denotes the Prandtl number of the fluid, R stands for the Rayleigh number (normalized to its critical value in the absence of vibrations), $b = 4\alpha/(1+\alpha^2)$ is the geometrical parameter determined by the wavenumber α of the convective pattern. The additional (with respect to the Lorenz model) term in the first equation is proportional to the "vibrational parameter" D, given by the squared ratio of the amplitude of the modulation to its frequency; another modification is breaking the symmetry $(x, y) \Leftrightarrow (-x, -y)$ by means of introduction of the term ax into the 3-rd equation.

Similarly to the unperturbed Lorenz equations, the transition to chaos in the equations (1.6) follows the formation of the homoclinic trajectories to the trivial steady state $x = y = z = 0$; in the parameter domain $D < R^{-1} - R^{-2}$ the latter is a saddle-point with three real eigenvalues $\lambda_3 < \lambda_2 < 0 < \lambda_1$. Whereas in the Lorenz case the positive eigenvalue is larger than the absolute value of the leading (closest to zero) negative one, here the homoclinic bifurcation can be encountered also in the parameter domain

$$\frac{1}{R} - \frac{1}{R^2} - \frac{b(\sigma+1-b)}{\sigma R^2} < D < \frac{1}{R} - \frac{1}{R^2} \tag{1.7}$$

where $\lambda_2 + \lambda_1$ is negative. This means that, as opposed to the Lorenz system, in the vicinity of the saddle point the contraction prevails over the expansion, and the destruction of homoclinic connections should produce not the unstable Ω-set [27, 28] but stable closed orbits. The further evolution through more and more complicated periodic states eventually leads to the emergence of the chaotic attractor; the structure of the parameter space is enormously rich, with uncountably many different routes to chaos [15, 16, 17]. We will focus below on two particular scenarios which seem to be the best-suited for the illustration of the unusual spectral and correlation properties. In our computations we will fix the "canonical" Lorenz parameter values $\sigma = 10$ and $b = 8/3$.

1.3.1 Symmetrical case

Let us fix $a = 0$, and increase R keeping D in the domain (1.7). Owing to the symmetry $(x, y) \Leftrightarrow (-x, -y)$ the homoclinic bifurcation results in gluing of two

mutually symmetrical stable closed orbits into a single one (Fig.1.1(a)-1.1(b)). The further sequence consists of the alternating symmetry-breaking bifurcations and subsequent homoclinic gluings of periodic orbits (Fig.1.1(c)-1.1(d)).

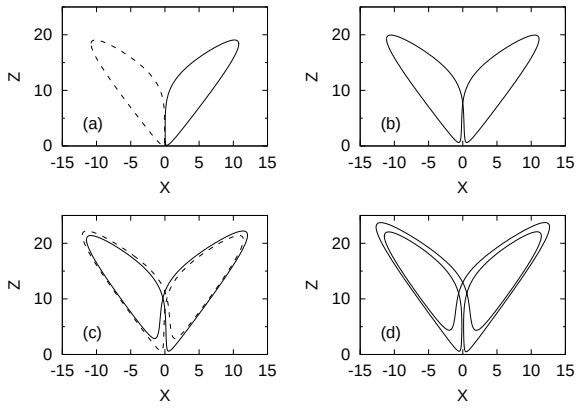

Figure 1.1: A sketch of the homoclinic-doubling bifurcation in the system(1.6): two symmetrical stable cycles (a) glue into a homoclinic orbit, which produces stable symmetrical cycle (b); this cycle loses its symmetry with creation of two 2-loop stable cycles (c), which glue and produce a "period-4" stable cycle (d).

The number of loops of the attracting periodic orbit is doubled at each homoclinic bifurcation (this is not, however, the period-doubling in the usual sense, since the time period is infinite at the bifurcation point), and the whole bifurcation sequence is converging at the universal geometric rate. The renormalization treatment of the corresponding one-dimensional discontinuous map [14, 13] shows that the convergence rate (along with the other scaling characteristics of this hierarchical process) is entirely determined by the so-called saddle index: the ratio of the eigenvalues $\nu = -\lambda_2/\lambda_1$. Projection of the resulting symmetric attractor at the accumulation point of homoclinic bifurcations for $\nu = 2.0$ can be seen in Fig.1.2. Further increase of R leads to the onset of chaos.

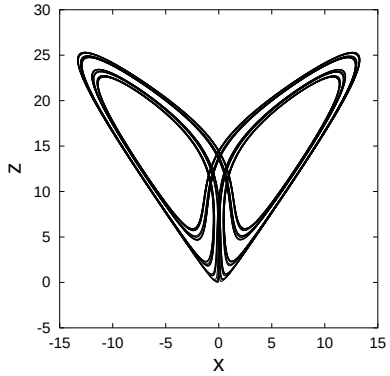

Figure 1.2: View of the attractor of the system(1.6) at the point of transition to chaos through homoclinic-doublings. $R = 15.8237366768028\ldots$, $D = 0.052634923195\ldots$ The Cantor structure of the attractor is clearly seen.

We now consider the spectral and correlation properties of the system (1.6) at the transition point. The computed autocorrelation functions for the variables x and z on this attractor are presented in Fig.1.3. It can be seen that their shape fulfills the conditions for the spectrum to be singular-continuous: the correlations themselves do not decay, so the condition (4) is not satisfied; on the other hand, the averaged squared correlation function decays as a power law. The plotted data display a remarkable feature: the values of time corresponding to the largest peaks of $C(t)$ form a geometrical progression: the ratio of the times is approximately 2. This factor corresponds to the fact that the attractor is created through homoclinic doublings. However, unlike in the case of the usual period doublings, the level of correlation remains less than 0.5.

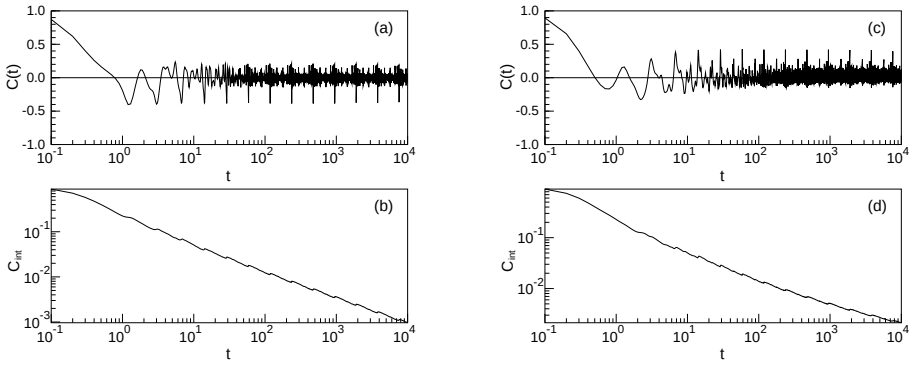

Figure 1.3: Autocorrelation functions for the variables x (a) and z (c). Note the logarithmic scale of the time axes. This shape with arguments of the peaks forming a geometrical progression, is typical for processes with singular continuous spectra. The integrated squared correlation functions (1.3) are presented in (b) and (d) respectively.

The spectral sums S_n for the same attractor, which were computed with the use of 2^n-points FFT (at a sampling rate 0.1 in the units of dimensionless time of (1.6)) and subsequent averaging for many realizations, are presented in Fig.1.4. One notices both the "fractalization" of the spectrum with the growth of n and the apparent self-similarity in the low-frequency part of the power spectrum: $S_n(\omega) \propto S_{n+1}(\frac{\omega}{2})$ (Fig.1.5).

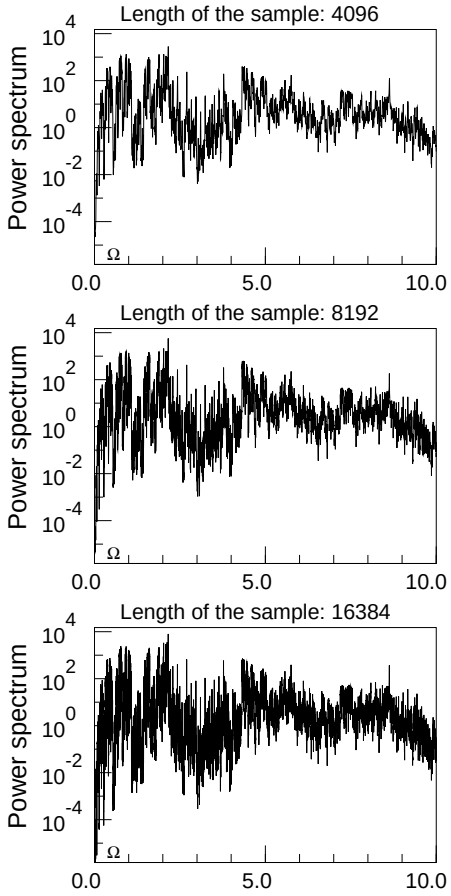

Figure 1.4: Power spectrum of the variable x, calculated for different numbers of points in the sample $N = 2^n$. With the increase of N the spectrum becomes more scarred: both the peaks and the depressions grow.

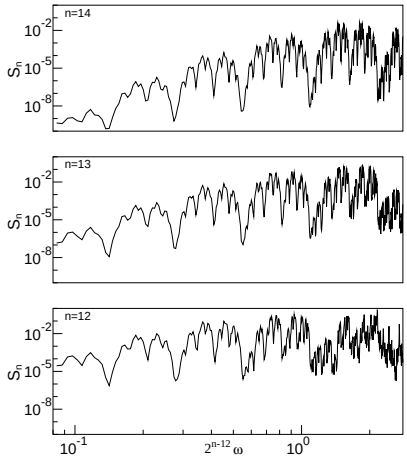

Figure 1.5: The low-frequency parts of the spectra of Fig.1.4, redrawn in scaled coordinates to show self-similarity.

A common way of reduction of a continuous-time dynamical system to a discrete one is to consider the Poincaré map on some surface. For the equations (1.6) it is convenient to introduce this surface near the saddle as depicted in Fig.1.6.

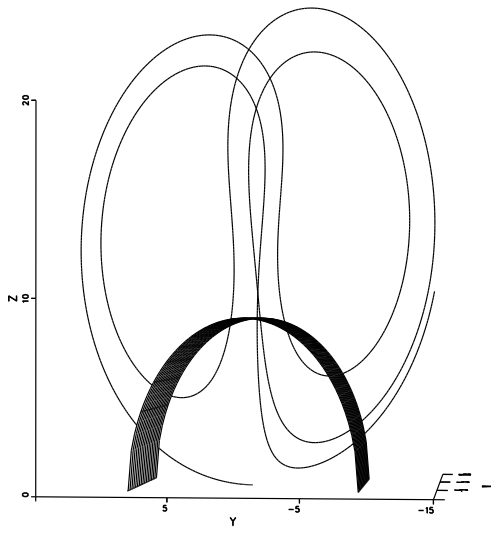

Figure 1.6: The sketch of the surface of section (the cylinder $z^2 + y^2 = 81$) used to construct the Poincaré map in the system (1.6).

Because of the strong volume contraction the resulting Poincaré map can be viewed as quasi-one-dimensional, see Fig.1.7. The mapping for the variable x (Fig.1.7a) is symmetric and discontinuous due to the symmetry of the underlying ODE system; in case of the variable z (Fig.1.7b) which does not participate in the symmetry transformation, the mapping is continuous and has a minimum. Owing to the Cantor-like structure of the attractor, the points do not fill the lines, but these can be easily interpolated [14, 13].

Calculations of the correlation function $C(n)$ (where the discrete time variable n stands for the number of intersections with the secant) for the corresponding series of the section coordinates, demonstrate that while the spectrum for the values of x remains singular-continuous (Fig.1.8(a)), the spectrum for z is discrete (Fig.1.8(c)) precisely in the same way as it should be for the logistic mapping at the Feigenbaum point[29]. This discrepancy between the properties of two coupled variables stemming from the same dynamical system is discussed in the Section 1.3.3 below; detailed analysis of the situation, including the proper symbolic description, is performed in Chapter 3.

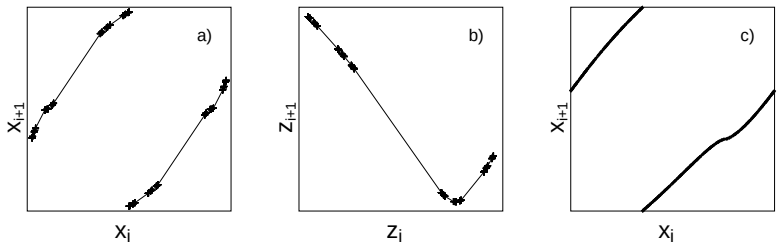

Figure 1.7: Poincaré maps for the variables x (a) and z (b), obtained with the surface of section Fig. 1.6 for the attractor Fig.1.2 (the variable x is additionally projected on a line transversal to the stable manifold of the saddle). The points of the attractor are marked with crosses which are connected by interpolation curves. The mapping (c) corresponds to the attractor Fig.1.9, here a quasiperiodic orbit is dense on the interval.

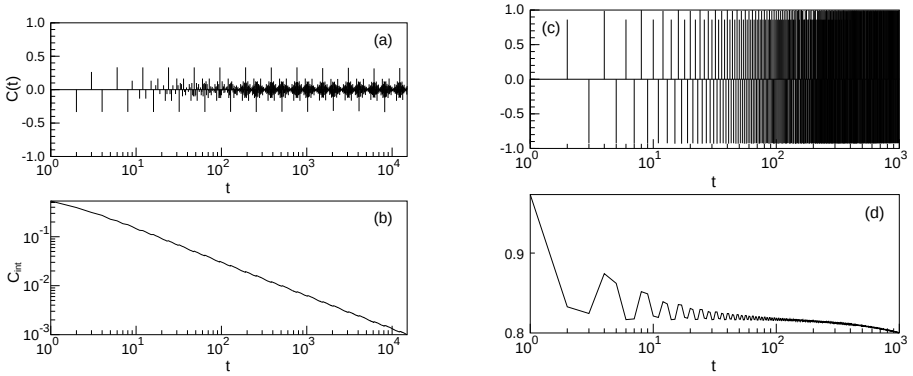

Figure 1.8: Correlation function for the discrete sequences x_n (a,b) and z_n (c.d). While the power spectrum of x_n remains singular continuous, the power spectrum of z_n is discrete.

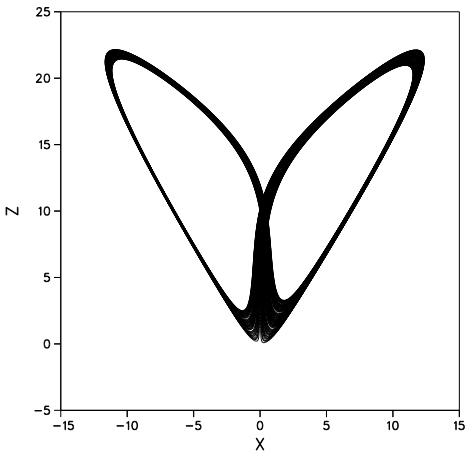

Figure 1.9: The view of the attractor of the system(1.6) at the point of transition to chaos through "quasiperiodicity"

1.3.2 Asymmetrical case

Of many different scenarios, which are possible for $a \neq 0$ we take the one which resembles very much the transition to chaos through quasiperiodicity. Without going into details (see [15, 16, 17, 30]) we should only mention that in the proper parameter domain one can define the "rotation number" ρ, which for the closed periodic orbit is the ratio of the number of loops in the half-space $x > 0$ to the entire number of the loops. For the non-closed orbit ρ is the ultimate "proportion" of these loops, i.e. the limit of the respective ratio for $t \to \infty$. The parameter space can be separated into the "subcritical" domain for which ρ is independent of the initial conditions, and the supercritical domain where orbits with different values of ρ may coexist and one should speak rather about the rotation intervals. These two domains are separated by a "critical" surface. For the parameter plane the latter is just a curve, and the subcritical domain is a union of the countable number of "resonant tongues" inside which ρ is rational and the continuum of curves which correspond to irrational values of ρ. This structure is reminiscent of the Arnold tongues for the circle mappings; however in our case all the tongues and all the irrational curves emanate from one and the same point; another difference is that at the edges of the tongues the periodic orbits are not necessarily coalescing via the tangent bifurcation, but may also disappear through the formation of the multi-turned homoclinic orbit.

Let us fix some irrational value of ρ and move on the parameter plane along the corresponding curve towards the critical line. The respective attracting set at the critical point of transition to chaos for the "reciprocal golden mean" rotation number $\rho = (\sqrt{5}-1)/2$ is presented at Fig.1.9; the parameter values $R = 14.148796861\ldots$, $D = 0.054334761974059106\ldots$, $a = -0.561287331738\ldots$ correspond to $\nu = 1.5$.

One sees that, in contrast to the Cantor-like attractor from Fig.1.2, this set looks dense on the transversal section. The Poincaré section resembles very much the critical circle map (with the only difference that the singularity is

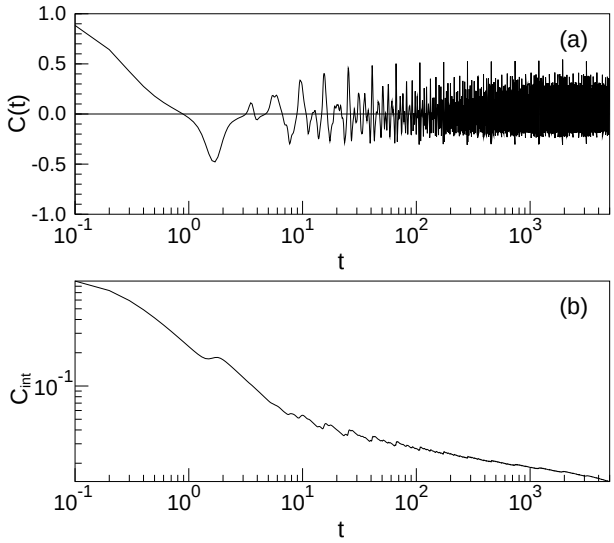

Figure 1.10: Autocorrelation functions for the variable x of the attractor Fig.1.9. $C(t)$ has a typical form for the case of singular continuous spectrum with peaks forming a geometrical progression. The factor of this progression is the golden mean, according to our choice of the rotation number.

generally not cubic, but has an order ν) [17, 30]; insofar as the rotation number is irrational, the attracting orbit is everywhere dense on the interval (Fig.1.7c). Correspondingly, the spectrum of the variable x_n discretized in this way, contains the pure-point component only. However the calculation of the autocorrelation function of the underlying continuous-time process $x(t)$ (Fig.1.10) demonstrates that its power spectrum is singular continuous.

1.3.3 Two mechanisms for the singular continuous spectrum

The numerical results presented above suggest that at least two distinct mechanisms are responsible for the appearance of singular continuous spectra.

1. The first mechanism is the one which ensures the singular continuous spectrum for the variable x in the symmetric case. Producing the same results for both the continuous flow and the sequence of the Poincaré sections, it obviously does not depend on the dynamical time properties of the process, and hence may be called the geometric mechanism. Not only the reduction to the mapping, but already the symbolic representation of the orbit of such mapping possesses the same spectral properties. Let us ascribe the symbol $L(R)$ to each loop in the half-space $x < 0$ ($x > 0$). On the symbolic language each homoclinic bifurcation is the concatenation (gluing) of some finite symbolic sequence with its mirror counterpart: the same sequence in which all R's are substituted by L's and vice versa. Thereby the scenario of the change of the attractor's code is

$$R \to RL \to RLLR \to RLLRLRRL \to \dots$$

The resulting infinite symbolic code which is obviously invariant under the transformation $R \to RL,\ L \to LR$, is known as the Thue-Morse sequence[18, 19]. From the mathematical literature it is known that this sequence has a singular continuous Fourier spectrum[21]; multifractal characteristics of its spectral measure will be investigated in Chapter 2 below. There exists a number of studies on the applications of the Thue-Morse sequence to different physical systems [31, 32, 33], however to our knowledge in all of these examples the sequence was prescribed externally – either as external forcing, or as a prepared pattern of the lattice. In our case this sequence appears as a result of the intrinsic dynamics of the system, which owes to the mirror symmetry of the original equations. The correlation and spectral properties of this symbolic code are readily transferred to the values of the Poincaré sections for the variable x and, finally, to the continuous process $x(t)$.

Along with the described scenario which yields the "pure" Thue-Morse sequence, one can follow in the parameter space certain other bifurcational sequences where the geometric mechanism is at work. We will briefly mention just two possibilities. For the general asymmetric case each intersection on the parameter plane of two curves corresponding to the formation of multi-looped homoclinic orbits, produces the pencil of lines marking the secondary homoclinic bifurcations [16, 17]. Let the symbolic codes of the primary multi-looped orbits be two words of some finite (and not necessarily equal) length l_1 and l_2 respectively, the first letter being R in one of them and L in the other. Since the codes of the new homoclinic orbits are obtained by concatenation of these two words, it is straightforward to re-define the coding rules: let us take two given words as the initial blocks and denote them by R and L respectively. Now one may trace the new sequence of homoclinic doublings (the corresponding orbits have $(l_1 + l_2)2^{n-1}$ loops) and locate at some distance its accumulation point, where the symbolic code of the attracting trajectory can be reduced to the conventional Thue-Morse form by the single symbolic renormalization.

The other example is provided in the symmetric case $a = 0$ by the sequences of "homoclinic m-tuplings", which converge to the parameter values where the symbolic code is invariant with respect to the substitution $R \to RL^{m-1},\ L \to LR^{m-1}$. For $m = 2$ one gets the scenario of homoclinic doublings described above, which provides the Thue-Morse code; symbolic sequences for the higher values of m also demonstrate singular continuous spectral properties, and this is immediately mirrored by the corresponding characteristics of the trajectories for the continuous flow (1.6).

It is noteworthy that one can find the Thue-Morse sequence even in a much simpler dynamical system: consider the symmetrical cubic mapping $x \to Ax(x^2 - 3)$. This mapping has three intervals of monotonicity: $x < -1$, $-1 < x < 1$ and $x > 1$, which provides the natural coding by symbols L, C, and R respectively. For the particular choice of the parameter $a = 0.9659413915688\ldots$ the stable orbit starting at the point $x = 1$ does not visit the central segment, and its symbolic coding which is composed of R's and L's only, is organized into the Thue-Morse sequence. No wonder that at this parameter value the Fourier spectrum of the attracting trajectory for the continuous cubic mapping is singular continuous (Fig.1.11).

2. The second mechanism which ensures the onset of singular-continuous spectra, is at work for the variable z in the symmetric case and for all the variables in the absence of symmetry. Here the discretized and the continuous-time

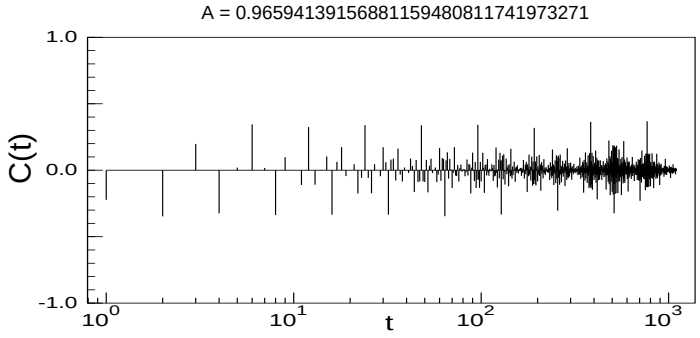

Figure 1.11: Autocorrelation function for the mapping $x \to Ax(x^2 - 3)$.

processes have qualitatively different spectra. The reason for the difference must lie in the properties of the return times between the consecutive Poincaré sections; therefore it is natural to call this mechanism the dynamical one. Indeed, the Poincaré map for the considered ODE system, as well as for the Lorenz equations, is singular: it is not defined at the intersection of the secant surface with the stable manifold of the saddle point. The behavior of return times is also singular: as the point of section approaches the stable manifold, the return time diverges logarithmically. As a result, one cannot speak about the characteristic return time (as it would be the case for period-doublings); insofar as the orbit should pass arbitrarily close to the saddle point, the return time may be arbitrary large. We conjecture that this singularity is responsible for the singular continuous nature of the spectrum. To support this conjecture we perform in the following section the analysis of the idealized dynamical system – the so-called special flow.

1.4 The special flow

In this section we intend to demonstrate that the logarithmic singularity of the return times alone provides the singular continuous spectrum. For this purpose we consider an idealized process, for which it is possible to separate properties of the Poincaré map and of the return times. The construction we use is a variant of the so-called special flow, typically used in studies of ergodic properties of continuous-time dynamical systems[20]. The special flow over the map $x \to f(x)$ of the interval $0 \le x < 1$ is defined as follows. Consider the piece of the plane $0 \le x < 1,\ 0 \le y < F(x)$. The trajectory starting from the initial point $x(0), y(0)$ is defined as

$$x(t) = f^n(x(0)), \quad y(t) = y(0) + t - \sum_{k=0}^{n-1} F(f^k(x(0))) \tag{1.8}$$

where integer n as a function of continuous time t is uniquely defined from the inequalities

$$\sum_{k=0}^{n-1} F(f^k(x(0))) \le y(0) + t < \sum_{k=0}^{n} F(f^k(x(0))).$$

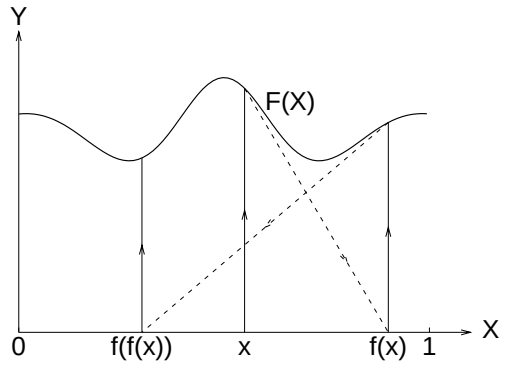

Figure 1.12: Geometric representation of the special flow construction

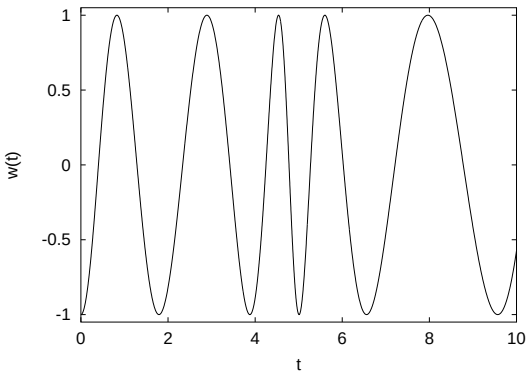

Figure 1.13: Process with pure phase modulation, generated by the special flow.

The geometrical representation of the special flow is the following (see Fig.1.12): a trajectory moves on the plane x, y upwards with unit velocity, until the value of y reaches the border $y = F(x)$, then the trajectory jumps to the point $(f(x), 0)$ and begins to move upwards again. One can see that the special flow has the map $x \to f(x)$ as the Poincaré map, and the return times are given by the function $F(x)$.

The variable x can be considered as the amplitude and the ratio $y/F(x)$ as the phase of the continuous-time dynamical process. The amplitude modulation is determined by the Poincaré map, while the phase modulation depends also on the properties of the return times $F(x)$. By choosing an observable which depends only on the phase, e.g. $w = \cos(2\pi y/F(x))$, we can select properties of the continuous dynamics that are connected with the distribution of the return times: for this observable the amplitude modulation vanishes (see Fig.1.13).

These properties are completely defined by the Poincaré map $x \to f(x)$ and by the function $F(x)$. We consider the two cases:
1) $f(x)$ is the logistic map at the point of transition to chaos[1]
2) $f(x)$ is a circle map with irrational rotation number.

[1]Although in real systems the Poincaré map is invertible, at the point of accumulation of period doublings it can be good approximated with a one-dimensional parabola-type mapping.

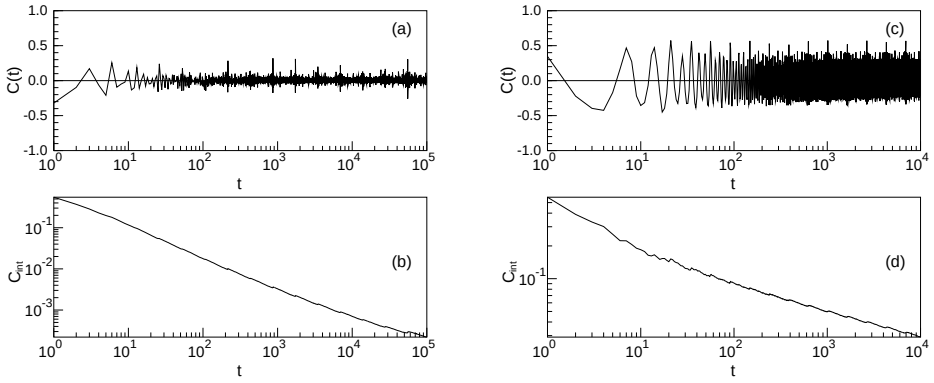

Figure 1.14: Autocorrelation functions for the processes with logarithmic singularities in return times constructed with the special flows over the logistic (a) and circle (c) maps. The corresponding averaged squared correlation functions (b) and (d) decay as powers of time, indicating the existence of singular continuous spectrum.

In both cases the spectrum of the Poincaré map of the variable x is discrete. While with a smooth function $F(x)$ the spectrum of the variable w remains discrete [34, 35], it can become continuous if F is singular. Von Neumann proved in [36] that in the second case a discontinuous $F(x)$ can generate a process with continuous spectrum. The mixing properties of the special flow when the function F has a logarithmic singularity $F(x) \sim -\log|x - x_0|$ were studied in refs. [37, 38], however to our knowledge, the characteristics of the Fourier spectrum have not been considered.

We have investigated numerically the correlation properties of the process $w(t)$ in the presence of a logarithmic singularity for the cases (1) and (2) described above (a renormalization group analysis of this problem is now in progress). The results are presented in Fig.1.14. They clearly demonstrate, according to the criteria discussed in section 1.2, that special flows with a logarithmic singularity have singular continuous spectra. It seems that for the circle map, where trajectories are dense on the interval, the location of the logarithmic singularity is irrelevant. For the Feigenbaum map the attractor is a Cantor set, so the singularity should not fall in a gap. In order to model the ODE system close to the homoclinicity, the singularity must be placed at the extremum of the map, and this point belongs to the Feigenbaum attractor.

Thus, consideration of special flows allows us to conclude, that a logarithmic singularity in return times can provide a singular continuous spectrum, even if the spectrum of the Poincaré map itself is discrete. For the system of ODEs considered above, this mechanism works for the variable z in the symmetrical case, and in general in the asymmetrical case.

1.5 Summary

In this chapter we have demonstrated that singular continuous spectra can be observed in certain autonomous dissipative dynamical system at the point of

transition to chaos. In the investigated ODE system we found two different mechanisms which are responsible for these spectra. The first mechanism, being purely geometrical, works equally well for both discrete-time and continuous-time dynamics; it is connected with the appearance of the particular symbolic code – the Thue-Morse sequence (or its generalizations). The second mechanism which owes to the dynamics of the return times, affects only the continuous-time systems, and is connected with singular phase modulation, when the process consists of pulses of different length. The amplitudes of the pulses are described by a corresponding Poincaré map and behave quasiperiodically (when the map is equivalent to a circle map with irrational rotation number) or almost periodically (when the map has the Feigenbaum-like attractor). The singular continuous spectrum appears, when the dependence of the duration of pulses on their amplitude has a logarithmic singularity. Such a singularity is present in the considered ODE system because the closure of the attractor includes the saddle point, in which neighbourhood the trajectories "stick" for a long time. As a consequence, the spectral properties of the continuous flow differ from those of the mapping. From the results of von Neumann [36] it follows that the singularity of phase modulation may be even weaker, in some cases a discontinuity in the dependence of return time on the amplitude is enough for the spectrum to be continuous. Presently, however, we do not have an example of an autonomous dynamical system, in which a discontinuity of return times is responsible for a singular continuous spectrum.

Chapter 2

On the generalized dimensions for the Fourier spectrum of the Thue-Morse sequence

2.1 Introduction

The Thue-Morse infinite binary sequence $\{M_j\}, (j = 1, 2, \ldots)$ is formed by two symbols (in our notation, 1 and -1) and can be obtained from the starting point $M_1 = 1$ by means of repetitive substitutions (inflations) according to the rule [18, 19]:

$$\begin{aligned} 1 &\rightarrow \quad 1 \quad -1 \\ -1 &\rightarrow \quad -1 \quad 1 \end{aligned} \tag{2.1}$$

Several equivalent definitions are possible, for instance, $M_j = (-1)^{k+1}$ where k is the sum of digits in the binary representation of j. Yet another definition (which we will exploit below) is based on concatenations. This goes as follows: given a symbolic string K_n of length 2^n we append to it the string $\overline{K_n}$ in which each symbol "1"of K_n is replaced by "–1" and vice versa; the recursion $K_{n+1} = K_n\overline{K_n}$ combined with the initial condition K_0=1 yields the Thue-Morse sequence.

With respect to a shift along the symbolic chain, the Thue-Morse sequence supports a unique translation-invariant ergodic probability measure [39]. Although organized by a simple deterministic rule, the Thue-Morse sequence is not periodic. The Fourier spectrum (in physical applications the term "structure factor" is frequently used) of the infinite chain is long known to be purely singular continuous [40, 21]: the spectral measure is neither atomic (discrete) nor absolutely continuous with respect to the Lebesgue measure, but is concentrated on a fractal set. This convenient combination of computational simplicity and intrinsic complexity turned the Thue-Morse sequence into a standard tool, widely exploited in the context of long-range ordering and disordering in one-dimensional patterns. To mention only a few recent applications, it was

prescribed as a governing law for the external force in a kicked quantum rotator [33, 41] and served as a ground state configuration for the classical lattice gas model [42] and Ising spin system with short interaction[43]. In the description of the critical phenomena for the aperiodic quantum Ising lattices [44, 45, 46] it dictated the constants of exchange coupling. Further, the Thue-Morse sequence played a role of a one-dimensional potential for the discretized Schrödinger equation in the study of the gaps distribution in the energy spectrum [31], and its singular spectra have been recovered in the diffraction patterns of the specially prepared GaAs-AlAs superlattice heterostructures [32, 47]; the latest advances in this direction are thoroughly discussed in [48] (where also the exhaustive list of appertaining references can be found). Finally, the Thue-Morse symbolic code of the attractor at the accumulation point of the sequence of "homoclinic doublings" in symmetrical flows with saddle equilibria [14, 13] was recently understood as one of the mechanisms responsible for the generation of singular continuous spectra in continuous dissipative systems [49].

2.2 Correlation dimension of the Fourier spectrum

The multifractal properties of the Fourier spectrum for the Thue-Morse sequence have been investigated by Godrèche and Luck [50], who determined numerically the generalized dimensions D_q and the singularity spectrum $f(\alpha)$ for the spectral measure (see also a recent application of the wavelet technique in [51]). Apparently, the box-counting dimension D_0 equals 1 (the fractal set which carries the spectral measure, is dense); estimation of D_q for the general case $q \neq 0$ requires extensive numerical computations. In this section we explicitly calculate the value of the correlation dimension D_2 for the spectral measure. In doing this, we utilize the exact relation $C_{\rm int}(T) \sim T^{-D_2}$ derived in [23, 24, 52] which binds the properties of the (integrated) autocorrelation to the value of D_2. Thus the direct evaluation of D_2 from the Fourier spectral data can be replaced by the estimation of the decay rate for the integrated autocorrelation; as shown below, the self-similarity of the Thue-Morse sequence allows to determine this rate analytically (note that autocorrelation function generically does not depend on the choice of observable, so we simply put $x_j = M_j$).

By construction the Thue-Morse sequence is invariant under the substitution (2.1) and under the inverse operation of "binary decimation": crossing out each even symbol. This is reflected in the recurrence properties of the correlation function: $\sum_j M_j M_{j+t} = \sum_j M_j M_{j+2t}$ and, respectively,

$$C(2t) = C(t). \tag{2.2}$$

This ensures repetitive non-decaying peaks for arbitrary large values of t (and thus prohibits the spectrum to be absolutely continuous with respect to the Lebesgue measure: the necessary condition of such continuity is the decay of correlations for $t \to \infty$ [53, 20]). The analogous recurrence relation for the odd argument values follows from the invariance of the infinite sum $\sum_j M_j M_{j+2t+1}$ under the binary decimation. After decimation, the odd symbols remain unchanged whereas the even ones are replaced by their counterparts (1 by -1 and

vice versa), hence the pairwise products acquire the opposite sign. Consequently,

$$C(2t+1) = -\frac{C(t)+C(t+1)}{2}. \tag{2.3}$$

The relations (2.2, 2.3) combined with "initial condition" $C(0) = 1$ allow one to obtain the exact values of $C(t)$ for any value of t. They ensure that the inequality $|C(t)| \leq \frac{1}{3}$ holds for all t (naturally, except for $C(0)$=1).

Consider now the recurrences between the sums $S_n \equiv \sum_{n+1}^{2n} C^2(t)$ for $n = m, 2m, 4m, \ldots$, m - arbitrary positive integer. On applying (2.2) and (2.3) to the even and odd terms in S_{4m} respectively, we obtain

$$S_{4m} = S_{2m} + \frac{S_{2m}}{2} + \frac{1}{2}\sum_{2m}^{4m-1} C(t)C(t+1) \tag{2.4}$$

Denoting the last term in the right hand size of (2.4) by Π_{2m} and transforming it with the help of (2.2, 2.3), we arrive at

$$\Pi_{2m} = -\sum_{m}^{2m-1} \left(C^2(t) + C(t)C(t+1)\right). \tag{2.5}$$

Thus we are left with the two coupled linear recurrences

$$\begin{aligned} S_{2j} &= \frac{3}{2}S_j + \frac{1}{2}\Pi_j \\ \Pi_{2j} &= -S_j - \Pi_j \end{aligned} \tag{2.6}$$

Introducing further the variables $\kappa_j \equiv S_{2j}/S_j$ and $\xi_j \equiv \Pi_{2j}/S_j$ and noticing that the equality $\kappa_j(\xi_j + 2) = 2$ is independent of j, we end up with a simple one-dimensional mapping

$$\kappa_{2j} = \frac{1}{\kappa_j} + \frac{1}{2} \quad . \tag{2.7}$$

which in the domain $\kappa > 0$ (only this is of relevance, since $S_j > 0$) has the globally attracting fixed point $\kappa_* = \frac{1+\sqrt{17}}{4}$=1.280776406.... Therefore, for large j holds: $S_{m2^j} \propto (\kappa_*)^j S_m$. Let us turn now to the integrated autocorrelation $C_{\rm int}(T)$. Since this function is by definition a ratio of two monotonous functions of T, it is easy to see that, irrespectively of T, the inequality

$$\frac{C_{\rm int}(2T)}{2} < C_{\rm int}(t) < 2C_{\rm int}(T) \tag{2.8}$$

holds for any t from the interval $(T, 2T)$. Obviously, for the values $T = 2^n m$ under large n

$$C_{\rm int}(T) = \frac{1 + \sum_{j=1}^{n} S_{m2^j}}{m2^n} \;\propto\; T^{\frac{\log \kappa_*}{\log 2} - 1} \quad . \tag{2.9}$$

In combination with (2.8), this ensures the power-law decay of $C_{\rm int}(T)$. According to Wiener [53], vanishing of $C_{\rm int}(\infty)$ implies the absence of the discrete component in the spectrum. Consequently, the spectral measure for the Thue-Morse sequence is purely singular continuous, and its correlation dimension equals:

$$D_2 = 1 - \frac{\log \kappa_*}{\log 2} \;=\; 3 - \frac{\log(1+\sqrt{17})}{\log 2} \;=\; 0.64298136\ldots \tag{2.10}$$

Cf. the values of other generalized dimensions: the capacity D_0=1 and the information dimension D_1=0.730 (numerical value).

The fact that the relation (2.9) is independent of m, implies that the prefactor before T^{1-D_2} on the right hand size of (2.9) must tend to a periodic function of the logarithmic variable $\log T/\log 2$. Our numerical estimates, however, show the influence of this time-dependence to be rather weak: the prefactor oscillates log-periodically between 0.75 and 0.77.

The same procedure can be implemented for other symmetrical substitution sequences, for instance, for the m-tuplings: $A \to AB^{m-1}$, $B \to BA^{m-1}$. Obviously, the case m=2 yields the Thue-Morse sequence. For m=3 the autocorrelation function obeys the recurrences

$$C(3t) = C(t), \;\; C(3t+1) = -\frac{C(t+1)}{3}, \;\; C(3t+2) = -\frac{C(t)}{3}$$

and the correlation dimension of the spectral measure equals $3-\frac{\log 11}{\log 3}$=0.8173.... For m=4 one has:

$$C(4t) = C(t), \;\; C(4t+1) = -C(4t+3) = \frac{C(t)-C(t+1)}{4}, \;\; C(4t+2) = 0$$

and $D_2 = \frac{5}{2} - \frac{\log(3+\sqrt{41})}{\log 4}$=0.8834.... Higher values of m can be treated in a similar way.

We expect that the knowledge of recurrent properties for the autocorrelation function of substitution symbolic sequences (the obvious (2.2) is commonly used, but the less evident relations like (2.3) seem to be overlooked) and that of the exact values like (2.10) can be helpful in answering many subtle questions which arise in the context of one-dimensional "quasicrystals" in substitutional systems with various bond-length ratios [54, 55], extended electronic states in one-dimensional lattices [56], and kicked quantum systems with corresponding potentials [33, 41].

2.3 Spectral measure

Since the Thue-Morse sequence plays a prototypic role for weakly aperiodic systems, the exact knowledge of the characteristics of its spectral properties is of especial methodical interest. In the previous section we utilized the relation between the decay rate of the integrated autocorrelation function and the correlation dimension D_2 of the spectral measure [23, 24] to obtain the exact value of the correlation dimension D_2 for the spectral measure of the Thue-Morse sequence: $D_2 = 3 - \log(1+\sqrt{17})/\log 2 = 0.64298\ldots$ [57]. Below, we will use a different approach and express the values of the generalized dimensions D_q for integer q through the leading eigenvalues of the appertaining $q \times q$ matrices. Further, we generalize the results of [23, 24] by relating D_q to the growth rates of the higher products of the values of the autocorrelation function. The case of the information dimension D_1 does not conform to this scheme; we present the series which allows to calculate it to arbitrary precision.

A generic observable built from the Thue-Morse sequence should attain only two values. Therefore, the spectral properties do not depend on the choice of the observable, and we select the most convenient one: the value

of $M_j = \pm 1$ itself. Let us take the value ω ($0 \le \omega \le 1$) and consider the partial Fourier sums formed by the first $l_n = 2^n$ symbols of the sequence: $\sigma_n(\omega) = \sum_{j=1}^{2^n} M_j \mathrm{e}^{2\pi i j\omega}$, and the finite-length approximations to the power spectrum $S_n(\omega) = 2^{-n}|\sigma_n(\omega)|^2$. The concatenation rule through which the Thue-Morse sequence is built, implies $\sigma_{n+1}(\omega) = \sigma_n(\omega)(1 - \mathrm{e}^{2^{n+1}\pi i\omega})$ and, respectively, $S_{n+1}(\omega) = S_n(\omega)(1-\cos 2^{n+1}\pi\omega)$. The evolution of $S_n(\omega)$ under the growing n allows to conclude both on the nature of the power spectrum at the given point ω and on the global distribution of the spectral measure μ:

$$\mu(\omega) = \lim_{n\to\infty} S_n(\omega) = \lim_{n\to\infty} \prod_{j=0}^{n-1} (1 - \cos 2^{j+1}\pi\omega) \tag{2.11}$$

The properties of $\mu(\omega)$ can be reconstructed from the asymptotic features of the infinite product (2.11) (also called the Riesz product [21]). It is straightforward to see that $S_n(\omega)$ vanishes at $\omega = 2^{-k}m$ for $n \ge k+1$ and arbitrary integer m, k [50]. For all the other rational values of ω, the ratio $\rho = S_{n+1}(\omega)/S_n(\omega)$ oscillates periodically with n. (These oscillations are preceded by a a transient whose length equals the multiplicity of the factor 2 in the factorization of the denominator of ω). When the geometric mean value $\langle\rho\rangle$ over the period of oscillations exceeds 1, the spectral sums S_n grow "on the average": $S_n \sim \langle\rho\rangle^n$ or, in terms of the length of the symbolic string, $S_n \sim l_n^\gamma$ where the growth rate γ equals $\log\langle\rho\rangle/\log 2$. However, no values of ω enable the delta peaks in the spectrum (or, in the diffraction jargon, the "Bragg peaks"): this would require $\gamma = 1$. This means that the discrete (atomic) component is absent in the spectrum. The fastest growth and, respectively, the largest γ is attained at $\omega = 2^{-k}m/3$ (of course, m should not be a multiple of 3); in this case $\gamma = \log 3/\log 2 - 1 = 0.584\ldots$[50]. Already this subset of ω-values is dense on the interval $[0, 1]$; this fact alone is sufficient to ensure that the capacity (box-counting dimension) D_0 of the set which carries the spectral measure, equals 1. However, since the latter measure is not absolutely continuous with respect to the Lebesgue measure, the other generalized dimensions D_q can differ from 1.

To describe the multifractal properties of $\mu(\omega)$, an appropriate partition of the interval $[0, 1]$ should be introduced. A standard way (see e.g. [50] where this formalism was applied to spectral measures) is to divide the unit interval into N small boxes of the length $\varepsilon = 1/N$, so that the probability to locate measure in the k-th subinterval is $p_k = \int_{(k-1)\varepsilon}^{k\varepsilon} \mu(\omega)d\omega$. The partition function is defined for any real number q as $Z(q, \varepsilon) = \sum_{k=1}^{N} p_k^q$. Assuming under the fixed q the scaling law $Z(q, \varepsilon) \sim \varepsilon^{\tau(q)}$, we arrive in the standard way [50] at the generalized (Rényi) dimensions: $D_q = \tau(q)/(q-1)$.

Since the normalization condition $\int_0^1 S_n(\omega)d\omega = 1$ holds for every n, we can use a sequence of $S_n(\omega)$ as approximations to the probability density. In its turn, this provides a sequence of approximations

$$\tilde{Z}(q, \varepsilon, n) = \sum_{k=1}^{1/\varepsilon} \left(\int_{(k-1)\varepsilon}^{k\varepsilon} S_n(\omega)d\omega \right)^q$$

to the partition function. As ε tends to zero, we can replace in these approxi-

mations summation by integration:

$$\tilde{Z}(q,\varepsilon,n) = \varepsilon^{q-1}\sum_{k=1}^{1/\varepsilon}\left(\frac{1}{\varepsilon}\int_{(k-1)\varepsilon}^{k\varepsilon} S_n(\omega)d\omega\right)^q \varepsilon \;\to\; \varepsilon^{q-1}\int_0^1 S_n^q(\omega)d\omega \qquad (2.12)$$

Apparently, infinite decrease of ε under fixed finite n makes no sense: in this way, one would approach the smooth $S_n(\omega)$ and obtain trivial scaling $\tau = q-1$. The decrease of ε should be combined with the simultaneous increase of n; this refinement of the partition allows to explore the asymptotical fine structure of $\mu(\omega)$. According to Eq.(2.11), the resolution in frequency domain for $S_{n+1}(\omega)$ is twice as good as that for $S_n(\omega)$. Respectively, seeking for the asymptotic scaling properties, one should compare $\tilde{Z}(q,\varepsilon,n)$ with $\tilde{Z}(q,\frac{\varepsilon}{2},n+1)$. Therefore $\tau(q)$ under fixed n and ε is evaluated as

$$-(\log 2)^{-1}\log\frac{\tilde{Z}(q,\frac{\varepsilon}{2},n+1)}{\tilde{Z}(q,\varepsilon,n)} \qquad (2.13)$$

which, taking into account the asymptotics (2.12), yields finally

$$D_q = \frac{\tau(q)}{q-1} = 1 - \frac{\log\lambda(q)}{(q-1)\log 2} \qquad (2.14)$$

where the growth rate $\lambda(q)$ is given by

$$\lambda(q) = \lim_{n\to\infty}\frac{\int_0^1 S_{n+1}^q(\omega)d\omega}{\int_0^1 S_n^q(\omega)d\omega} = \lim_{n\to\infty}\frac{\int_0^1\left(\prod_{k=0}^n(1-\cos(2^{k+1}\pi\omega)\right)^q d\omega}{\int_0^1\left(\prod_{k=0}^{n-1}(1-\cos(2^{k+1}\pi\omega)\right)^q d\omega} \qquad (2.15)$$

In this way, computation of the generalized dimensions D_q has been reduced to the evaluation of $\lambda(q)$.

2.4 Generalized dimensions D_q for integer values of q

In general, the only way to find the value of $\lambda(q)$ seems to be the direct numerical integration of numerator and denominator in Eq.(2.15) with subsequent extrapolation to the limit $n\to\infty$. However, the case of integer values of $q>1$ admits a simplification. The 2^n terms in the expansion of $S_n(\omega)$ into $\cos 2\pi k\omega$ range from $k=0$ to $k=2^n-1$. Respectively, for integer $q>0$ the cosine-expansion of $S_n^q(\omega)$ contains the terms until $\cos 2\pi(2^n-1)q\omega$: $S_n^q(\omega)=\sum_{k=1}^{q(2^n-1)} b_k^{(n)}\cos 2\pi k\omega$.

Let us pick out from the set of the coefficients $\{b_k^{(n)}\}$ the subset which corresponds to the multiples of 2^n: $a_j^{(n)}\equiv b_{j\times 2^n}^{(n)}$, $j=0,1,\ldots,q-1$. Obviously, of the whole expansion only the ω-independent term $a_0^{(n)}$ contributes to the integrals in (2.15), and $\lambda(q)$ equals $\lim_{n\to\infty} a_0^{(n+1)}/a_0^{(n)}$. When we proceed from S_n to S_{n+1}, the coefficients $a_j^{(n+1)}$ at $\cos 2\pi j 2^{n+1}\omega$ come into the consideration. By combinatorial arguments it can be easily shown that each of $a_j^{(n+1)}$ is a linear combination of $a_k^{(n)}$: thus, for $q=2$ we have

$$a_0^{(n+1)} \;=\; \frac{3}{2}a_0^{(n)} - a_1^{(n)}$$

$$a_1^{(n+1)} = \frac{1}{2}a_0^{(n)} - a_1^{(n)} \tag{2.16}$$

for $q = 3$ the recursion relations are

$$\begin{aligned} a_0^{(n+1)} &= \frac{5}{2}a_0^{(n)} - \frac{15}{8}a_1^{(n)} + \frac{3}{4}a_2^{(n)} \\ a_1^{(n+1)} &= \frac{3}{2}a_0^{(n)} - 2a_1^{(n)} + \frac{5}{2}a_2^{(n)} \\ a_2^{(n+1)} &= -\frac{1}{8}a_1^{(n)} + \frac{3}{4}a_2^{(n)} \end{aligned} \tag{2.17}$$

and so on. In case of S_q one has to do with the $q \times q$ matrix, whose elements are combinations of binomial coefficients with the coefficients of expansion of $\cos^n x$ into $\cos jx$. Although the general expressions are rather complicated, the computation of the matrix elements for not too large q is straightforward.

Since the relations (2.16),(2.17) etc. are linear, λ is simply the largest eigenvalue of the corresponding matrix and can be found from the respective characteristic equation. For $q = 2$ the equation is

$$\lambda^2 - \frac{\lambda}{2} - 1 = 0 \tag{2.18}$$

which yields $\lambda = (1 + \sqrt{17})/4 = 1.28077064\ldots$ and $D_2 = 1 - \log\lambda/\log 2 = 0.642981\ldots$.

For $q = 3$ we have

$$\lambda^3 - \frac{5}{4}\lambda^2 - \frac{3}{2}\lambda - 1 = 0 \tag{2.19}$$

and, respectively, $\lambda = 1.777389781\ldots$ and $D_3 = 0.58511995\ldots$; for $q = 4$ the characteristic equation is

$$\lambda^4 - \frac{13}{8}\lambda^3 - \frac{55}{16}\lambda^2 + \frac{17}{8}\lambda + 1 = 0 \tag{2.20}$$

with $\lambda = 2.579911342\ldots$ and $D_4 = 0.5442261703\ldots$, etc.

2.5 Generalized dimensions through the autocorrelation function

The same results can be expressed in terms of the autocorrelation functions. Being merely the Fourier transform of the power spectrum, $C(t)$ can be easily recovered from the spectral sums. In this sense, casting the Riesz product into the form of the trigonometric sum immediately yields the cosine-transform of the power spectrum and is especially convenient: let $c_j^{(n)} = 2\int_0^1 S_n(\omega)\cos(2\pi j\omega)d\omega$ denote the coefficient at $\cos 2\pi j\omega$ in S_n, then

$$C(j) = \frac{1}{2 - \delta_{0j}} \lim_{n\to\infty} c_j^{(n)} \tag{2.21}$$

(the factor $\frac{1}{2}$ at $j \neq 0$ enters the expression because S_n includes the contributions of both $C(j)$ and $C(-j)$).

This presentation allows to reformulate the above analysis of the growth of the coefficient $a_0^{(n)}$ in the expansions of $S_n^q(\omega)$. In the q-th power of the cosine-transform of $S_n(\omega)$, the ω-independent part is formed by the product terms with the vanishing net sum of trigonometrical arguments. Respectively, in the time domain the integral $\int_0^1 S_n^q(\omega)d\omega$ is represented by the sum of the products of q values of $C(j)$:

$$U(q,T) = \sum_{|j_1|+|j_2|+\ldots+|j_{q-1}|<T} C(j_1)C(j_2)\ldots C(j_{q-1})C(-j_1-j_2-\ldots-j_{q-1}) \tag{2.22}$$

where T is the length of the segment of the symbolic string, contributing to S_n. This sum grows with T according to the power law: $U(q,T) \sim T^{\kappa(q)}$ where $\kappa(q) = \log\lambda(q)/\log 2$. Respectively,

$$D_q = 1 - \frac{\kappa(q)}{q-1} \tag{2.23}$$

The expression (2.23) relates the Rényi dimensions of the spectral measure D_q for integer q with the growth law for the sums of $q-$products of the values of the autocorrelation function. For the case $q = 2$ it is equivalent to the formula derived in [23].

2.6 Cases of $q \to 0$ and large q

In case of small q the growth rate λ can be computed explicitly:

$$\begin{aligned}\lambda(q) &= \lim_{n\to\infty} \frac{1+q\int_0^1 \log S_{n+1}(\omega)d\omega}{1+q\int_0^1 \log S_n(\omega)d\omega} + O(q^2) \\ &= 1 + q\int_0^1 \log\frac{S_{n+1}(\omega)}{S_n(\omega)}d\omega + O(q^2) \\ &= 1 - q\log 2 + O(q^2)\end{aligned} \tag{2.24}$$

For the generalized dimension this yields:

$$D_q = 1 - \frac{\log\lambda}{(q-1)\log 2} = 1 - q + O(q^2) \tag{2.25}$$

In the opposite limit $q \to \infty$ the dominating contribution into $\int_0^1 S_n^q(\omega)d\omega$ is made by the values of ω which enable the fastest growth of the local finite-length approximations $S_n(\omega)$. The peaks in S_{n+1} which belong to the most rapidly growing family are 3/2 times higher than the peaks at the same places in S_n; at the same time, due to the improvement of the spectral resolution, the width of these peaks is halved. Therefore, $\lambda \cong \frac{1}{2}(3/2)^q$. Respectively,

$$D_q \cong \frac{q}{q-1}\left(2 - \frac{\log 3}{\log 2}\right) \tag{2.26}$$

As q grows, D_q tends to $D_\infty = 2 - \log 3/\log 2 = 0.415037\ldots$.

In fact, already moderate values of q are "large" enough: thus, the exact value of D_4 quoted above differs from the estimate (2.26) by less than 0.01; in case of $q = 6$ this difference is less than 0.0007, and for $q = 8$ it is even less than 0.00007.

2.7 Information dimension D_1

The case $q = 1$ should be treated separately. Differentiation of numerator and denominator in (2.14) provides the expression for the value of the information dimension:

$$D_1 = 1 - \frac{1}{\log 2} \lim_{n\to\infty} \int_0^1 \left(S_{n+1}(\omega) \log S_{n+1}(\omega) - S_n(\omega) \log S_n(\omega)\right) d\omega \quad (2.27)$$

Let us transform the integral in this expression:

$$\begin{aligned}
&\int_0^1 \left(\prod_{j=1}^{n+1} (1-\cos 2^j\pi\omega) \sum_{j=1}^{n+1} \log(1-\cos 2^j\pi\omega) \right. \\
&\qquad\qquad \left. - \prod_{j=1}^{n} (1-\cos 2^j\pi\omega) \sum_{j=1}^{n} \log(1-\cos 2^j\pi\omega) \right) d\omega = \\
&\int_0^1 S_n(\omega) \log(1-\cos 2\pi\omega) d\omega \qquad (2.28) \\
&\qquad\qquad - \int_0^1 \cos 2\pi\omega \sum_{j=2}^{n} \log(1-\cos 2^j\pi\omega) d\omega \\
&+ \int_0^1 \left(\prod_{j=2}^{n+1} (1-\cos 2^j\pi\omega) \sum_{j=2}^{n+1} \log(1-\cos 2^j\pi\omega) \right. \\
&\qquad\qquad \left. - \prod_{j=1}^{n} (1-\cos 2^j\pi\omega) \sum_{j=1}^{n} \log(1-\cos 2^j\pi\omega) \right) d\omega
\end{aligned}$$

Of the three integrals, the last one vanishes, since the contributions of its first and second parts mutually balance each other. Similarly, the second integral vanishes because $\sum_{j=2}^{n} \log(1-\cos 2^j\pi\omega)$ does not contain terms proportional to $\cos 2\pi\omega$: its cosine-expansion starts with $\cos 4\pi\omega$. Thus, the only remaining part is the first term

$$\int_0^1 S_n(\omega) \log(1-\cos 2\pi\omega) d\omega = -\log 2 - \sum_{j=1}^{2^n-1} \frac{c_j^{(n)}}{j} \quad (2.29)$$

where $c_j^{(n)}$, as above, is the coefficient at $\cos 2\pi j\omega$ in S_n. Taking into account Eq.(2.21) which relates $c_j^{(n)}$ to the values of the autocorrelation function $C(j)$, we get

$$D_1 = 1 - \frac{-\log 2 - \lim_{n\to\infty} \sum_{j=1}^{2^n-1} \frac{c_j^{(n)}}{j}}{\log 2} = 2 + \frac{2}{\log 2} \sum_{j=1}^{\infty} \frac{C(j)}{j} \quad (2.30)$$

Thus the problem is reduced to the estimation of the value $\Lambda \equiv \sum_{j=1}^{\infty} C(j)/j$.

The invariance of the infinite Thue-Morse sequence with respect to the inflation and the inverse operation of binary decimation imposes the recurrent

relations on the values of the autocorrelation function [40, 57]:

$$C(2j) = C(j), \quad C(2j+1) = -\frac{C(j)+C(j+1)}{2} \tag{2.31}$$

which, combined with the normalization condition $C(0) = 1$, allow to compute $C(j)$ for every value of j: $C(2^n) = -C(3\times 2^n) = -1/3$, $C(5\times 2^n) = C(7\times 2^n) = 0$, $C(9\times 2^n) = -C(11\times 2^n) = 1/6$, and so on ($n = 0, 1, \ldots$). This information alone does not allow to obtain Λ in a closed form. The series in (2.30) converges slowly ($\sim j^{-1}$); however, the recursions (2.31) allow to implement the "internal summation" which leads to the noticeable (in principle, indefinite) acceleration of the convergence. Let Ξ be a sum

$$\Xi = a + \sum_{j=1}^{\infty} f(j)C(j) \tag{2.32}$$

where a is a constant and $f(j)$ is some function of j. Transforming this expression with the help of (2.31), we obtain

$$\Xi = a - \frac{f(1)}{2} + \sum_{j=1}^{\infty} \frac{2f(2j) - f(2j-1) - f(2j+1)}{2} C(j) \tag{2.33}$$

This provides the iteration scheme:

$$a_{m+1} = a_m - \frac{f_m(1)}{2} \tag{2.34}$$

$$f_{m+1}(j) = \frac{2f_m(2j) - f_m(2j-1) - f_m(2j+1)}{2} \tag{2.35}$$

where, in order to compute Λ, we should start with $a_0 = 0$ and $f_0 = 1/j$.

Since the expression on the right of Eq.(2.35) is the (rescaled and shifted) finite-difference approximation for the second derivative of $f_m(j)$, the result of k iterations of Eq.(2.34,2.35) provides a series in $C(j)$ whose coefficients $f_k(j)$ converge as j^{-1-2k}. Successive transformations yield

$$\Lambda = -\frac{1}{2} - \sum_{j=1}^{\infty} \frac{C(j)}{2j(4j^2-1)} = -\frac{5}{12} + \sum_{j=1}^{\infty} \frac{(96j^2-9)C(j)}{4j(4j^2-1)(16j^2-1)(16j^2-9)} = \ldots \tag{2.36}$$

Although the further expressions are too cumbersome to quote them explicitly, their derivation is straightforward and can be easily performed with every program for symbolic computations. Already after the 7-th iteration the coefficients at $C(2)$, $C(3)$ and $C(4)$ have an order of, respectively, $10^{-15}, 10^{-18}$ and 10^{-20}, and it is enough to take the first two terms in the series (that is, $a^{(7)}$ and the term at $C(1)$), in order to produce Λ with 14 correct digits: $\Lambda = -0.43995518283629$ and, respectively, $D_1 = 0.73055767901739\ldots$

2.8 Discussion

The approach which we have proposed above, is not restricted to the particularities of the Thue-Morse sequence. In the general case, as soon as the building

rules of the symbolic sequence allow to explicitly interrelate the consecutive approximations $S_n(\omega)$ and $S_{n+1}(\omega)$ to the spectral measure $\mu(\omega)$, the same technique can help to extract the generalized dimensions from the corresponding characteristic equations.

Similarly, the expression (2.23) which relates the generalized dimensions to the growth rate of the products of the autocorrelation function values, remains valid for a broad class of problems and can be applied not only to binary symbolic sequences but to general (stationary) datasets of computational or experimental origin. In case of processes with singular continuous or mixed Fourier spectra the direct evaluation of spectral sums (and thereby of the set which supports the spectral measure) is sensitive to the numerical details like frequency resolution, etc. Compared to this, the estimation of the autocorrelation function is a robust procedure. Thus the relationship (2.23) allows one in principle to recover the generalized dimensions from observational and numerical data. However, the rapid growth of the number of terms in the sums $U(q,T)$ (this number is proportional to T^{q-1}) makes its application for $q > 4$ hardly practical.

Chapter 3

Symbolic dynamics behind the singular continuous power spectra of continuous flows

3.1 Introduction

The common way to obtain the discretized description of a continuous process is to mimic the flow by some recurrent relation binding the current position of the imaging point to its location at certain future and/or past moments. This construction replaces the continuous independent variable by an integer. A remarkably efficient tool for this is the Poincaré map which interrelates two consecutive returns onto some appropriate part of a suitably chosen codimension-1 surface (Poincaré surface) in the phase space; it is required that the relevant orbits intersect this surface transversely. In many situations the dynamics of the flow is adequately reproduced by the dynamics of the Poincaré map. Accordingly, there is a widespread feeling that the reduction to the map is an innocent procedure which preserves the dynamical features completely. However, this is not necessarily the case, and our current study is focused on one origin of the possible discrepancies.

In general, the time interval $\tau_{\rm r}$ between the consecutive intersections with the Poincaré surface is not constant. Usually $\tau_{\rm r}$ as a function of the coordinates on this surface is bounded and continuous (as in the case of a Feigenbaum attractor), and there is no qualitative difference between the properties of the map and the flow. Moreover, in some situations it is possible to make the moments of intersections equidistant by shifting the secant surface and reparameterizing the time [22]; thus the flow becomes a suspension over the Poincaré mapping and their features coincide. An example is given by quasiperiodic motions, provided that the rotation numbers are not anomalously close to their rational approximants. On the other hand, it is known that discontinuities and singularities in $\tau_{\rm r}$ may lead to a qualitative change of dynamical properties, like the birth of a continuous spectrum [36] or the onset of mixing [37, 38]. In this Chapter, we

will address a situation where a saddle-point of the flow belongs to the closure of the attractor. Here $\tau_{\rm r}$ is finite for those points at the Poincaré surface which do not lie on the intersection of this surface with the local stable manifold of the saddle. On the contrary, orbits which start from points close to this intersection slow down in the vicinity of the saddle; this results in a marked increase of $\tau_{\rm r}$. As a function of a coordinate (say, x) parameterizing some path along the Poincaré surface, the return time diverges at the intersection point x_0; this singularity is logarithmic ($\tau_{\rm r} \sim -\log|x-x_0|$) for non-degenerate saddles and power-like ($\tau_{\rm r} \sim |x-x_0|^{-\beta}, \beta > 0$) otherwise. Under these circumstances the averaged characteristics (like the Fourier spectra) computed from the map by a procedure which treats all the points uniformly and does not assign additional weights to the "neighborhood of singularity", can differ dramatically from those of the prototype flow. For instance, in the situation when the power spectrum of the flow is (singular) continuous, the return map may nevertheless have a discrete spectrum which is a signature of a qualitatively different type of dynamics. This situation was encountered in [49]; the objective of the current paper is to analyze the influence of the distribution of return times on the power spectrum.

Unbounded return times are inherent in continuous systems close to homoclinic and heteroclinic bifurcations. After a brief introduction to singular continuous spectra in section 3.2, we proceed in section 3.3 to the description of a particular dissipative flow whose attractor possesses the demanded properties, and develop in section 3.4 a kind of an "improved" semi-discrete model which effectively accounts for the variations in return times. In section 3.5 we reduce this model to self-similar symbolic sequences; the subsequent calculation of their spectral and correlation characteristics in section 3.6 reproduces the respective features of the flow and demonstrates qualitative differences in comparison with the usual Poincaré mapping.

3.2 Singular continuous spectra in dynamics

Systems with singular continuous spectra constitute a kind of a bridge between regular behavior and chaotic dynamics. Unlike ordered systems, they do not preserve the complete information about the details of an initial state; nevertheless, unlike the chaotic systems, they still exhibit a kind of a vague memory about the distant past. The basic feature of this kind of dynamics is reflected in the name: the spectral measure is neither pure point (discrete) nor absolutely continuous with respect to the Lebesgue measure, but is singular continuous; its carrier is a dense Cantor set. The calculation of the power spectra for the observable ζ from the respective time series $\{\zeta_k\}$ through the familiar expression

$$S(\omega, l) = \frac{1}{l}\langle | \sum_{k=m}^{m-1+l} \zeta_k \mathrm{e}^{i2\pi k\omega} |^2 \rangle \tag{3.1}$$

(the angular brackets denote averaging over the initial position m) fails to provide conventional results. With the increase of the sample length l, the partial sums $S(\omega, l)$ converge for a dense set of frequency values ω neither to constant values (which would correspond to an absolutely continuous spectrum), nor grow linearly with l (which would hold for the discrete spectra). Usually they grow as $S(\omega, l) \sim l^{\gamma(\omega)}$ ($0< \gamma(\omega) <1$), and one observes a "fractalization" of the spectral

curve. Accordingly, estimation of the autocorrelation function for such processes shows that the correlations neither ultimately decay for large τ, which would be the case for chaotic motion, nor display the infinite sequences of exact (or arbitrarily close) returns to unity, as for periodic (respectively, quasiperiodic) processes.

The autocorrelation function gives a reasonably reliable numerical tool for telling processes with singular continuous spectra from such with discrete or absolutely continuous ones. Recall that the necessary condition for the spectral measure to be absolutely continuous is the decay of correlations. On the other hand, the pure point component is absent if the value of the integrated correlation $C_{\rm int}(T)= \frac{1}{T}\int_0^T |C(\tau)|^2 d\tau$ vanishes for $T \to \infty$[53]. Thus the numerical observation that the function $C(\tau)$ displays repetitive peaks of non-diminishing height over the longest computationally available values of τ whereas $C_{\rm int}$ decays (usually in a power-like way), provides reasons to conjecture that one has to do with a singular continuous spectrum. Keeping this criterion in mind, we will use the spectral vocabulary but make our judgments from the appearance of the respective autocorrelation functions.

3.3 The flow and its maps: affinity and mismatch

For our purpose we need a flow in which orbits on the attractor pass arbitrary close to the saddle point. This is the case for the Lorenz attractor [58] which contains the saddle point in its closure; however here already the Poincaré map delivers the fully chaotic dynamics [27] with positive Lyapunov exponent and continuous Fourier spectrum. A more appropriate example is provided by continuous dynamical systems at the accumulation point of the "homoclinic doublings" scenario. For such flows it has been recently demonstrated that their spectral properties can be qualitatively different from those of the induced return maps [49]. We will exploit this example to see in detail how the slowing down near the saddle results in the singularities of the power spectra.

As a starting point we take the symmetric case of Eq.(1.6): the system of the third order

$$\begin{aligned} \dot{x} &= \sigma(y-x) + \sigma D y(z-r) \\ \dot{y} &= rx - y - xz \\ \dot{z} &= xy - bz \end{aligned} \tag{3.2}$$

which differs from the conventional Lorenz equations in their standard notation by the additional term proportional to the non-negative parameter D. The detailed description of the underlying hydro-mechanical problem, of the equations themselves and of the numerous bifurcation scenarios can be found elsewhere [13, 17, 49]; here we will only briefly recall the properties which are relevant for our current purpose. In the parameter region $D > (r-1)/r^2$ the trivial equilibrium $x = y = z = 0$ is a saddle with one-dimensional unstable manifold. Inside this region the increase of r eventually leads to the formation and subsequent destruction of homoclinic connections to the equilibrium; due to the symmetry $\{x, y\} \leftrightarrow \{-x, -y\}$ (inherited from the Lorenz equations), the homoclinic orbits always arrive in pairs. In the parameter domain $r-1-(\sigma+1-b)/\sigma < r^2 D < r-1$

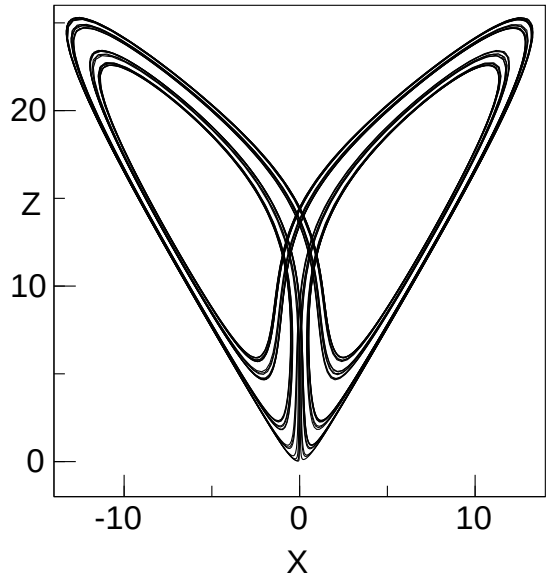

Figure 3.1: Attractor for eq. (3.2) at the accumulation point of homoclinic bifurcations
(σ=10; b=8/3; $r = 15.82373667\ldots$; $D = 0.052634923\ldots$);
The saddle point is located at the origin; the saddle index ν equals 2.0.

the positive eigenvalue λ_1 which locally characterizes the unstable direction, is smaller than the absolute value $|\lambda_2| = b$ of the leading (closest to zero) negative eigenvalue. This implies that unlike the Lorenz case, the destruction of the couple of homoclinic orbits does not create a chaotic set, but instead "glues" two stable mutually symmetrical closed orbits into a single one. In this way the length of the attracting trajectory in the phase space is doubled; notably, the period at the bifurcation point is infinite. Further increase of r leads through a bifurcation sequence in which symmetry-breakings of periodic orbits alternate with new homoclinic doublings (in systems with the Lorenz-like mirror symmetry each of these bifurcations is a codimension-1 event). The renormalization treatment of the reduced return mapping shows that this sequence converges in a universal i way [14, 13]; the quantitative characteristics of the scenario (convergence rate, scaling properties of the resulting attracting set, etc.) depend only on the saddle index $\nu = |\lambda_2|/\lambda_1$ which uniquely determines the universality class.

The projection of this latter set is presented in Fig. 3.1; one notices both the reflection symmetry and the self-similar structure of the attractor. The unstable manifold Γ_u of (0,0,0) belongs to the attractor and provides a convenient way to characterize its scaling: starting from the outermost turn, the distance between the 2^n-th and 2^{n+1}-th turns of Γ_u decays as α^{-n}. The scaling factor α as a function of the saddle index ν monotonically decreases from $\alpha = \infty$ for $\nu = 1$ to $\alpha \to 1$ for $\nu = \infty$ (the latter case corresponds to vanishing of the eigenvalue λ_1 at the stability boundary of the equilibrium).

The geometry of the attractor admits the convenient symbolic coding. Let us assign the symbol R to each revolution of the orbit in the half-space $x > 0$

and the symbol L to the revolution in the half-space $x < 0$. At each homoclinic doubling the two mutually symmetric attracting orbits (whose codes turn into each other under the transformation $R \leftrightarrow L$) are glued together; thereby the code of the new attractor is simply the concatenation of the codes of its parents. This scenario runs through the steps $R \to RL \to RLLR \to RLLRLRRL\ldots$ and ends up with the symbolic object familiar from the previous Chapter: the Thue-Morse code [18, 19].

One would expect that the symbolic dynamics (as given by the Thue-Morse sequence) directly reflects the properties of the continuous system (3.2). Indeed, the estimates of power spectra computed from the finite series of the variables $x(t)$, $y(t)$ and $z(t)$ of the flow display no tendency to converge to smooth curves with the increase of the sample length [49]. Calculation of the autocorrelation function (Fig. 3.2a,b) demonstrates a series of moderate (distinctly lower than the unit value) peaks which, although becoming more and more seldom, preserve the same height (the rightmost peaks at these plots correspond to $\approx 2^{15}$ revolutions around the attractor). The integrated correlation function $C_{\rm int}$ decays within the same time interval by a factor of $\approx 10^3$ (Fig. 3.3). Thus, we have convincing numerical evidence that the criterion from preceding section is fulfilled: $C_{\rm int}$ decays whereas $C(\tau)$does not; accordingly, we may conjecture that the spectrum is singular continuous. (In fact, the analysis below implies that the discrete spectral component might be present as well, but its contribution seems to be exclusively small).

The autocorrelation function in logarithmic timescale for the variable $x(t)$ is plotted in Fig.3.2a; the whole structure is reminiscent of the correlation function for the Thue-Morse sequence (Fig. 3.2c). The latter can be computed with the help of the recurrent formulae $C(2\tau) = C(\tau)$, $C(2\tau+1) = -\frac{C(\tau)+C(\tau+1)}{2}$; its largest peak values are $C(3\times 2^n)$=–$C(2^n)$=1/3, $n = 0, 1, 2, 3\ldots$. [1] (A closer look at the two plots shows that this typical symmetry between the positive and negative peaks of $C(\tau)$ is absent for the continuous variable; accordingly, a finer symbolic description of the flow should yield the symbolic sequence with asymmetric autocorrelation function).

In studying the properties of the continuous system (3.2) the natural way is to reduce the dynamics to the return map; in presence of a stable foliation the map can be further reduced to a one-dimensional one. Should the surface of section be chosen transversely to the stable manifold of the saddle (in practice, fixing a small value of z is sufficient), this map will have a form

$$\xi_{i+1} = f_\xi(\xi_i) = (|\xi_i|^\nu - \mu)\ \mathrm{sign}(\xi_i) \tag{3.3}$$

up to the higher order terms in $\xi_i|\xi_i|^{\nu-1}$. Here the coordinate ξ is measured along the unstable manifold of the saddle; ν is the saddle index (unlike the Lorenz case, $\nu > 1$). The parameter μ characterizes the distance between the first return of the unstable manifold and the local stable manifold: $\mu = 0$ corresponds to the formation of a couple of simple (1-looped) homoclinic orbits. The two antisymmetric branches of the discontinuous map (3.3) correspond to the two components of the unstable manifold of the saddle-point of initial

[1] For the flows $C(\tau)$ is well defined for all τ; for a comparison with symbolic sequences and maps, one should choose in the continuous system times $t = n\tau_{av}$ $(n = 1, 2, 3, \ldots)$ where τ_{av} is the average duration of one loop (which for the attractor of Fig. 3.1 is 1.85465... in the dimensionless time units of (3.2)).

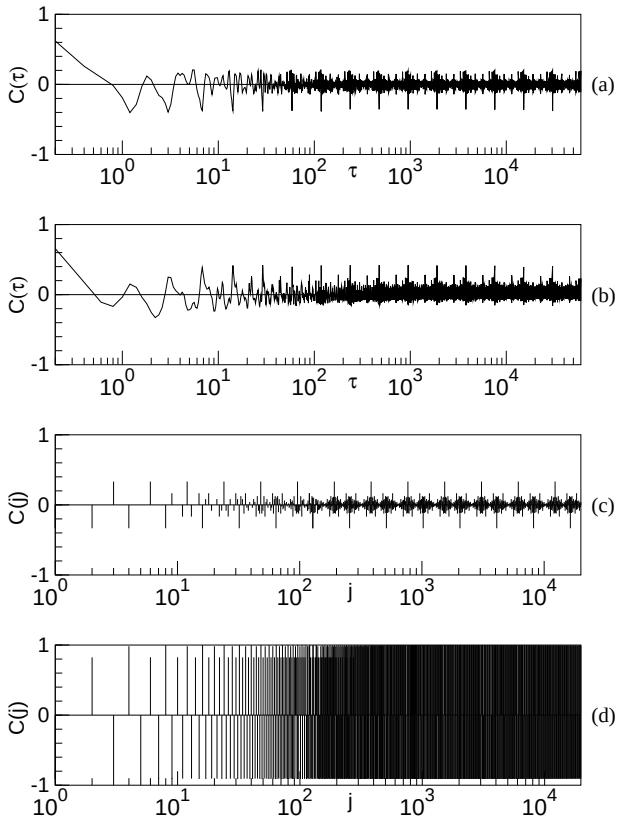

Figure 3.2: Autocorrelation function in logarithmic timescale for the observables:
a) variable $x(t)$ for the attractor from Fig. 3.1;
b) variable $z(t)$ for the attractor from Fig. 3.1;
c) Thue-Morse sequence;
d) attracting orbit of f_z at m^*.

system. On assigning the symbol R (L) to iterations with positive (negative) ξ, one obtains a convenient coding; obviously, for the parameter value $\mu^*(\nu)$ which marks the accumulation of the homoclinic doublings, the symbolic code of the attractor is the Thue-Morse sequence. No wonder that the spectrum of the orbit of the map (3.3) at this parameter value also proves to be singular continuous.

The described way to construct the return map is by far not the only one; the Poincaré surface may be for instance any of cylinders whose axis passes through the saddle point and is perpendicular to the z-axis. Once again, the stable foliation reduces the dynamics to a one-dimensional map. If the map variable is chosen to be x or y or any combination thereof, then the map itself has the form of eq.(3.3). However if one chooses the z-coordinate of the intersections, then (after proper rescaling, shift and truncation up to the terms of the order $O(|z_i|^\nu)$) the map takes the form

$$z_{i+1} = f_z(z_i) = \mu - |z_i|^\nu \tag{3.4}$$

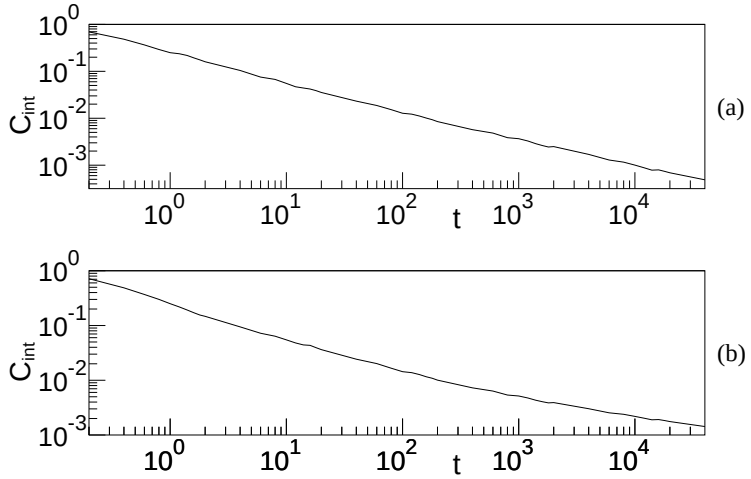

Figure 3.3: Integrated autocorrelation in logarithmic timescale;
the observables are:
a) variable $x(t)$; b) variable $z(t)$ from eq.(3.2)
for parameter values from Fig. 3.1.

(a similar expression is obtained for the return map of subsequent z-maxima as it was done in the initial paper of Lorenz [58]). Unlike eq.(3.3), the map (3.4) is continuous and unimodal; on changing the parameter μ, instead of the sequence of homoclinic bifurcations the period-doubling scenario is encountered. Obviously, f_z is nothing else but the even counterpart of the odd f_ξ: one has $f_\xi(x) = f_z(x)\mathrm{sign}(x)$, and, therefore, $|f_\xi^n(x)| = |f_z^n(x)|$ for each n. Consequently, there exists a one-to-one correspondence between the bifurcational parameter values in these two maps [14]: the symmetry-breakings of eq.(3.3) correspond to period-doublings in eq.(3.4), whereas the homoclinic bifurcations in eq.(3.3) are matched by the points of superstability for the periodic orbits of the map (3.4). The convergence rate $\delta(\nu)$ of both scenarios depends on the saddle index ν; it increases monotonically from $\delta(1)$=2 to $\delta(\infty) = 29.57\ldots$ [59]; obviously, for the case of quadratic singularity $\nu = 2$ it is given by the Feigenbaum constant: $\delta(2)$=4.669201.... The symbolic codings in the limiting points of both scenarios are the well-known symbolic itinerary of the period-doubling attractor [60] $\{P_j\} = RLRRRLRL\ldots$ and the Thue-Morse sequence $\{T_j\} = RLLRLRRL\ldots$. These codes are interrelated: if one starts with $T_1 = R$ and assigns the values of -1 and 1 to L and R respectively, the sequence $\{T_j\}$ can be obtained from $\{P_j\}$ by recursion:

$$T_{j+1} = \prod_{k=1}^{j}(-P_k) = -P_j T_j \tag{3.5}$$

However the dynamics on the period-doubling attractor which exists at $\mu = \mu^*(\nu)$, is not equivalent to its counterpart from eq.(3.3): the values of the autocorrelation function $C(n)$ for the attractor of eq.(3.4) approach 1 for even n (Fig. 3.2d); respectively, the power spectrum of z_j as well as the spectrum of the symbolic itinerary $\{P_j\}$ are both pure point.

Thus two one-dimensional reductions of the same two-dimensional Poincaré map prove to have attractors with qualitatively different dynamics. This seeming paradox is easily resolved when one recalls that the variables x and z have different symmetries with respect to the original flow. According to eq.(3.5) the rule which yields the value of the n-th element of the Thue-Morse sequence as a function of n, is simply a skew product over the analogous rule for the period-doubling itinerary; it is known that a skew product over a dynamical system often possesses the richer spectral properties than the system itself [20]. Another discrepancy arises in relationship between the continuous variable $z(t)$ from (3.2) and its discretized version z_i from (3.4), as seen from the autocorrelation functions for the former (Fig. 3.2b) and for the latter (Fig. 3.2d). One notices series of persistent peaks in Fig. 3.2b; although these are definitely lower than 1, the correlations do not ultimately decay. Combined with the apparent decay of the integrated function $C_{\rm int}(t)$ (Fig. 3.3b), this points to the singular continuous spectral component. This confirms that a "straightforward" discretization with the help of the return map fails to capture the basic feature of the dynamics, presenting it more ordered than it really is. As found in [49], the reason for this failure lies in the divergence of the return times near the saddle point, which remains unnoticed by the return map. Below we introduce the simplified model which incorporates the return times into this map, thus allowing us to see explicitly how the non-uniformity of the return times influences the power spectrum of the process.

3.4 Modeling non-equal return times

Our starting point is the continuous dependence $z(t)$ from eq.(3.2) (as plotted in Fig. 3.4a); our aim is to obtain a map which adequately models the spectral properties of $z(t)$. The crosses mark the intersections of the orbit with the cylinder $x^2+y^2=9$ (with $\frac{d}{dt}(x^2+y^2)>0$); the resulting sequence $\{z_i\}$ induces a mapping f_z. As seen from Fig. 3.4a, the peaks are sharp and the valleys are broad (the lower the minimum, the broader the plateau around it). The system spends a noticeable time in the region of relatively small z, that is, near the saddle point where the "velocity" of the imaging point is much lower than elsewhere. It is therefore natural that characteristics (correlation functions, spectra etc.) averaged over time are strongly influenced by the contributions of the low-amplitude part of the orbit. One can hope to extract the necessary information from the points $\{z_i\}$. However, as we know, taking the mapping f_z as it is would be insufficient, since it does not take into account the differences between the durations of residence at different z_i's.

Let us couple the return map on the Poincaré surface to the temporal distribution of returns. Consider the discontinuous process $u(t)$ where $u(t)$ admits the constant value z_j (or ξ_j, if one models the variable $x(t)$) for the whole interval of time between the j-th and $j+1$-th intersections; it jumps to z_{j+1} (respectively, ξ_{j+1}) in the right endpoint of this interval (Fig. 3.4b). This construction in which the time is continuous and the observable variable is piecewise constant, is known under the name of "special flow" [20], and can be viewed as the map whose iterations are separated by non-equal time differences . Thus, the return times turn into the "residence durations".

Near the non-degenerate saddle point the return time has a logarithmic

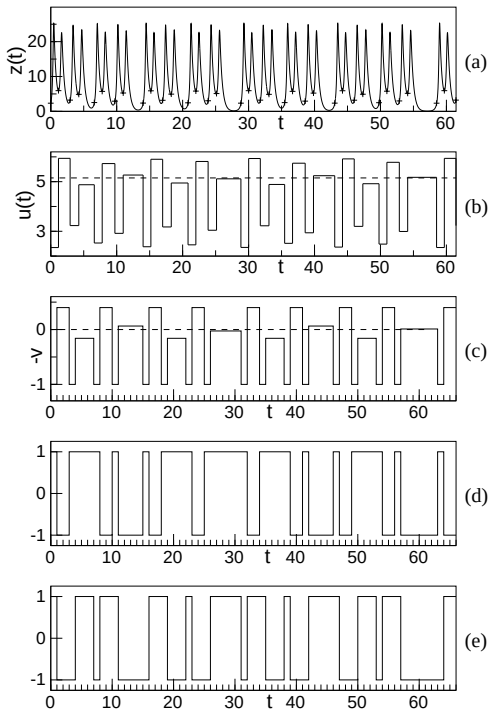

Figure 3.4: Time dependencies corresponding to 34 orbit turns
(residence durations in c), d) and e) are given by (3.8)):
a) variable $z(t)$ (crosses denote intersections with Poincaré surface);
b) special flow $u(t)$ over the mapping induced by crosses in subplot a);
dashed line denotes the preimage of the extremum of z_j;
c) special flow over the variable v_n with $\alpha = 2.5$ and $\tau_0 = 0$
(as compared to $u(t)$, v is shifted and rescaled, and its sign is changed);
d) process reconstructed from the period-doubling code;
e) process reconstructed from the Thue-Morse sequence.

singularity; we model it by the function

$$\tau_{\rm r}(u) = A + B \log \frac{1}{|u|} \tag{3.6}$$

where the variable u stands both for ξ_i from (3.3) and z_i from (3.4). Here, the logarithmic term is responsible for the hovering near the saddle, and the u-independent term A gives roughly the time spent on the global (distant from the saddle) segment of the orbit loop. By itself, the knowledge of the coordinate dependence $\tau_{\rm r}(u)$ does not yet provide the statistics of return times: this would also require the complete knowledge of the distribution of the values of u on the attractor. We approximate this distribution taking use of the scaling properties.

Both for the scenario of homoclinic doublings in (3.3) and for the period-doubling sequence in (3.4) the Feigenbaum-Cvitanović renormalization equation $g(u) = \alpha g(g(u/\alpha))$ [61] yields the universal function $g(u)$ which is discontinuous (piecewise increasing) in the former case and has extrema of order ν in the latter. Since eq.(3.6) is logarithmic, presentation on logarithmic scale is especially

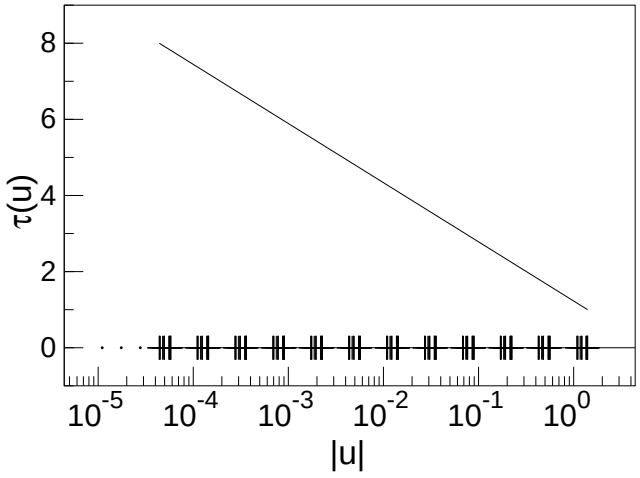

Figure 3.5: Logarithmic coordinate dependence of residence durations $\tau(u)$ in the points of the attractor (points of the period-doubling attractor are marked along the abscissa).

illuminating (Fig. 3.5): one sees that the points on the attractor are grouped around the values $d_n{=}g^{2^n}(0){=}\alpha^{-n}g(0)$, with the size of the n-th "cluster" being of order $d_n/|\alpha|$. Take the sequence $\{u_i\}$ obtained from $u_0 = 0_+$ by iterating the function f_ξ or f_z. The n-th iteration of the extremum lies in the $j+1$-th cluster where $j(n)$ is the number of the first non-zero coefficient m_j in the binary expansion of n: $n = \sum_{j=0}^{\infty} m_j 2^j$ (thus, all odd iterations belong to the 1-st cluster located at a distance of μ^* from the origin). In our further estimates we neglect the distances between the points within the same cluster. In other words, instead of the sequence $\{u_n\}$ we consider the values $v_n \equiv \mu^*|\alpha|^{-j(n)}\mathrm{sign}(u_n)$. For v_n the value of $\tau_{\mathrm{r}}(v_n)$ equals

$$\tau_{\mathrm{r}}(v_n) = \tau_{\mathrm{r}}(\mu^*|\alpha|^{-j(n)} = A - B\log\mu^* + B\,j(n)\log|\alpha|) \tag{3.7}$$

Apparently, this approximation should work better for larger values of $|\alpha|$, that is, in the range of not too large values of the saddle index ν.

Let the time be measured in units of $B\log|\alpha|$; in these units eq.(3.7) can be rewritten as

$$\tau_{\mathrm{r}}(v_n) = \frac{A - B\log(\mu^*|\alpha|)}{B\log|\alpha|} + 1 + j(n) \equiv \tau_0 + (1 + j(n)) \tag{3.8}$$

In this notation, τ_0 is the contribution of the global segment, and the bracketed term presents the logarithmic divergence of residence times on the attractor with geometric scaling: for all the odd values of n it equals 1, for the even values which are not multiples of 4, it equals 2, etc.

The mean residence duration under the law (3.8) is $\tau_0{+}2$; it corresponds in the original continuous system to the average duration of one turn of the trajectory on the attractor. Evolution of the "continuous" variable reconstructed in this way from the discrete sequence $\{v_n\}$ for the unimodal map (3.4) with $\nu{=}2$ is plotted in Fig. 3.4c. The autocorrelation function for this process (Fig. 3.6a) is qualitatively very similar to $C(\tau)$ computed for the original continuous variable $z(t)$ and plotted in Fig. 3.2b.

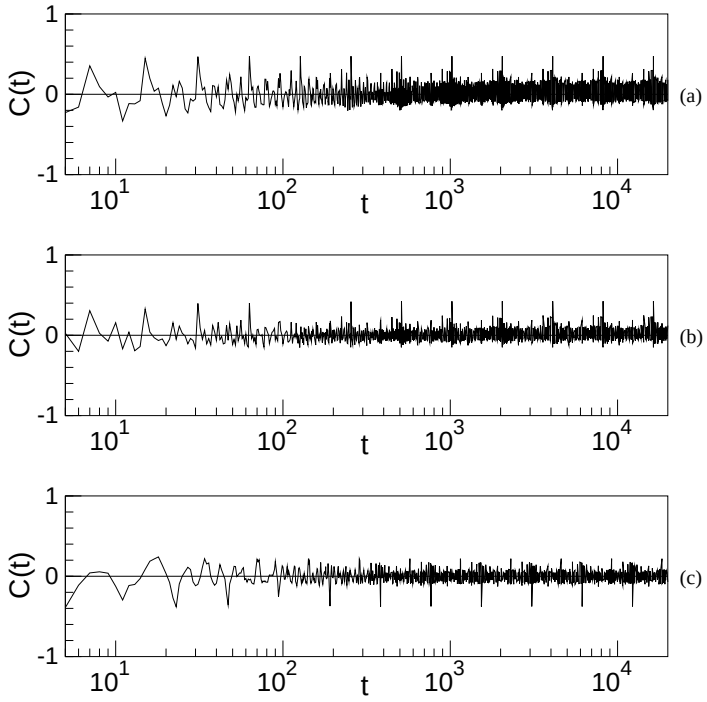

Figure 3.6: Autocorrelation function in logarithmic timescale for the observables:
a) variable $v(t)$ from Fig. 3.4c;
b) process reconstructed from period-doubling code (as in Fig. 3.4d);
c) process reconstructed from the Thue-Morse code (as in Fig. 3.4e).

3.5 Transformation of symbolic sequences

Insofar, we approximated the range of $z(t)$ by the set $\{\mu^*|\alpha|^{-j(n)}\}$ without any qualitative changes in the autocorrelations. A further simplification eliminates the coordinate values at all; we replace $u(t)$ in the special flow by $\mathrm{sign}(u)$. The process obtained in this way from the special flow over the period-doubling attractor is presented in Fig. 3.4d; the analogous procedure applied to the special flow over the discontinuous map (3.3) yields the process shown in Fig. 3.4e. The respective autocorrelation functions are plotted in Fig. 3.6b,c; their likeness to the autocorrelation functions of the original continuous variables $z(t)$ and $x(t)$ is apparent. Noteworthy, the plot in Fig. 3.6c has lost the typical up-down symmetry of the autocorrelation function for Thue-Morse sequence.

The rough description with the help of $\mathrm{sign}(u)$ is in fact nothing else but coding with two symbols. Therefore, another way to view the results of this last simplification could be the following: Given the symbolic sequence, we prescribe the "residence duration" of the n-th symbol by $\tau_{\mathrm{r}}(n) = \tau_0 + (1 + j(n))$, and build in this way a kind of a special flow over the symbolic sequence. From this point of view, the plots in Fig. 3.4d and Fig. 3.4e present continuous-time processes reconstructed from the period-doubling code and the Thue-Morse sequence, respectively.

Now let us assume that τ_0 is a non-negative integer and go back from contin-

uous time to symbolic sequences. For example, starting from the Thue-Morse sequence $\{T_j\} = R\,L\,L\,R\,L\,R\ldots$, taking $\tau_0 = 0$ and keeping in mind that $j(1) = j(3) = j(5) = 0$, $j(2) = j(6) = 1$ etc., we arrive at the sequence in which the second and the sixth symbol of $\{T_j\}$ are repeated twice, the fourth one is repeated three times, and so on: $R\,LL\;\;L\,RRR\,L\,RR\;\ldots$.

From now on the object of our studies will be symbolic codes obtained by introducing the residence durations into $\{P_j\}$ and $\{T_j\}$. In fact, instead of the direct evaluation of these durations for each particular symbol, we will utilize the self-similarity of the codes. There are two equivalent methods to construct a self-similar symbolic sequence from an initial segment. One of them is to substitute recursively each letter of this segment by a prescribed sequence of symbols; in this way the sequence is "inflated" from inside. The other method is the concatenation: one deals with several sorts of symbolic "bricks" which are consecutively added to one another in the prescribed order; the result is treated as a new set of bricks, the procedure being repeated *ad infinitum*. During this process the "head" of the sequence (which is just the initial segment) remains unchanged whereas the "tail" grows and gets longer and longer.

Let us discuss briefly the first of these methods. At each step of the substitution (inflation) each symbol is substituted according to a specific rule. For both initial sequences these rules involve two letters: the period-doubling code $\{P_j\}$ can be obtained from the initial symbol R by repeated substitutions $R \to RL$, $L \to RR$, and the Thue-Morse sequence evolves from the same R under the action of the symmetric substitution $R \to RL$, $L \to LR$. The inflation rules which take into account the distribution of residence durations, require in both cases four letters. For the code $\{\Pi_j\}$ obtained from $\{P_j\}$, the rule is

$$A \to ABC,\;\; B \to AAD,\;\; C \to D,\;\; D \to C \tag{3.9}$$

One should start with the symbol A; before assigning the numerical values to the letters, each A must be replaced by a chain of $\tau_0 + 1$ symbols R, each B should be identified with $\tau_0 + 1$ subsequent L's, each C becomes a single L and each D becomes a single R, respectively. The code $\{\Upsilon_j\}$ built over the Thue-Morse sequence is generated from $\Upsilon_1 = A$ by the inflation rule

$$A \to ABC,\;\; B \to BAD,\;\; C \to D,\;\; D \to C \tag{3.10}$$

with the same condition for replacements before identifying the symbols with numbers. In each case, after m steps the sequence consists of $2^m - 1$ symbols. It is convenient to characterize the substitution with the help of its associated matrix [62, 7]. Let our alphabet consist of k symbols $a_1, a_2, \ldots, a_k$. Take an arbitrary word in which all the letters are represented (this requirement excludes a risk of picking a word from the subset of alphabet which is substituted only through its own elements), and inflate it. The relation between the numbers of entries of each type $n_{a_1}, \ldots\, n_{a_k}$ in the initial word and the respective numbers $n'_{a_1}, \ldots\, n'_{a_k}$ for the transformed word, is

$$\begin{pmatrix} n'_{a_1} \\ \ldots \\ n'_{a_k} \end{pmatrix} = M \begin{pmatrix} n_{a_1} \\ \ldots \\ n_{a_k} \end{pmatrix} \tag{3.11}$$

and M is called the associated matrix of the substitution rule. In case of the period-doubling code this matrix is $\left(\begin{smallmatrix} 1 & 2 \\ 1 & 0 \end{smallmatrix}\right)$, and for the Thue-Morse sequence it is

$\left(\begin{smallmatrix}1&1\\1&1\end{smallmatrix}\right)$. Noteworthy, the ordering of symbols in the substitution finds no reflection in M; only the overall numbers of entries of each type count. According to the conjecture of Bombieri and Taylor[62], spectral properties of the symbolic code are determined by the location of eigenvalues of the associated matrix for its substitution rule: a discrete component must be present, if the so-called Pisot-Vijayaraghavan (PV) condition is satisfied. This condition requires that strictly one eigenvalue is larger than one whereas the rest of the eigenvalues lies within the unit circle. Already the Thue-Morse code provides an important exception to this rule: although the PV condition is fulfilled (the eigenvalues are 2 and 0), the spectrum, instead of being discrete, is singular continuous.

The associated matrix for the substitution (3.9) is

$$\begin{pmatrix} 1 & 2 & 0 & 0 \\ 1 & 0 & 0 & 0 \\ 1 & 0 & 0 & 1 \\ 0 & 1 & 1 & 0 \end{pmatrix} \tag{3.12}$$

with the eigenvalues $(2, 1, -1, -1)$; the respective matrix for (3.10) is

$$\begin{pmatrix} 1 & 1 & 0 & 0 \\ 1 & 1 & 0 & 0 \\ 1 & 0 & 0 & 1 \\ 0 & 1 & 1 & 0 \end{pmatrix}, \tag{3.13}$$

its eigenvalues being $(2, 1, 0, -1)$. In neither of these two cases is the PV condition fulfilled: along with the eigenvalue 2 one has to do with several marginal eigenvalues belonging to the unit circle.

To get an idea of the spectral properties of $\{\Pi_j\}$ and $\{\Upsilon_j\}$ one can further exploit the associated matrices (3.12) and (3.13), similarly to the technique used in [7] for studies of quasiperiodically ordered short and long bonds on the line. To our mind, however, the other recursive way to build the same symbolic sequences looks more appropriate for this purpose: to produce them with the help of the concatenation rules.

Concatenation of two strings is simply writing the second after the end of the first. In the following, the very last letter of a string Ψ will be denoted as $\psi_{\rm E}$, and the string Ψ *without* this last symbol will be denoted as $\psi_{\rm B}$ (thus $\Psi = \psi_{\rm B}\psi_{\rm E}$). For a binary string, the overbar will denote the ="mirror image": given the string A, the string $\overline{A}$ defines the string in which each 1 (or, in our context, R) of A is changed to -1 (L) and vice versa.

The concatenation rule for building the Thue-Morse sequence has been already demonstrated above while describing the scenario of homoclinic doublings. The string $\Psi^{(n+1)}$ obtained from $\Psi^{(1)} = R$ after n concatenations, consists of 2^n symbols and is produced by appending to $\Psi^{(n)}$ its opposite:

$$\Psi^{(n+1)} = \Psi^{(n)}\overline{\Psi^{(n)}} \tag{3.14}$$

The analogous rule for the period-doubling code involves two steps. At first, $\Psi^{(n)}$ is concatenated with itself: $\Psi^{(n)} \to \Psi^{(n)}\Psi^{(n)}$, and then the very last letter of the resulting word is converted to the opposite one: $R \leftrightarrow L$.

$$\Psi^{(n+1)} = \Psi^{(n)}\psi_{\rm B}^{(n)}\overline{\psi_{\rm E}^{(n)}} \tag{3.15}$$

Evaluation of the respective spectral sums $S(\omega, l)$ shows that the power spectrum is discrete for eq.(3.15) and singular continuous for eq.(3.14) (see e.g. [49]).

In order to take account for the residence durations, the rules (3.14,3.15) require only a slight modification: in each case the last letter of the concatenated word should be repeated. This yields

$$\Psi^{(n+1)} = \Psi^{(n)}\overline{\Psi^{(n)}\psi_{\mathrm{E}}^{(n)}} \tag{3.16}$$

for the code $\{\Upsilon_j\}$, and

$$\Psi^{(n+1)} = \Psi^{(n)}\psi_{\mathrm{B}}^{(n)}\overline{\psi_{\mathrm{E}}^{(n)}\psi_{\mathrm{E}}^{(n)}} \tag{3.17}$$

for the code $\{\Pi_j\}$, respectively. Besides, the initial condition should be reformulated: now $\Psi^{(1)}$ is a string of $\tau_0 + 1$ symbols R. Obviously, in both cases after n concatenations the resulting object consists of $l_n = (\tau_0 + 2)2^n - 1$ letters and is identical with the string obtained by applying n respective substitutions to the same initial word.

3.6 Spectral characteristics of symbolic codes

Let us proceed with the estimation of the spectral sums $S(\omega, l_n)$. We begin with the code $\{\Upsilon_j\}$ derived from the Thue-Morse sequence. Consider $Z_n(\omega) = \sum_{k=1}^{l_n} \Upsilon_k \mathrm{e}^{2\pi\mathrm{i}\omega k}$. From eq.(3.16) follows:

$$Z_{n+1}(\omega) = Z_n(\omega)(1 - \mathrm{e}^{2\pi\mathrm{i}\omega l_n}) + \Upsilon_{l_{n+1}}\mathrm{e}^{2\pi\mathrm{i}\omega l_{n+1}} \tag{3.18}$$

and, further,

$$\begin{aligned} |Z_{n+1}(\omega)|^2 &= 2|Z_n(\omega)|^2(1 - \cos 2\pi\omega l_n) + 1 \\ &+ \Upsilon_{l_{n+1}}\left(Z_n(\omega)(1 - \mathrm{e}^{2\pi\mathrm{i}\omega l_n})\mathrm{e}^{-2\pi\mathrm{i}\omega l_{n+1}} + Z_n^*(\omega)(1 - \mathrm{e}^{-2\pi\mathrm{i}\omega l_n})\mathrm{e}^{2\pi\mathrm{i}\omega l_{n+1}}\right) \end{aligned} \tag{3.19}$$

In the following we consider only such values of ω for which the spectral sums $S(\omega, l_n) = l_n^{-1}|Z_n(\omega)|^2$ at least do not decay for large n, i.e. for which $|Z_n(\omega)|$ grows not slower than $\sqrt{l_n}$. For these values of ω one can neglect on the right hand size of eq.(3.19) the terms proportional to $\Upsilon_{l_{n+1}}$ (recall that $|\Upsilon_j| = 1$) and the summand 1. For large n this leaves us with

$$S(\omega, l_{n+1}) \approx S(\omega, l_n)(1 - \cos 2\pi\omega l_n) \tag{3.20}$$

We will treat it as an exact recurrent relation; combined with the relationship between l_{n+1} and l_n, this provides us with the two-dimensional mapping

$$S_{n+1} = S_n(1 - \cos 2\pi\theta_n) \tag{3.21}$$

$$\theta_{n+1} = (2\theta_n + \omega) \bmod 1 \tag{3.22}$$

whose orbit starts from initial conditions $S_1 = 1$, $\theta_0 = (\tau_0 + 1)\omega$.

The map (3.21,3.22) is a skew product: the dynamics of the second variable does not depend on the first one. We are interested in the evolution of S_n; its mean growth (or decay) rate is determined by the geometric average $\varrho = \langle 1 - \cos 2\pi\theta_n \rangle$ along the respective orbit of (3.22): $S_n \sim l_n^{\overline{\lambda}}$ where $\overline{\lambda} = \log \varrho / \log 2$.

Generally speaking, (3.22) is a chaotic map with uniform invariant density, a variant of the Bernoulli shift [20], but for each given ω we are interested in the particular orbit starting at θ_0. In terms of the variable $(\theta + \omega)$ the map acquires the familiar Bernoulli form; from this point of view, changing ω in eq. (3.22) is equivalent to changing initial value in the Bernoulli map. If ω is rational, the respective orbit is either periodic or eventually periodic (in the latter case it becomes periodic after a certain initial segment). For the fixed period p ($p = 1, 2, 3, \ldots$) the corresponding values of ω are given by

$$\omega = \frac{l}{(\tau_0 + 2)2^m(2^p - 1)} \tag{3.23}$$

where m is an arbitrary non-negative integer and l is an odd integer between 0 and $(\tau_0 + 2)2^m(2^p - 1)$. For $m \neq 1$ the orbit is eventually periodic: the actual periodic orbit located at

$$\theta = \frac{l}{2^p - 1}\left(1 - \frac{1}{2^m(\tau_0 + 2)}\right) \bmod 1 \tag{3.24}$$

is reached at the $(m-1)$-th iteration of (3.22).

As an example, we present in Table 3.1 the values of $\overline{\lambda}$ for several periodic orbits of (3.22) and compare them to the analogous values evaluated from the sequence $\{\Upsilon_j\}$. In the latter case the estimates to $\overline{\lambda}$ are given by the expression:

$$\lambda_l(\omega) = (p \log 2)^{-1} \log \frac{1 + 2^{1-l} \sum_{k=1}^{2^l-1} (2^l - 1 - j) C(k) \cos 2\pi\omega k}{1 + 2^{1+p-l} \sum_{k=1}^{2^{l-p}-1} (2^{l-p} - 1 - j) C(k) \cos 2\pi\omega k} \tag{3.25}$$

where $C(k)$ is the value of the autocorrelation function for $\{\Upsilon_j\}$. According to numerics, the quite satisfactory convergence of λ_l is attained already for moderate (≥ 12) l's.

Table 3.1: Growth rates of the spectral sums for the sequence $\{\Upsilon_j\}$.

τ_0	p	ω	ϱ	$\overline{\lambda}$	λ_{12}	λ_{13}	λ_{14}	λ_{15}
0	1	3/8	$1+2^{-1/2}$	0.77155	0.77389	0.77246	0.77051	0.76632
0	1	5/16	1.38268	0.46747	0.47425	0.47118	0.47420	0.47088
0	1	1/4	1	0	0.00596	0.00639	0.00414	–0.00024
0	2	1/12	1.36602	0.44998	0.46043	0.45512	0.45339	0.45256
0	2	5/12	0.36602	–1.44998	–0.78587	–0.81555	–0.83187	–0.85719
0	2	5/24	0.75882	–0.39817	–0.34811	–0.35401	–0.38569	–0.38767
1	1	1/3	3/2	0.58496	0.58509	0.58579	0.58760	0.58416
1	2	1/9	1.26604	0.34033	0.34297	0.34105	0.33910	0.34032
1	3	2/7	1.10809	0.14807	0.15206	0.15412	0.15128	0.15044
1	3	9/28	0.91566	–0.12711	–0.11465	–0.11612	–0.11653	–0.12446
1	3	8/21	0.10203	–1.09761	–0.88704	–0.91565	–0.92706	–0.93559

The remarkably good correspondence between the positive growth rates provides an *a-posteriori* justification for our reduction of (3.19) to (3.20). Moreover, the last row of the upper half of the Table and the penultimate row of the lower half display this correspondence even in case of the moderate ($-1/2 < \lambda < 0$) decay of the spectral sums. Only the faster decay (cf. the last row in the Table), as expected, cannot be properly described with the help of relations (3.21,3.22). Consequently, we conjecture that some part of the spectral measure is concentrated on the countable set of the rational values of (ω) with $\overline{\lambda}(\omega) \geq 0$. For all the periodic and eventually periodic orbits with $p > 1$ and nearly all fixed and eventually fixed points with $p = 1$ (the exceptions will be separately discussed below) the value of $\overline{\lambda}$ is distinctly lower than 1; accordingly, the spectral sums grow with n slower than linearly, and the respective values of ω belong to the singular continuous spectral component.

For the irrational values of ω the corresponding orbit of (3.22) is chaotic. The distribution of the invariant measure on the interval $(0, 1)$ is uniform, and for the generic value of ω the rate λ can be computed simply by averaging the ratio $\frac{\log(1-\cos 2\pi\theta)}{\log 2}$ on this interval; this yields $\overline{\lambda} = -\frac{1}{2} - \frac{1}{4\pi} \approx -0.579$ and ensures the rapid decay of the respective spectral sums. However, the Bernoulli map includes also the continuum of trajectories which stay anomalously close to the rational values of ω. Let us pick out from this continuum the trajectories which repeatedly hover near the periodic orbits with positive $\overline{\lambda}$. An iteration of the Bernoulli map is simply a unit shift along the binary representation of the number. One should cut out the very long segments from the binary representations of ω for different periodic orbits with positive $\overline{\lambda}$, and concatenate them into the infinite binary sequence. Obviously, the leftmost segment of the sequence is of no importance, and the orbit can be started arbitrarily close to any given point. This procedure provides a dense non-denumerable set of irrational (if we reject the periodic concatenations) values of ω with $\overline{\lambda}(\omega) > 0$; roughly speaking, this is just the set which carries the spectral measure.

The peculiar circumstance is associated with the value $\omega = \frac{1}{2}$: this is a fixed point of (3.22) for any integer τ_0, and the growth rate for it equals 1: $S(1/2, l_n) \propto l_n$ which produces the δ-peak in the power spectrum. Hence the spectrum should be a mixture of the discrete and the singular continuous component. The visual absence of the former, as implied by the apparent decay of the integrated autocorrelation function $C_{\rm int}(t)$ in Fig.3.3, can be attributed to the weakness of the contribution of the discrete part; this contribution must be especially small, should τ_0 be non-integer (this aspect is further discussed below in the final paragraph of this section).

Now let us turn to the sequence $\{\Pi_j\}$ obtained from the period-doubling code. In this case we have

$$Z_{n+1}(\omega) = Z_n(\omega)(1 + \mathrm{e}^{2\pi \mathrm{i}\omega l_n}) - 2\Pi_{l_n}\mathrm{e}^{2\pi \mathrm{i}\omega(l_{n+1}-1)} + \Pi_{l_{n+1}}\mathrm{e}^{2\pi \mathrm{i}\omega l_{n+1}} \qquad (3.26)$$

and, using the same assumptions as above, the recursion for the spectral sums S_n is derived:

$$S_{n+1} = S_n(1 + \cos 2\pi\theta_n) \qquad (3.27)$$

$$\theta_{n+1} = (2\theta_n + \omega) \bmod 1 \qquad (3.28)$$

The map (3.28) coincides with (3.22); consequently, the same expression (3.23) provides us with the complete list of the values of ω corresponding to periodic

and eventually periodic orbits. On the other hand, the difference between (3.21) and (3.27) means that for each of these orbits the growth/decay rate for the spectral sums of $\{\Pi_j\}$, in general, is not the same as in the case of $\{\Upsilon_j\}$ (Table 3.2). Thus, for the orbit with period 1 the decay for $\{\Pi_j\}$ always implies growth for $\{\Upsilon_j\}$ and vice versa, since the respective values of ϱ are related by $\varrho(\Pi) + \varrho(\Upsilon) = 2$. On the whole, however, we obtain qualitatively the same picture: decay of spectral sums for almost all irrational values of ω and part of the rationals, as opposed to the growth (with $\overline{\lambda} < 1$) of these sums for the rest of the rationals and the remaining dense subset of the irrationals.

Table 3.2: Growth rates of the spectral sums for the sequence $\{\Pi_j\}$.

τ_0	p	ω	ϱ	$\overline{\lambda}$
0	1	3/8	1-$2^{-1/2}$	–1.77155
0	1	5/16	0.61731	–0.69591
0	1	1/4	1	0
0	2	1/12	0.36602	–1.44984
0	2	5/12	1.36602	0.44984
0	2	5/24	0.24118	–2.05181
1	1	1/3	1/2	–1
1	2	1/9	0.26604	–1.91026
1	3	2/7	0.25157	–1.99090
1	3	9/28	0.21360	–2.22696
1	3	8/21	0.10203	0.47403

On the first sight, it may seem that in this situation the discrete component might be absent: although $\theta = 1/2$ remains the fixed point of the map (3.28), the respective growth rate vanishes identically. However, there are countably many eventually periodic orbits of (3.28) with period 1 whose growth rate λ is arbitrarily close to 1. The last iteration on the transient, before reaching the periodic orbit, passes very close to $\theta = 1/2$; respectively, the spectral sum is multiplied by a tiny factor and nearly vanishes after this iteration. The subsequent fast growth begins from the very small starting position; for this reason, to observe the presence of the discrete component, one needs really long samples.

The above discussion refers to the local properties of the spectral measure. The global description should characterize the set which carries this measure as a whole; this would inevitably require the multifractal analysis, because the generalized dimensions D_q of this set are apparently different (thus, its capacity D_0 equals 1, since the values of ω with positive $\overline{\lambda}$ are dense). The complete picture is delivered by the singularity spectrum $f(\alpha)$ (for the applications of thermodynamical formalism to singular continuous spectra see, e.g. [50, 49]); here we will limit ourselves to the numerical estimates for the correlation dimension D_2 of the fractal component of the spectrum. It has been recently proved that in systems with purely singular continuous spectra the correlation dimension of the spectral measure predetermines the decay rate of the integrated autocorrelation function [23, 24]: $C_{\rm int}(T) \sim T^{-D_2}$. Our situation is more complicated: the above analysis predicts the presence of discrete component in the power spectra of both $\{\Pi_j\}$ and $\{\Upsilon_j\}$, which means that $C_{\rm int}(T)$ should not decay to zero but

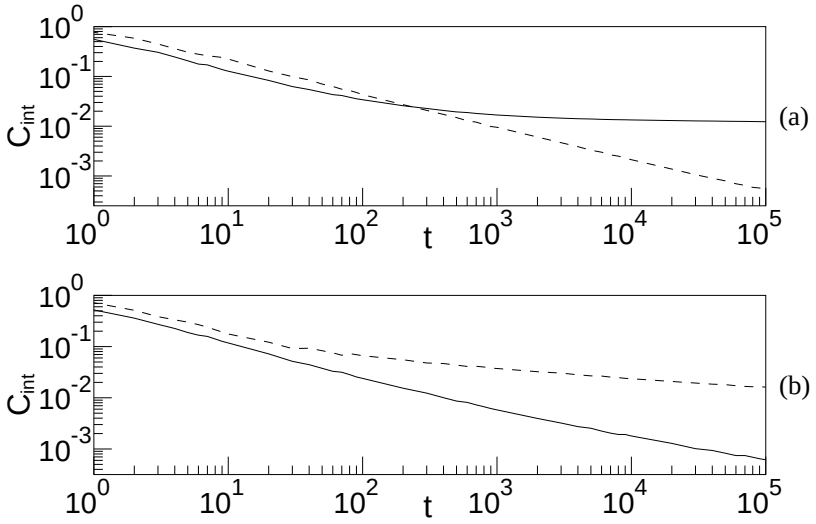

Figure 3.7: Integrated autocorrelation in logarithmic timescale for the observables:
a) symbolic sequence $\{\Upsilon_j\}$: $\tau_0 = 0$ (solid line) and $\tau_0 = 3$ (dashed line);
b) symbolic sequence $\{\Pi_j\}$: $\tau_0 = 0$ (solid line) and $\tau_0 = 3$ (dashed line).

will instead tend to some finite positive value. At present we are not aware of rigorous mathematical relations between the dimensions of the spectral measure and the properties of integrated correlations for the case of mixed power spectra. For this reason we will use the empirical extrapolation from the pure singular case, employed in [63] for the mixed spectrum of the kicked Harpers model. Let the contribution of the discrete spectral component be $C_{\rm int}(\infty) \equiv A \ \ (A > 0)$; we assume that the rate of convergence to A is a reasonably good approximation to D_2: $C_{\rm int}(T) - A \sim \ T^{-D_2}$ and estimate the values of A and D_2 by numerical fitting of the $C_{\rm int}(T)$ dependencies.

Let us take as a reference point the prototype symbolic sequences $\{P_j\}$ and $\{T_j\}$. The spectral measure of the period-doubling code is pure-point, hence for the former $D_2 = 0$. The value of D_2 for the spectral measure of the Thue-Morse sequence equals $3 - \log(1 + \sqrt{17})/\log 2 \ = \ 0.64298\ldots$ [57].

Fitting the data on $C_{\rm int}$ from Fig.3.3, obtained from the integration of the initial continuous system (3.2), we come to the values $A \approx 1.9 \times 10^{-4}$, $D_2 \approx 0.63$ for the variable $x(t)$ and $A \approx 8.1 \times 10^{-4}$, $D_2 \approx 0.56$ for the variable $z(t)$.

Coming now to the corresponding data for $\{\Upsilon_j\}$ (Fig.3.7a), we observe that the weight of the discrete component in the power spectrum is strongly dependent on τ_0: the best-fitted value of A may be as large as 1.2×10^{-2} for $\tau_0 = 0$ and as small as 9.1×10^{-5} for $\tau_0 = 3$. However, this seems to exert little (if at all) influence on the slope D_2: for the checked values $0 \leq \tau_0 \leq 6$ the estimates on D_2 lie within the range $(0.64 \div 0.68)$. Thus we see that, both for the flow and its discrete models, even on the quantitative level the fractal component of the spectral measure, as inherited from the Thue-Morse sequence, does not change its global properties in spite of the action of the logarithmic divergence in the return (residence) times.

The results for $\{\Pi_j\}$ are much less conclusive. Again, the intensity of the dis-

crete spectral component A is strongly influenced by the value of τ_0 (Fig.3.7b). However, here also the slope D_2 exhibits large fluctuations depending on τ_0: from $D_2 \approx 0.58$ for $\tau_0 = 0$ to $D_2 \approx 0.36$ for $\tau_0 = 3$. In the Thue-Morse case, introduction of the residence durations has enforced the onset of a weak discrete spectral component upon the singular continuous background; here, on the contrary, the very existence of the singular continuous part of the spectrum is due to these unequal residence times. For this reason, the properties of the fractal component seem to be very sensitive to the details of the pattern of residence durations.

The final remark concerns the origin of the mixed character of the spectrum. On the first sight, the presence of the discrete spectral component follows from the provision that the time of global reinjection τ_0 should be integer. One can hardly expect that in a generic continuous system the mean time of global reinjection would be commensurate with the average time of hovering near the saddle point. In fact, this provision is formally needed neither for the inflation rules (3.9,3.10) nor for the concatenations (3.16,3.17). The associated substitution matrices are τ_0-independent. The only place where it really matters is the substitution of the "original" symbols R and L into the inflated codes. Should we allow the process to be described in terms of four (and not two) symbols, τ_0 can easily be rendered non-integer. Then the partial spectral sums (3.1) turn into the Fourier integrals, and the assumption that they do not decay when the sample length grows, leads to the very same skew products: (3.21,3.22) for the process obtained from the Thue-Morse sequence and (3.27,3.28) for the suspension over the period-doubling code. Under irrational τ_0 all the periodic and eventually periodic orbits correspond to irrational values of ω; for this reason, say, in the Thue-Morse case, $\theta = 1/2$ would not be a fixed point. However, admission of non-integer values of τ_0 does not provide an ultimate remedy, since for any of these values the eventual fixed points can be found arbitrarily close to $1/2$; respectively, the growth rate $\overline{\lambda}$ can be made arbitrarily close to 1, the corresponding spectral component being indistinguishable from the delta-function. Noteworthy, linear growth starts only after hitting the fixed point, and the preceding transient may well be long. Each new iteration of the skew product is equivalent to the doubling of the sample length; this means that the integer values of τ_0 simply make the discrete component of the power spectrum better resolvable in short samples.

3.7 Discussion

Self-similar properties of the prototype Thue-Morse and period-doubling symbolic sequences play the crucial role in our derivation of substitution and concatenation rules for the processes with logarithmic singularities of return times. Although inherent for the scenario of "homoclinic doublings", these properties are absent in the general case when the flow does not possess the Lorenz-like mirror symmetry, and the road to chaos through the homoclinic bifurcations in the parameter space follows one of the multitude of the possible routes [15, 16, 17]. All of these routes are associated with unbounded times of return on the secant surface (and hence, for all of them the flow is not equivalent to the Poincaré map), but only a countable subset can be characterized through self-similarities. In the latter case one can build up the corresponding concatenation rules and

examine with their help the laws which govern the growth of the spectral sums; in the more general case a kind of a statistical approach could be more helpful.

The same methods can be applied to other situations in which the origin of the singular continuous spectral component is related to singularities of return times: e.g. in Hamiltonian flows on a 2-torus with saddle points and irrational rotation numbers [64, 38], or in the hydrodynamical variant of the problem: the forced steady flow of a viscous fluid on a doubly periodic domain in presence of a mean drift [65].

In the paper we have demonstrated that particular mechanisms for the appearance of multifractal power spectrum in continuous dissipative systems can be adequately described by means of symbolic dynamics. In fact, the role played in the above analysis by the dissipative character of the flow, is restricted to the effective reduction of dynamics to one-dimensional maps; the proper account of the logarithmic divergence of return times seems to be more important, and we expect that similar considerations should work also in the context of low-dimensional conservative systems. An open question remains, whether an adequate symbolic description is possible for a general continuous flow. As soon as such description is obtained, the well-developed theory of spectral properties of symbolic sequences [21] can serve as a basis for understanding dynamical systems at the border between order and chaos.

Chapter 4

Fractal Fourier spectra of Cherry flows

4.1 Introduction

Equations reducible to flows on 2-tori are encountered in different branches of science. In many cases, such dynamical systems possess no steady states: thus, in the textbook example of a 2-torus flow governing the dynamics of a periodically perturbed oscillator, the monotonic growth of the phase of the force forbids the existence of static equilibria. However, flows on 2-tori arise also in the autonomous setup where the evolution does not need to be monotonic. Examples of vector fields on low-dimensional tori which possess fixed points, appear in various physical contexts: charged particle transport in toroidal plasma fusion devices in the approximation of several electrostatic plane waves [66, 67], charge-density wave transport[68], forced two-dimensional viscous flows [65], phase approximation to the dynamics of coupled solid state lasers interacting with an injected field [69], etc.

Since chaos in a continuous dynamical system is only possible if the dimension of its phase space exceeds two, dynamics on two-dimensional manifolds may appear simple. However, the question about the spectral properties of such flows is still not completely answered. Kolmogorov proved that the spectrum of a Hamiltonian flow on a 2-torus with an irrational rotation number is discrete, provided that two conditions are satisfied: the flow has no fixed points, and the rotation number cannot be anomalously well approximated by rationals [34]; his conjecture that violation of the latter condition could produce continuous spectrum, was later confirmed in [70]. Spectral properties are related to the ergodic property of mixing [20]; absence of mixing for a flow without fixed points on a 2-torus was demonstrated in [71]. In the present analysis, we remove the remaining restriction and allow the vector field to possess fixed points. According to numerical results, in this case the Fourier spectrum of the trajectory with irrational rotation number is supported by a fractal set.

In Sect.4.2 an exemplary 2-parameter family of equations on a 2-torus is introduced. In Sect.4.3 the characteristics of the Fourier spectral measure are discussed. Numerically evaluated autocorrelation function indicates that the power spectrum of the flow with irrational rotation number is neither discrete

nor absolutely continuous but fractal. A straightforward symbolic description based solely on topology of the orbit, fails to reproduce the unusual spectral properties of the flow. This discrepancy is due to the extreme variation of return times which is not contained in the Poincaré map. Sect.4.4 describes modification of the symbolic representation by incorporating metric information about dynamics. For this purpose, we utilize the fact that the return map is a discontinuous circle map for which the accumulation of closest returns to the critical point is described by the superexponential scaling law. The modified substitution rule produces a symbolic code whose spectral characteristics are in good correspondence with those of the original continuous flow. In the concluding part of the paper we argue that our particular example represents a typical case and, hence, the results apply to a wide class of flows with fixed points on the 2-torus.

4.2 A sample Cherry flow

In the generic case of a flow with fixed points on a 2-torus, at least one of these points should be a saddle. For the flows with rational rotation numbers, existence of saddle points permits the formation of homoclinic trajectories which can give birth to the respective closed orbits. The implications in the case of irrational rotation numbers are more far-reaching. The qualitative differences were described by Cherry [72] who constructed an analytical example of a vector field on a torus with a saddle, a source and non-trivial recurrent trajectories. By the term "Cherry flow" we will denote below a flow on a 2-torus which has fixed points and an irrational rotation number. We restrict ourselves to the simplest example when there are only two fixed points (Fig.4.1a), one of them a saddle and the other one a source: the latter may be either an unstable node or an unstable focus. Flows with one sink and one saddle turn into our case when viewed in reversed time. For the description of geometric properties of Cherry flows see e.g. [73, 74]; typical bifurcation sequences were investigated in [75].

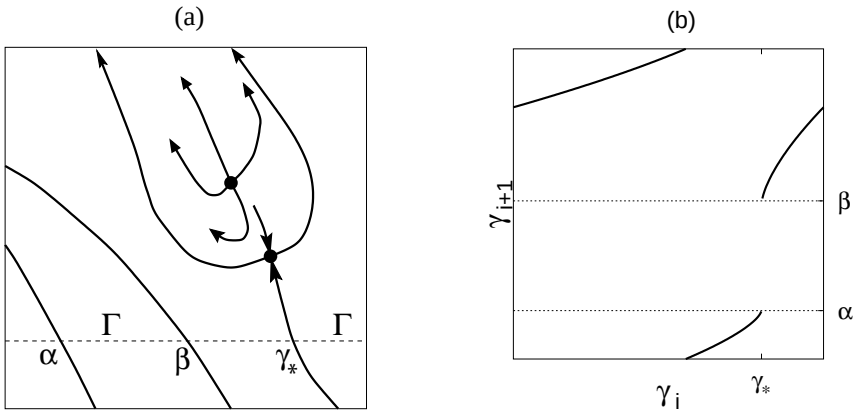

Figure 4.1: (a) Geometry of the Cherry flow; Γ: global secant on the torus; α, β, γ_*: intersections of Γ with invariant manifolds of the saddle point.
(b) Return mapping on Γ (γ: coordinate along the secant).

As an example, we consider the family

$$\begin{aligned} \dot{x} &= 1 + \sin y - \sin x \sin y \\ \dot{y} &= b + \cos x - K \cos x \cos y \end{aligned} \tag{4.1}$$

which is a generalization of equations arising in the context of forced spatially periodic steady motions of incompressible viscous fluid [65]. The algebraic expressions which, in terms of parameters b and K, ensure the existence of steady solutions of Eqs.(4.1), are too cumbersome to be quoted explicitly; below we deal with the ranges of values of b and K where such solutions are present.

To compute the rotation number on the torus T^2, we introduce a lift of the flow from T^2 to the plane R^2 [75]. For the case of a flow with a source, take the initial conditions (x_0, y_0) which do not belong to the stable manifold of a fixed point, and consider the forward limits of $x(t)$ and $y(t)$. The rotation number is defined as $\rho = \lim_{t\to+\infty} y(t)/x(t)$. If the flow has a sink instead of a source, the initial conditions should be chosen outside the unstable manifold of the saddle point, and the limit should be taken at $t \to -\infty$; for the conservative case, either of the limits will do.

We begin with this conservative flow. At $K = 1$ Eqs.(4.1) describe an area-preserving flow with the Hamiltonian $H(x, y) = -x + by - \cos y - \sin x + \sin x \cos y$. For $-1.56644 < b < 1.56644$, the vector field has two fixed points: a center and a saddle. The center is surrounded by closed curves which fill the "vortex" V encircled by the separatrix of the saddle point (Fig.4.2a). The rotation number for the points outside the vortex equals b; under irrational values of b each orbit which starts outside the vortex, is dense in $T^2 \setminus V$.

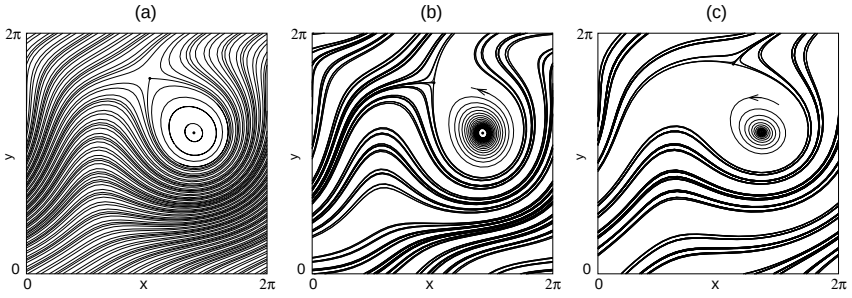

Figure 4.2: Phase portraits of Eqs.(4.1) for flows with inverse golden mean rotation number.
(a) Hamiltonian flow: $K = 1, b = (\sqrt{5} - 1)/2$; (b) saddle and source: $K = 3/2, b = 0.58766578\ldots$; (c) saddle and sink: $K = 1/2, b = 0.60398604\ldots$.

The situation for $K \neq 1$ is different. The degeneracy is removed, the continuum of closed curves disappears, and for $K > 1$ the center turns into the unstable focus (Fig.4.2b); for $K < 1$, the center becomes the stable sink (Fig.4.2c). In both cases the dense covering of the torus is replaced by the Cantor-like pattern.

The bifurcation diagram of Eqs.(4.1) on the plane of parameters b and K is briefly described in the Appendix. On this plane, Cherry flows exist on the continuum of curves; the curve which corresponds to a flow with rotation number ρ, passes through the point $(b = \rho, K = 1)$. We choose the curve corresponding to the inverse "golden mean" rotation number: $\rho = \sigma^{-1} = (\sqrt{5} - 1)/2$. A

typical phase portrait of the attracting set is shown in Fig.4.2b; here, $K = 3/2$ and $b = 0.58766578\ldots$. In the course of winding around the torus, the orbit approaches the saddle point and departs from it; the distance between the orbit and the saddle is not bounded from below. During such passages the velocity of the imaging point can become arbitrarily small. This property has been shown to lead to the presence of the fractal component in the power spectrum [49].

4.3 Autocorrelations and Fourier spectra on orbits with irrational rotation numbers

Since we expect that the support of Fourier spectra can be concentrated on fractals, direct numerical computation of such spectra may prove to be a fragile procedure. For this reason, instead of insecure estimates in the frequency domain, we will mainly work in the time domain and use the more robust tool: the autocorrelation function $C(\tau)$ defined in Eq.(1.1). If the observable is a periodic function of time, its $C(\tau)$ is also periodic, with maximal values equal to 1. For quasiperiodic motions, the values of τ which correspond to the peaks of $C(\tau)$, form a progression in which the ratios of consecutive terms yield the best rational approximations to the irrational rotation number; the magnitude of these peaks tends to 1. For the chaotic and stochastic processes, the increase of τ is accompanied by the asymptotic decay of $C(\tau)$.

Autocorrelation is the Fourier image of the spectral measure $\mu(\omega)$: $C(\tau) = \int d\mu(\omega)\, \exp(2\pi \mathrm{i}\omega\tau)$. There always exists a uniquely determined decomposition of the spectral measure into the pure-point component (discrete power spectrum) and the continuous one [76]. The latter, in its turn, is further decomposable into a part which is absolutely continuous with respect to Lebesgue measure (absolutely continuous power spectrum) and a singular continuous part supported by a fractal set. This singular continuous spectral component will be a main object of our interest.

Along with $C(\tau)$ we will also employ the integrated autocorrelation $C_{\mathrm{int}}(T)$ introduced in Eq.(1.3). Recall that behavior of these two functions at asymptotically large argument values characterizes the spectral measure:

a) a necessary condition for a spectral measure to be purely absolutely continuous is the decay of autocorrelation: $\lim_{\tau\to\infty} C(\tau) = 0$ [20];

b) contribution of the pure point component into the power spectrum is proportional to $\lim_{T\to\infty} C_{\mathrm{int}}(T)$ [53].

Hence, if for sufficiently long time intervals the integrated autocorrelation decays to (nearly) zero, one can conjecture that the power spectrum includes no discrete component. If, further, the autocorrelation function itself does not display the tendency to a complete decay, the absolutely continuous component of the spectral measure also appears to be absent. Consequently, the process has a singular continuous Fourier spectrum. Further, as discussed in previous chapters, the knowledge of the power law which characterizes the decay rate of $C_{\mathrm{int}}(T)$, allows one to evaluate the fractal properties of the set which supports the spectral measure: namely, to estimate its correlation dimension (for the connections between the products of autocorrelations and the values of the other generalized fractal dimensions D_q, see Section 2.5 above and [77]).

For computational purpose, it is convenient to "unfold" a torus onto a plane and consider an observable which is a continuous periodic function of coordinates x and y; immediate candidates are trigonometric functions like $\cos x$.

Typical autocorrelation functions for the flows whose rotation number equals the inverse golden mean, are presented in Fig.4.3; note the logarithmic timescale. Within the plotted time intervals the orbit performs ∼3000 turns around the torus. The parameter values in Fig.4.3a and Fig.4.3b correspond to the phase portrait shown in Fig.4.2b; the flow at $K = 2, b = 0.513061539446796\ldots$ used for the plots in Fig.4.3c and Fig.4.3d, is qualitatively similar to Fig.4.2b. Finally, the plots of autocorrelations in Fig.4.3e and Fig.4.3f correspond to the quasiminimal set of the vector field from Fig.4.2c which has a saddle and a sink (recall that under $K < 1$ one of the fixed points is a stable focus).

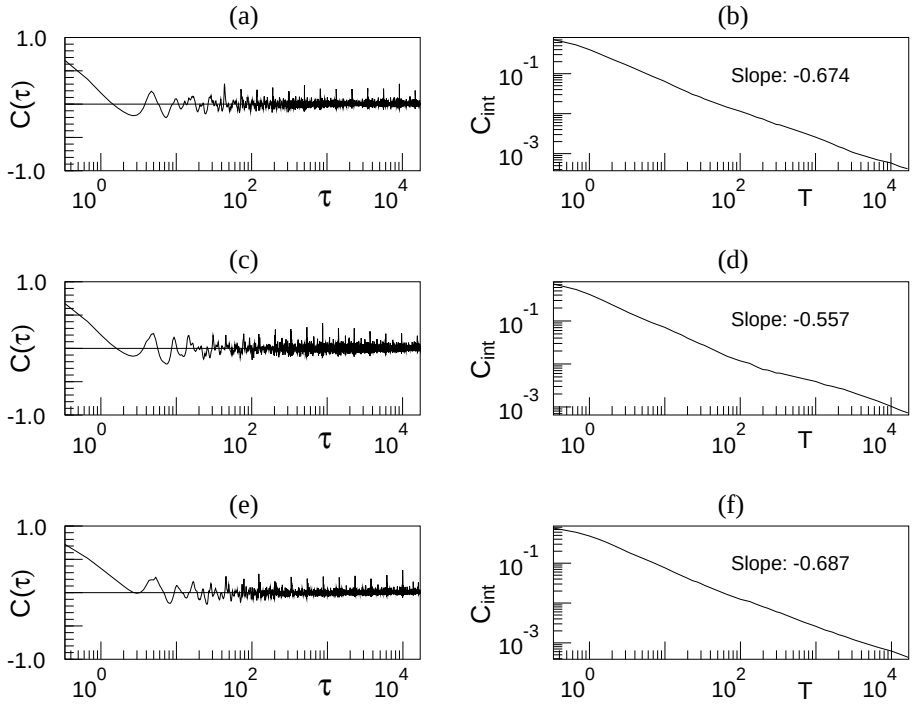

Figure 4.3: Autocorrelation of observable $\cos x$ in flows with golden mean rotation number:
(a),(b): $K = 3/2; b = 0.58766578\ldots$ (vector field from Fig.4.2b);
(c),(d): $K = 2; b = 0.51306153\ldots$;
(e),(f): $K = 1/2; b = 0.60398604\ldots$ (vector field from Fig.4.2c).

As recognizable in the plots, the autocorrelation $C(\tau)$ does not return to the value of 1; this underscores the difference from the case of quasiperiodic dynamics. On the other side, repetitive minor peaks of $C(\tau)$ imply that the power spectrum cannot be absolutely continuous. On the logarithmic axis, the highest peaks form a nearly regular lattice; they are separated by the distance $\approx \sigma = (\sqrt{5}+1)/2$. As visualized by the plots of the integrated autocorrelation which is apparently decaying, the spectrum also cannot include the discrete component. We can conjecture that the power spectrum is singular continuous;

the dimension of the fractal set which supports the spectral measure, can be estimated from the slope of the $C_{\rm int}(T)$ on log-log plots.

4.4 Symbolic coding

In this section, dynamics of the continuous flow is reduced to a much simpler discrete object: the sequence built over the finite set of symbols. Our aim is to obtain a symbolic string which adequately reproduces the spectral and correlation properties of the flow.

The most straightforward way to introduce the symbolic coding of the orbit involves the Poincaré map induced by the flow. Due to the presence of fixed points on the surface of the torus, such maps differ qualitatively from conventional circle mappings. Let us briefly describe their basic properties.

Let Γ be a global secant on the torus (Fig.4.1a). Since two separatrices of the saddle point return onto Γ in two different places (denoted, respectively, by α and β), the 1-dimensional map ϕ induced on Γ is not homeomorphic: not all of the points of Γ have preimages. This is a discontinuous circle map with a gap (Fig.4.1b). Since during the passage near the saddle the linear terms of the equations dominate, close to the discontinuity the mapping is described by the power law: for small positive ε, $\phi(\gamma_* + \varepsilon) - \beta \sim \varepsilon^\nu$, and $\alpha - \phi(\gamma_* - \varepsilon) \sim \varepsilon^\nu$. Here the saddle index $\nu = -\lambda_s/\lambda_u$ is the ratio of the negative eigenvalue λ_s and the positive eigenvalue λ_u of the Jacobian of the vector field taken at the saddle point. The properties of families of circle mappings with gaps were previously considered in the context of sequences of homoclinic ("gluing") bifurcations for flows in R^n, $n \geq 3$ [15, 16, 17, 30]. The peculiarity of these mappings is the superexponential scaling near the irrational rotation numbers, both in the parameter space and along the state variable; the reason for this unusual scaling lies not in the power-law character of the map (the piecewise-linear map demonstrates it as well), but in the presence of the discontinuity. The flow with a sink is described by the same mapping in the reversed time. In this case the mapping is not everywhere defined on Γ: the backward orbits which start between the points α and β in Fig.4.1a end up in the sink and never return onto Γ. On extending the map to the whole of Γ by prescribing a constant value on $[\alpha, \beta]$, one arrives at the circle mapping with a flat interval. Such mappings have also been an object of extensive studies [78, 79, 80, 81]. Thus, it has been proven that, under $\nu > 1$, the Hausdorff dimension of the non-wandering set of the map is strictly less than one [80]. For the opposite case of expanding maps with flat intervals, the Cherry flows have been shown to be, in a certain sense, "rare": parameter values corresponding to irrational rotation numbers have in the parameter space not only zero Lebesgue measure but also zero Hausdorff dimension [78]; under certain additional technical assumptions, each recurrent set of Γ with irrational rotation number has Hausdorff dimension zero [79].

The Poincaré map has one discontinuity and consists of monotonic branches; this suggests that the alphabet consisting of two symbols is sufficient for the adequate description of dynamics: the symbols mark the passages e.g. "below" and "above" the saddle point. The symbolic code for the inverse golden mean rotation number is the Fibonacci symbolic sequence $ABAABABA\ldots$ which can be obtained from the initial symbol A by means of repetitive substitutions (inflations) $\{A \to AB,\ B \to A\}$. On assigning to A and B numerical values, a

symbolic code is turned into a sequence of numbers which can be further treated as time series. In this way the metric characteristics of the sequence (autocorrelation, Fourier spectrum, entropies, etc.) can be evaluated. The straightforward computation shows that the autocorrelation function $C(\tau)$ displays repetitive returns arbitrarily close to 1 (Fig.4.4a); hence, the power spectrum of the Fibonacci sequence is discrete. We see that the Fibonacci code, albeit correctly reproducing the pattern which the orbit follows during its winding around the torus, fails to reproduce the spectral properties of the Cherry flow. This does not mean that the chosen symbolic coding is not appropriate for the Poincaré map; the reason is deeper: the map itself also appears to have a discrete power spectrum (Fig.4.4b). Hence, the Poincaré map does not share the spectral properties of the underlying flow.

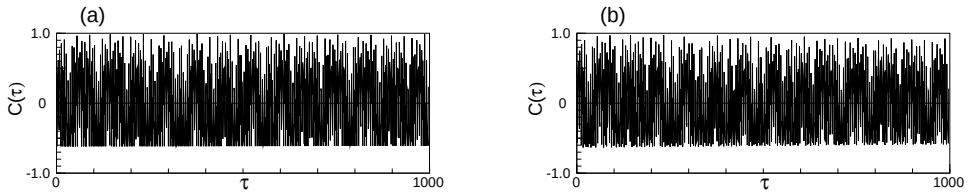

Figure 4.4: Autocorrelation function for: (a) Fibonacci symbolic code; (b): Poincaré mapping induced by the flow from Fig.4.2b.

The situation in which the flows and their Poincaré maps have qualitatively different Fourier spectra, was discussed in [49]; the reason was found to lie in the unboundedness of the return times onto the Poincaré surface in the phase space, resulting from presence of saddle points in the attractors of corresponding flows. In the case of Cherry flows the same mechanism is in action: trajectories can approach the saddle point arbitrarily close, and the time intervals between the returns onto a secant Γ can be arbitrarily long. The cause of the discrepancy is obvious: in the straightforward symbolic representation all turns of the trajectory around the torus are treated equally: each one, irrespectively of its temporal duration, is represented by a single symbol. The duration is characterized through strong variations: the turns during which the orbit passes close to the saddle point, require rather long time intervals. Consequently, the contribution of the protracted turns into the computation of averaged characteristics of the orbit, like the power spectrum, autocorrelation function etc., is significantly larger than that of the faster turns; this circumstance remains ignored by the Poincaré map.

To obtain an adequate symbolic description which recovers the metric characteristics of the process, one has to take into account the slowdown of the flow in the neighborhood of the saddle point. Certain symbols in the Fibonacci code must be doubled, tripled etc, depending on the length of the corresponding time intervals. Consider the Poincaré secant Γ parameterized by coordinate γ; let γ_*, as above, denote the coordinate of the intersection of Γ with the local stable manifold of the saddle point (Fig.4.1a). The length τ_{r} of the time interval until the next return of an orbit onto Γ is a function of γ; it is easy to estimate that this function has a logarithmic singularity in the point γ_*:

$$\tau_{\mathrm{r}}(\gamma) \sim -\log|\gamma - \gamma_*| \tag{4.2}$$

The multiplicity (the number of repeats) of each symbol in the code should be proportional to the corresponding $\tau_{\rm r}$. In order to characterize the weight with which the individual symbols in the code contribute into the averaged characteristics, let us follow the approach of [82] and introduce the "residence time" R for the symbols. For the j-th symbol this time $R(j)$ is given by the length of time interval between the j-th and the $j+1$-th crossings of the Poincaré secant by the orbit starting at γ_*. (Strictly speaking, the orbit starting exactly at γ_* belongs to the local stable manifold of the saddle and never returns onto Γ; here and below under images of γ_* we mean, for shortness, either of the one-sided limits for $\gamma \to \gamma_*$; these limits correspond to two components of the unstable manifold of the saddle).

To estimate the distribution of residence times, scaling properties of the orbit should be taken into account. In the example of [82] the logarithmic singularity of return times was combined with the geometric (exponential) scaling on the attractor. In Cherry flows the situation is qualitatively different, and the construction of [82] cannot be directly applied. As already mentioned, in contrast to vector fields on tori without fixed points where under irrational rotation numbers the trajectories are dense, the trace of a Cherry flow on the secant Γ is a Cantor set (cf. Fig.4.2b). Keeping the inverse golden mean rotation number, consider the "Fibonacci returns" for the Poincaré mapping ϕ: the F_n-th images of γ_* where F_n is the n-th number in the Fibonacci series $\{1, 2, 3, 5, 8, 13 \ldots\}$ [1]. The "odd" (corresponding to the odd n) and the even Fibonacci returns accumulate to γ_* from two opposite sides; as known from the analysis of gap maps [16, 17, 30], this accumulation is characterized through the superexponential scaling:

$$|\phi^{F_{n+2}}(\gamma_*) - \gamma_*| \sim |\phi^{F_n}(\gamma_*) - \gamma_*|^{\kappa} \tag{4.3}$$

where the rate of accumulation κ, in its turn, depends on the saddle index ν. The analysis of the corresponding renormalization operator shows that the relevant fixed point is singular: the renormalizing transformation cannot be properly linearized in its vicinity. For the values of ν close to 1 the respective κ can be estimated [17, 30] as

$$\kappa(\nu) \approx \nu + \frac{\nu^2 + \sqrt{\nu^4 + 4\nu^3}}{2} \tag{4.4}$$

When n is large enough, the most part of $\tau_{\rm r}$ for the F_n-th return is spent in a very slow motion near the saddle point, and the contribution of relatively fast "global" passage around the torus is negligible. Combining (4.2) with (4.3), we obtain the residence times for the symbols with numbers F_n:

$$R(F_n) = \tau_{\rm r}\left(\phi^{F_n}(\gamma_*)\right) \sim G_{\rm o,e}\kappa^{n/2} \tag{4.5}$$

where the constants $G_{\rm o,e} > 1$ refer to odd and even n, respectively. According to Eq.(4.5), residence times for the Fibonacci returns form two geometric progressions with the same exponent κ.

The Cantor set on Γ has a hierarchical structure: it is composed of "clusters"; each cluster is organized around one of the Fibonacci returns; inside each cluster

[1] Naturally, the full Fibonacci series reads $\{1, 1, 2, 3, 5, 8, \ldots\}$; to simplify the notation, we start the enumeration from zero: $F_0 = 1, F_1 = 1, \ldots$, and do not use the zeroth term.

one observes the next level of self-similar hierarchy, and so on. As n grows, the size of the n-th cluster rapidly (obeying the double-exponential law) decreases. Since the gaps which separate the clusters are large compared to the cluster sizes, we can neglect the variation of return time inside each cluster. Therefore, as the representative timescale for each cluster we choose the value of $\tau_{\rm r}$ for the Fibonacci return from this cluster, as given by Eq.(4.5). Then, to compute the residence time for the j-th symbol in the code, one needs only to determine the number $N(j)$ of the cluster to which belongs the j-th image of γ_*. This $N(j)$ can be determined with the help of so-called Zeckendorf expansion [83] through which each natural number is in the unique way represented as a sum of non-neighboring Fibonacci numbers (e.g. 16=13+3, 133=89+34+8+2, etc.). The value of $N(j)$ is given by the place which the last (the smallest) term in the Zeckendorf expansion of j occupies in the Fibonacci series $\{1, 2, 3, 5, 8, 13 \ldots\}$. For the above examples, $N(16) = 3$ (the smallest term in the expansion is 3, which is the 3-rd Fibonacci number), $N(133) = 2$; obviously, $N(F_n) = n$. In this way, the residence time for j-th symbol becomes

$$R(j) = R\left(N(j)\right) = G\kappa^{N(j)/2} \tag{4.6}$$

where $G = G_{\rm o}$ ($G = G_{\rm e}$) if $N(j)$ is odd (even).

Since the residence time $R(j)$ effectively accounts for the contribution of the j-th turn of the orbit into the averaged characteristics, one can attempt to recover these characteristics numerically by computing them for the step function which admits only two values 1 and 0. In the plot of this function the j-th plateau has the height 1 if the j-th symbol of the Fibonacci code is A, and the height 0 if the respective symbol is B; the length of the j-th plateau is $N(j)$. Applied to the Fibonacci code, this procedure allows to recover fractal power spectra. On the symbolic level this means that the j-th letter in the symbolic Fibonacci code should be replaced by a string of $R(j)$ identical letters. In general, this does not work out, since the rate κ is non-integer, and we obtain the non-integer multiplicity for $R(j)$. A convenient integer example is delivered e.g. by $\kappa = 2$; according to Eq.(4.4) this requires the value of the saddle index $\nu \approx 2\sqrt{2} - 1 = 0.8284\ldots$ which in the Eqs.(4.1) corresponds to $K \approx 1.21$. We can choose a time unit to be $G_{\rm o}$ and include $\kappa^{1/2}$ into the rescaled $G_{\rm e}$, then $R(F_{2n+1}) = \kappa^n$ and $R(F_{2n}) = G_{\rm e}\kappa^n$. Under $G_{\rm e} = 2$, this produces from the Fibonacci code $ABAABABA\ldots$ the string

$$A^{(1)}B^{(2)}A^{(2)}A^{(1)}B^{(4)}A^{(1)}B^{(2)}A^{(4)}\ldots \tag{4.7}$$

where the bracketed indices denote the residence times, in other words the multiplicities with which the respective letters should be repeated.

The very same symbolic string (4.7) can be produced in a different way, with the help of the substitution rule applicable to the case of integer κ. The rule combines two parts: a part, responsible for the correct ordering of the orbit, and a part which reflects the growth of residence times due to hovering near the saddle after Fibonacci returns. Since the topology of the orbit is the same as for the flow without fixed points, the first part must be the Fibonacci substitution $\{A \to AB,\ B \to A\}$. The action of the second part should elongate the sequence for A; let us use the symbol D for the added "hovering" segment: $A \to ABD$. The substitution rule for D is $D \to C$, where C denotes the "hovering part" of the previous Fibonacci return. In its turn, after the substitution C is replaced

by two (three in case of κ=3, etc.) symbols D: $C \to DD$. Assembling the parts together, we obtain an inflation rule acting on an alphabet of four letters:

$$A \to ABD, \quad B \to A, \quad C \to DD, \quad D \to C \tag{4.8}$$

It should be kept in mind that both A and C refer to the same branch of the Poincaré map; the other branch is represented by B and D. For this reason, while computing the quantitative characteristics of the symbolic sequence, the numerical values should be assigned to the letters pairwise: e.g. $A = C = 1$, $B = D = 0$.

The autocorrelation function and integrated autocorrelation for the symbolic code built with the help of the rule (4.8) are presented in Fig.4.5a,b respectively. Modification of the rule allows to reproduce the qualitative properties of the autocorrelation function computed directly from the orbit of the Cherry flow (cf. Fig.4.3a,c,e): the observed structure has moderate, log-periodic in τ peaks, typical for systems with singular continuous spectra. The quantitative correspondence, as measured by the logarithmic period which is close to the golden mean $\sigma = (\sqrt{5}+1)/2$, and by the decay rate of the integrated autocorrelation, is also quite satisfactory.

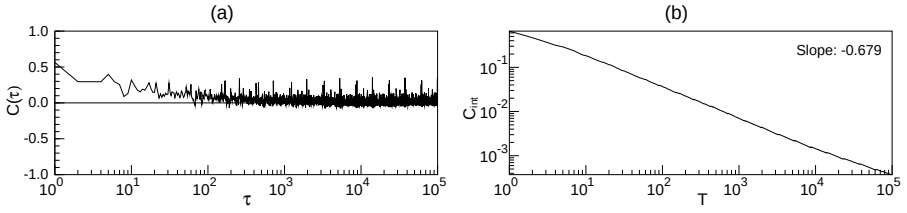

Figure 4.5: Characteristics of symbolic code produced by substitution rule (4.8). Code length: 4×10^6; (a) correlation function; (b) integrated autocorrelation.

4.5 Discussion

In order to obtain the symbolic sequence with correct spectral characteristics, the topological properties of the trajectory (ordering of the turns, as reflected by the Fibonacci code) should be combined with its metric properties (supexponential scaling of the nearest returns) and its dynamical characteristics (logarithmic divergence of return times). The crucial role is played here by the neighborhood of the saddle point. Each generic observable on the trajectory remains nearly constant during the long hoverings near the saddle; the durations and ordering of these hoverings are governed by the properties of the trajectory (and not of the observable itself). Therefore the singular continuous component should be present in the Fourier spectral measure of a generic observable.

Although the above results concentrate on the particular rotation number, they seem to be in some sense typical. Logarithmic periodicity for the lattice of peaks of the autocorrelation function follows from the periodicity of the expansion of the rotation number into the continued fraction: $\sigma^{-1} = \{1, 1, 1, \ldots\}$.

The inverse golden mean σ^{-1} is slowly approximated by rationals; denominators of successive approximants F_n/F_{n+1} differ by a factor which tends to σ with $n \to \infty$. This growth factor determines the distance between the highest peaks of the autocorrelation function on the logarithmic timescale. For other "noble" irrationals (numbers with periodic expansions into continued fractions) log-periodicity of the peak lattice should persist; however, the convergence of approximants is faster, hence the peaks are more seldom. This is illustrated by Fig.4.6a where the autocorrelation function is plotted for the Cherry flow with the "silver mean" rotation number $\sqrt{2}-1 = \{2, 2, 2, \ldots\}$. For a "generic" rotation number, there is no periodicity among the coefficients of the continuous fraction expansion; hence the peak pattern is irregular. This can be seen in Fig.4.6b, where $C(\tau)$ is computed for the "randomly chosen" rotation number $0.441756079565\ldots = \{2, 3, 1, 3, 1, 4, 2, 1, 1, 3, 1, 1, 2, \ldots\}$.

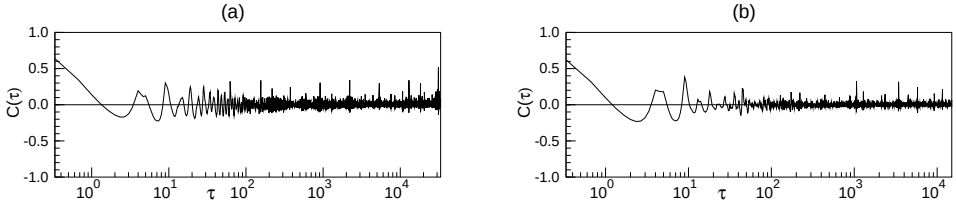

Figure 4.6: Autocorrelation function for Cherry flows at $K = 3/2$:
(a) "silver mean" rotation number; $b = 0.38717552694000980415\ldots$
(b) rotation number 0.441756079565; $b = 0.406982282437618009092\ldots$

The substitution rule on the alphabet of four symbols can be easily generalized for other rotation numbers; the procedure should combine the symbolic 2-letter renormalization known from the usual circle map [84, 16] and the elongation of residence times, described in the previous section. Thus, for a rotation number with expansion into the continuous fraction $\{n_1, \ldots, n_j, \ldots\}$ substitution on the j-th step should be

$$A \to B^{(n_j-1)}ABD, \quad B \to B^{(n_j-1)}A, \quad C \to DD, \quad D \to C \qquad (4.9)$$

For rotation numbers with periodic or eventually periodic continued-fraction expansions, a finite set of substitutions would alternate in the regular manner, eventually resulting in the ordered lattice of peaks for the autocorrelation function. Non-periodic sequences of continuous fraction entries $\{n_i\}$ would produce disordered symbolic strings and, consequently, disordered peak pattern.

Irrespective of the periodicity of the continued fraction expansion, the presence of singular continuous component appears to be the common property both of Cherry flows and of substitution sequences which mimic this unusual kind of two-dimensional dynamics.

Another aspect which deserves to be mentioned here, is the role of power spectra as a criterion to separate chaotic processes from non-chaotic ones. Among the first tools exploited by experimentalists in their search for chaos in the experimental data was the Fourier analysis of time records [85, 86], with continuous spectra being interpreted as the hallmark of chaotic dynamics, and discrete spectra indicating to non-chaotic behavior. Since that early work, this criterion has been often employed for the identification of the type of dynamics

from experimental and numerical data. The above results suggest that certain precautions should be met: in case of processes with fractal power spectra, finite-length spectral sums may produce the false impression of the absolutely continuous spectrum and, hence, chaotic dynamics. This can be seen in Fig. 4.7 which shows the approximation to the power spectrum of the Cherry flow from Fig.4.2b, estimated from 2^{14} datapoints. Behavior of spectral sums under the increase of the dataset length should be checked: in case of the absolutely continuous spectrum, finite-length approximations converge to a bounded spectral curve, whereas the absence of such convergence indicates to the presence of singularities in the spectral measure.

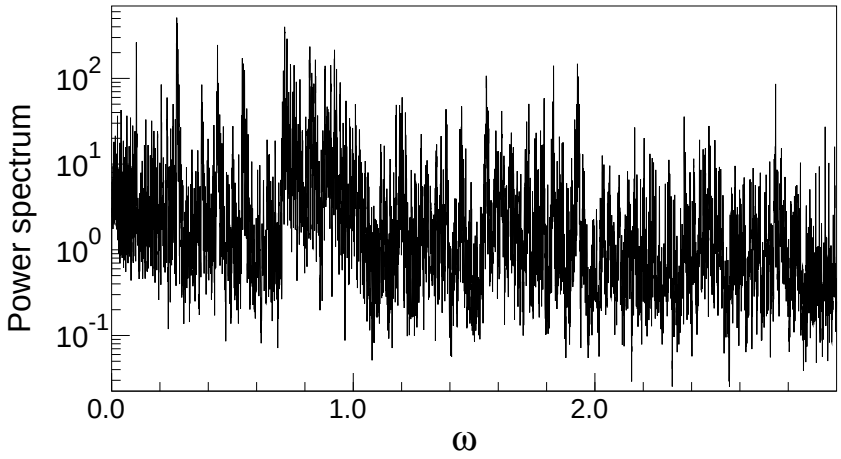

Figure 4.7: Estimation of the power spectrum for the flow from Fig.4.2b. Length of the sample: 2^{14} points.

Appendix: Bifurcation sequences in the family (4.1).

The organizing element for the diagram of states on the parameter plane of the equations (4.1) is the line $K = 1$ on which the dynamics is Hamiltonian, and on which each rotation number ρ is represented by the point $b = \rho$. For rational values of ρ, the existence domains for periodic solutions with the corresponding rotation numbers open from these points into both directions ($K > 1$ and $K < 1$, respectively); for irrational ρ these points belong to the existence curves for the Cherry flows. In Fig.4.8 these domains are presented for the rotation numbers equal to the first 6 ratios of the consecutive Fibonacci numbers F_n/F_{n+1}.

The structure of the parameter plane is reminiscent of two-parameter families with quasiperiodic and periodic dynamics. Similarly to the Arnold tongues in such families, the domains of periodic behavior have wedge-like shape and are bounded by the lines of saddle-node bifurcations. However, in contrast to the Arnold tongues, inside these domains there are additional bifurcation lines which pass through the tips of the wedges: lines of homoclinic bifurcations. These lines divide each "tongue" into the inner region and two narrow sideband strips.

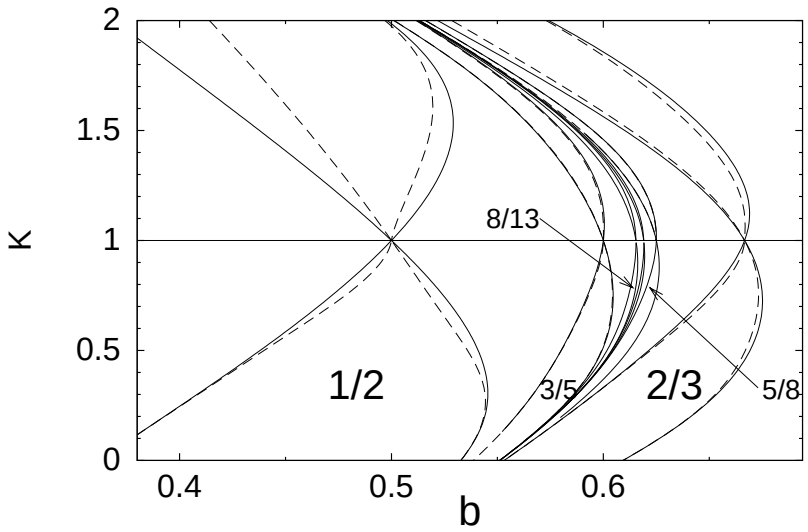

Figure 4.8: Bifurcation diagram of Eqs (4.1). Labels denote rotation numbers; solid lines: saddle-node bifurcations of periodic solutions; dashed lines: homoclinic bifurcations of the saddle-point.

In the narrow strips, close to the curves of tangent bifurcations, two periodic orbits are present: one stable and one unstable; this illustrates the statement proven in [87] that approximations to expanding Cherry flows possess at most two periodic trajectories. In the inner region only one periodic orbit exists. For $K > 1$ this is the stable one, which remains the unique attractor for the flow in the whole parameter domain. For $K < 1$ the picture is reversed; now the unstable periodic orbit is present everywhere inside the tongue, whereas the existence of the stable one is restricted to the strips outside the curves of homoclinic bifurcations. Inside the inner tongue, the only attractor of the flow is the stable fixed point; in the strips two attracting states coexist.

Chapter 5

Steady viscous flow with fractal power spectrum

5.1 Introduction

To get a feeling of historic affinity between hydromechanics and the theory of dynamical systems one has only to recall several words like "sink", "source" and, last not least, one of the most important ones, the "flow". When one views a steady motion of incompressible fluid as a dynamical system, the flow is really a phase flow, streamlines become phase trajectories, and the time-independent spatial pattern recovers the geometry of the attractor. For this purpose, the Lagrangian description of the fluid motion seems more suited than the Eulerian one. Whereas the latter is bound to the fixed place in the space (where by virtue of steadiness the values of all observables remain time-independent), the former traces the individual "fluid particles" along their paths and can deliver the picture of chaotic motion with its exponential growth of the distance between the initially close particles [88]. The stirring and mixing imposed by chaotic streamline patterns is of importance for geophysics and magnetohydrodynamics; for the numerous examples of Lagrangian chaos in various steady and time-dependent flow patterns see e.g. the monograph [89].

For obvious reasons, the phase space of a chaotic autonomous dynamical system is at least 3-dimensional. Consequently, Lagrangian chaos can be encountered only in fully 3-dimensional steady fluid motions. At the first sight, it may seem that the highest temporal complexity attainable for tracers transported by two-dimensional steady flows is periodicity or at most (in appropriate geometry) quasiperiodicity, with well pronounced correlations and discrete temporal spectra. However, slowing down near the stagnation points generates singularities in the turnover times of individual fluid particles. As we will demonstrate, this can result in the onset of some intermediate phase between order and chaos, where the power spectrum is (singular) continuous, but certain correlations persist over arbitrarily long times (recall that the absolutely continuous spectrum is a signature of chaos, but a dynamical system is mixing if and only if the correlations asymptotically decay [20]). This peculiar type of dynamics is known basically from the mathematical models of systems with incommensurate scales or quantum systems in quasiperiodic potentials (see e.g. [5, 8]), where, unlike

our case, the singular spectra describe the spatial structure; to our knowledge it has never been previously reported in the context of fluid mechanics.

In this Chapter, we report on the class of two-dimensional steady viscous flows generated by time-independent forcing. Increase of the forcing amplitude leads to changes in the topology of streamlines pattern; from the Lagrangian point of view, this marks the transition from the flow with a discrete temporal spectrum to the motion with a fractal one. With the help of the autocorrelation function, we obtain numerical estimates for the correlation dimension of the spectral measure.

5.2 Formulation of hydrodynamical problem

Let the incompressible fluid with density ρ and viscosity ν flow over the 2-torus ($0 \leq x \leq 2\pi$, $0 \leq y \leq 2\pi$) under the action of the time-independent force $\mathbf{F} = (f \sin y, f \sin x, 0)$ (for the experimental realization of spatially periodic forcing in 2-dimensional flows see e.g. [90, 91, 92]). The Navier-Stokes equations governing the fluid motion are

$$\frac{\partial}{\partial t}\mathbf{v} + (\mathbf{v} \cdot \nabla)\mathbf{v} = -\frac{\nabla P}{\rho} + \nu \nabla^2 \mathbf{v} \; + \; \mathbf{F} \tag{5.1}$$

$$\nabla \cdot \mathbf{v} = 0$$

where $\mathbf{v}$ and P are, respectively, the velocity and the pressure. The structure of the forcing term is reminiscent of the Kolmogorov flow [93]. We restrict ourselves to the 2-dimensional formulation; besides, the geometry of the domain implies that not only the forcing, but also the velocity field itself is periodic:

$$\mathbf{v}(x, y) = \mathbf{v}(x + 2\pi, y) = \mathbf{v}(x, y + 2\pi) \tag{5.2}$$

Thus the possible perturbations are confined to the torus size, and the longwave disturbances which are known to be the first to destabilize the Kolmogorov flow [93, 94], are precluded. As a further difference from the Kolmogorov flow we prescribe the fixed non-zero mean flow across the domain in both directions, parameterizing it by the two flow rates α and β, respectively:

$$\begin{aligned} \int_0^{2\pi} v_x dy \Big|_{x=0,2\pi} &= 2\pi\alpha, \\ \int_0^{2\pi} v_y dx \Big|_{y=0,2\pi} &= 2\pi\beta \end{aligned} \tag{5.3}$$

5.3 Flow patterns

Incompressibility of the fluid allows to project out the pressure by introducing the streamfunction $\Psi(x, y)$: $v_x = \partial\Psi/\partial y$, $v_y = -\partial\Psi/\partial x$. The pattern, described by the steady solution

$$\Psi = \alpha y - \beta x + \frac{f \, \sin(x - \phi_1)}{\sqrt{\alpha^2 + \nu^2}} - \frac{f \, \sin(y - \phi_2)}{\sqrt{\beta^2 + \nu^2}} \tag{5.4}$$

$$\phi_1 = -\arctan\frac{\nu}{\alpha},\ \ \phi_2 = -\arctan\frac{\nu}{\beta}$$

of the equations (5.1) satisfying to (5.2) and (5.3), yields the stationary velocity field:

$$\begin{aligned} v_x &= \alpha - \frac{f\ \cos(y-\phi_2)}{\sqrt{\beta^2+\nu^2}} \\ v_y &= \beta - \frac{f\ \cos(x-\phi_1)}{\sqrt{\alpha^2+\nu^2}} \end{aligned} \tag{5.5}$$

In the absence of forcing ($f = 0$) the streamlines are straight and the velocity is everywhere the same; one has the trivial flow on the 2-torus with the rotation number α/β. (Of course, the rotation number equals α/β also in the general case $\Psi = \alpha y - \beta x + \Phi(x, y)$ where $\Phi(x, y)$ is periodic in both arguments and bounded). The increase of the forcing amplitude f distorts the streamlines

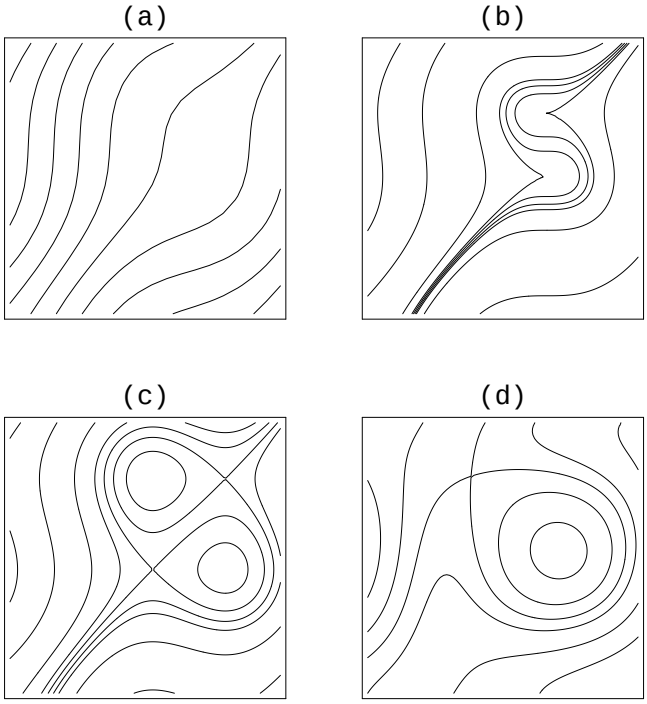

Figure 5.1: Flow patterns for $\alpha = (\sqrt{5}-1)/2$, β=1:
(a) pattern (5.4) for ν=1, $f = \frac{1}{2}f_{cr}$= 0.587785;
(b) pattern (5.4) for ν=1, $f = f_{cr}$;
(c) pattern (5.4) for ν=1, $f = \frac{3}{2}f_{cr}$= 1.7633557;
(d) pattern (5.7).

(Fig.5.1(a)). However, in a range of values of f the Lagrangian dynamics does not alter qualitatively: if α/β is rational, the streamlines are eventually closed; otherwise each particle path is dense in the domain. In both cases the Fourier spectrum of an observable $\xi(t)$ measured along the trajectory of the particle is discrete; the autocorrelation function $C(\tau)$ displays peaks which approach 1 for

the time values corresponding to the multiples of period in the former case and to the denominators of rational approximations to α/β in the latter. This can be seen in Fig.5.2(a); here and below we fix the values ν=1 and the "golden mean" rotation number $(\sqrt{5}-1)/2$.

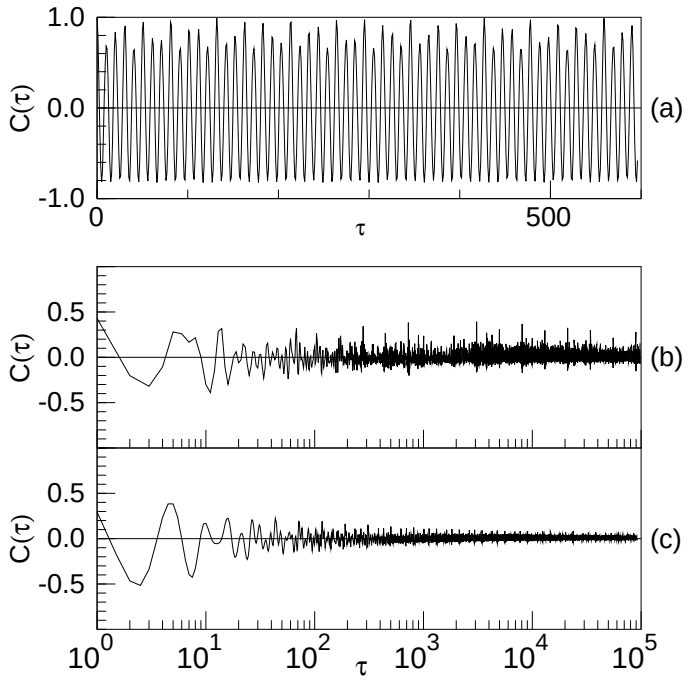

Figure 5.2: Autocorrelation function for "fluid particles" in steady flow patterns:
(a) pattern (5.4); parameter values as in Fig.5.1(a);
(b) pattern (5.4); parameter values as in Fig.5.1(c);
(c) pattern (5.7).

At reaching the threshold value of the forcing amplitude

$$f = f_{cr} = \sqrt{\alpha^2\beta^2 + \nu^2 \max(\alpha^2, \beta^2)} \tag{5.6}$$

two cusps appear at two particular streamlines, with the velocity vanishing at the cusp tips (Fig.5.1(b)). For $f > f_{cr}$ each cusp tip splits into a couple of stagnation points: the elliptic one and the hyperbolic one (the Poincaré index [95, 96] being 1 for the former and -1 for the latter). The pattern of streamlines (5.4) acquires new features: along with the "global" particle paths crossing the whole domain, there appears a "localized" component which is built of two mutually symmetric isolated eddies (Fig.5.1(c)). Each eddy has the elliptic point at its centre and is encircled by one of the separatrices of the respective hyperbolic stagnation point. Inside the eddies the particle paths are obviously closed; respectively, the above statement concerning the density of orbits under irrational values of α/β holds everywhere *outside* the eddies [97].

5.4 Correlation and transport properties

Let us choose a secant which is transversal to the global component of the flow. Due to the Hamiltonian nature of the flow (which is ensured by the incompressibility of the fluid), the Poincaré return mapping which the particle paths induce on this secant, is conjugate to the shift on the circle: $\phi_{i+1} = (\phi_i + 2\pi\,\alpha/\beta) \bmod 2\pi$, both for rational and irrational values of α/β.

Under irrational values of α/β the power spectrum for any orbit of this map is discrete, and the motion is completely correlated, with the appropriate peaks of the autocorrelation function (ACF) tending to 1, like those in Fig.2(a). However, the correlation properties of the flow appear to be remarkably different from those of its own Poincaré mapping. As can be seen from Fig.5.2(b), unlike the subcritical case from Fig.5.2(a), the highest peaks of the ACF do not even reach $\frac{1}{2}$, i.e. the dynamics is far from being completely ordered. The reason for the weakening of correlations lies in the non-uniform slowing down of motion in vicinities of the stagnation points. Take a smooth curve l transversal to the local stable separatrix W_s of a stagnation point. The turnover time τ as a function of a coordinate ζ on l diverges at the point ζ_0 where l and W_s intersect: $\tau(\zeta) \sim -\log|\zeta - \zeta_0|$ (Fig. 5.4). Consider two initially close fluid particles near W_s which move along two streamlines on the same side of W_s and slow down while approaching the stagnation point. The slowing is more pronounced for the particle which lies closer to the separatrix; it stays in the vicinity of the stagnation point longer than its counterpart, and the distance between them grows. The much stronger effect is observed for the two particles lying on the *opposite* sides of W_s, since one of them is doomed to hover in the stagnation region twice (for the first time, on entering it along W_s and for the second, after making a tour around the eddy) and thereby gets a very noticeable lag. As a consequence, the coefficients before the logarithmic terms in $\tau(\zeta)$ to the left and to the right from ζ_0 differ by a factor of 2 [97].

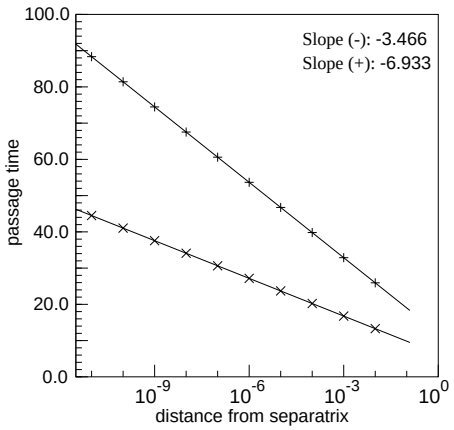

Figure 5.3: Divergence of the turnover time for the pattern from Fig 5.2(c).:
+: passage to the left from stagnation point;
×: passage to the right from stagnation point

Albeit relatively low, the correlations do not entirely decay: at certain time values (which apparently mark the denominators of the best rational approximations to α/β) the ACF displays distinct peaks whose height remains above the certain finite level. Although with growth of time the intervals between these peaks are getting larger and larger (note the logarithmic scale along the time axis), they are well discernible at the largest computationally attainable times which correspond to tens of thousands of revolutions around the torus. The "vague" memory of this kind is characteristic for dynamical systems with singular continuous (fractal) power spectra [49]. The latter deliver a link between systems with the discrete (pure point) spectra and those with absolutely continuous spectra: although the spectrum is continuous, the spectral measure is located on a set of zero Lebesgue measure. For the typical frequency values ω the Fourier sums $S(\omega, L) = L^{-1} \sum_{k=1}^{L} |\xi_k e^{i2\pi k\omega}|^2$ neither grow linearly with the increase of the sample length L, as would be the case for the δ-peaks of the discrete spectrum, nor converge to constant values as in the case of the absolutely continuous spectrum. In this sense, the conventional procedure of computing the power spectrum $S(\omega)$ from time series of progressively growing length provides the more and more "fractalized" approximations to the ultimate singular continuous object. Since the ACF is the Fourier transform of the power spectrum, the fractal properties of the latter can be evaluated with the help of the former. Thus, as discussed above, the integrated squared autocorrelation function $C_{\rm int}(T)$ for a state with purely singular continuous spectrum should decay as $\sim T^{-D_2}$ where D_2 is the correlation dimension of the spectral measure [23]. The plot of $C_{\rm int}(T)$ corresponding to Fig.5.2(b) is presented in Fig.5.4; it provides evidence that the contribution of the discrete spectral component, if present at all, is extremely weak; the slope of this curve yields the estimate for D_2 of the fractal spectral measure: $D_2 = 0.51 \pm 0.02$.

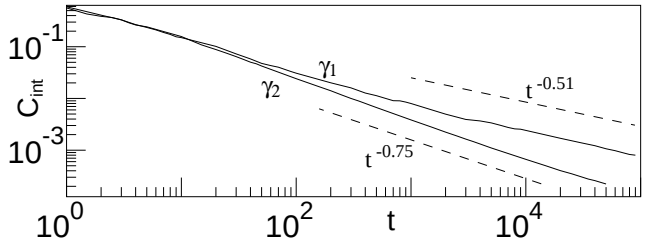

Figure 5.4: Integrated autocorrelation for states from Fig.5.1(c) (curve γ_1) and Fig.5.1(d) (curve γ_2); cf. power laws shown by dashed lines.

The spectral properties of the Hamiltonian flow on a torus without fixed points ($f < f_{cr}$ in our terms) were first addressed by Kolmogorov [34], who showed that the spectrum was discrete for irrational rotation numbers "not too fast" approximated by rationals and conjectured thay it could be continuous otherwise. Further, the possibility of weak mixing for the latter rotation numbers (which constitute a subset of zero measure on the set of all numbers) under certain conditions imposed on the distribution of bounded turnover times was demonstrated by Shklover [70]. In the presence of fixed points the return times are unbounded; as shown by Kochergin [37] in this case the flow does not mix

if the prefactors before the logarithmic terms in the return times are balanced. This is precisely the case for the pattern (5.4) with two symmetric eddies where the sums of prefactors corresponding to the passage to the left and to the right from the stagnation points are obviously equal. Noteworthy, mixing must be present [64] in the threshold case $f = f_{cr}$ when the stagnation points are degenerate and the return times diverge in a power-like way $\tau(\zeta) \sim |\zeta - \zeta_0|^{-1/6}$.

Applying the more elaborate periodic forcing, it is possible to excite a velocity field with a single eddy; a typical flow pattern with a stream function

$$\Psi(x, y) = \alpha y - \beta x + \sin x \cos y - \sin x - \cos y \tag{5.7}$$

is presented in Fig.5.1(d). For this pattern the logarithmic singularities in the return times are not mutually compensated. The respective ACF is plotted in Fig.5.2(c); although one notices many similarities to Fig.5.2(b), the slow but definite decrease of the highest peaks is not to be overseen. The decay of correlations implies mixing; presence of mixing for Hamiltonian flows on a torus with non-balanced logarithmic singularities was shown by Sinai and Khanin [38]. As compared to the case of symmetric eddies, $C_{\rm int}(T)$ decays faster (Fig.5.4); evaluation of the fractal dimension of the spectral measure results in $D_2 = 0.75 \pm 0.01$.

As regards the transport of the non-diffusive scalar tracers in these velocity fields, one may expect something "in between" the ordered motion over the regular pattern and the chaotic advection imposed by Lagrangian turbulence. Due to incompressibility, both Lyapunov characteristic exponents vanish identically; thereby the exponential divergence of close particles is prohibited, and the slower effects should be looked for. Different stages of this slow "diffusion" for the pattern from Fig.5.1(d) are shown in Fig.5.5: the initially compact droplet (10^4 individual particles) spreads over the whole area outside the eddy.

To enable the unbounded drift, we considered the periodic tiling on the plane and computed the value of

$$d_2(t) = \langle\, (x(T+t) - x(t) - t\overline{v_x})^2 \,\rangle \tag{5.8}$$

averaged with respect to the time T along the particle paths, for both the symmetric field (5.4) and asymmetric pattern (5.7); here $\overline{v_x}$ is the mean velocity of the drift in x-direction. In both cases after a short intermediate stage with the timescale of one revolution around the torus, one observes the slow stretching; $d_2(t) \sim t^{2\chi}$ with $\chi \approx 0.07$ for the former and $\chi \approx 0.09$ for the latter.

Summarizing, the discussed class of steady flows is a reasonable candidate for a role of a state with the most complicated Lagrangian dynamics which can be observed in a time-independent 2-dimensional setup. Noteworthy, for these flow patterns the property of having a singular continuous component in the spectrum is generic, unlike the case of dissipative dynamical systems where until now such spectra were reported only for certain marginal situations on the border between order and chaos [49]. Properly rewritten, the equations are governed by 3 dimensionless parameters: the forcing strength and two "Reynolds numbers" characterizing the mean flow in $x-$ and $y-$ directions, respectively. Obviously, each particular state with an irrational rotation number is structurally unstable, but the set of all these states taken together occupies almost the whole parameter space (its complement, corresponding to rational rotation numbers has zero measure). In other words, a randomly chosen point in the

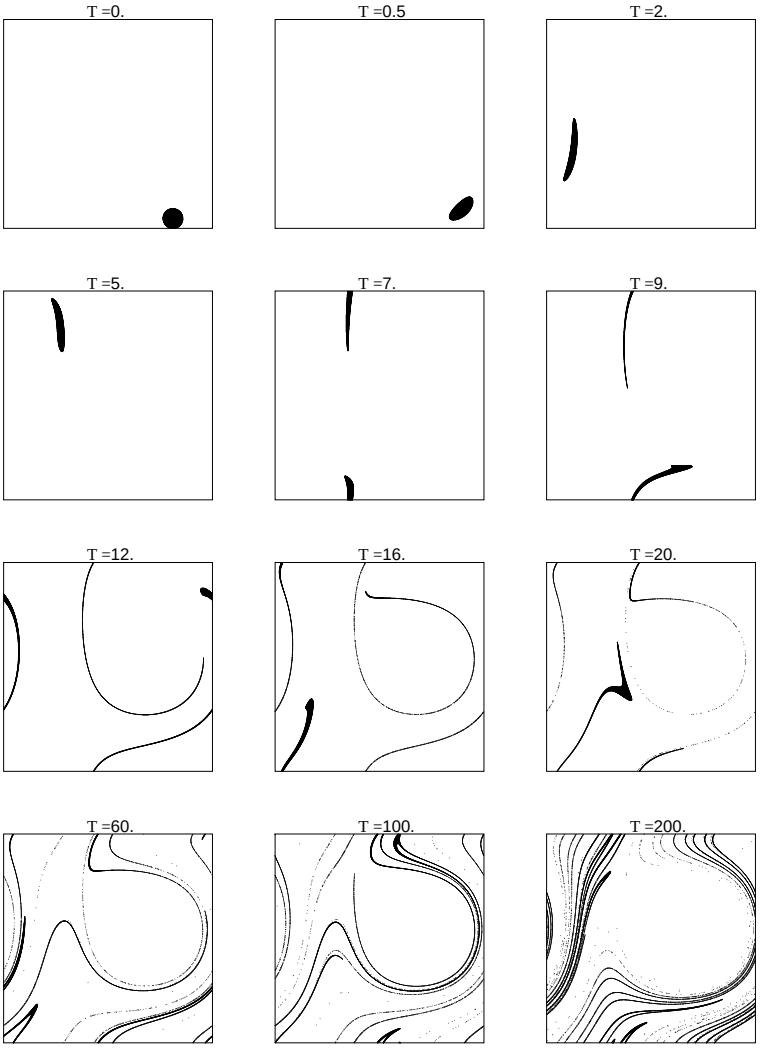

Figure 5.5: Transport of tracer particles by the steady pattern from Fig.5.1(d)

parameter space corresponds with probability 1 to a pattern with irrational rotation number. Thus one is tempted to conjecture that in presence of the imposed mean flow a motion of a passive tracer along the typical two-dimensional steady pattern with isolated eddies possesses the fractal Fourier spectrum.

Chapter 6

Action of noise and randomness on dynamics with fractal Fourier spectra

Problems which were considered in the preceding chapters, were purely deterministic. In almost every physical observation, measurement and experiment the stochastic component is present for obvious reasons: neither it is possible to ensure perfectly constant external conditions during the whole experiment, nor is the precision of the measurement tools unlimited. Our theoretical models also have limited accuracy, and contribution of non-accounted or neglected factors can be often viewed as some weak noise. Singular continuous Fourier spectra are fragile; a weak disturbance can either make them discrete, collecting spectral measure into the countable subset, or (which seems much more plausible) smooth out the singularities, turning them into the absolutely continuous ones. A natural question is: how to resolve inside the noisy datasets the patterns which allow one to conclude that in the deterministic setup the Fourier spectrum should be fractal ? Below we consider several of such situations. We show that the noise which enters the data only during the measurement, leaves intact large parts of the fractal structure of the spectral measure. Further, we take the case when the singular continuous component of the spectrum is generated by geometric mechanism (see Chapter 1), and see how it is affected by the presence of additive noise. Although action of noise leads to the decay of correlations, on the intermediate stage the "noiseless" correlation pattern persists. Duration of this stage is related to the noise intensity by the power law.

Finally, in Sect. 6.3 we introduce randomness into the every core of dynamics: we consider substitution sequences in which each individual symbol is inflated according to one of several randomly chosen substitution rules. It is demonstrated that randomness ensures the power-law decay of correlations; furthermore, if one of the substitution patterns is strongly preferred, the Fourier spectrum retains its multifractal nature.

6.1 Contamination by instrumental noise

In this short section, we treat the situation in which the noise does not affect the nature of the process and interferes only at the observation stage by means of an inaccurate measurement device. Let observable be a superposition of the original signal x_i and δ-correlated noise ξ. In case of additive measurement noise, the autocorrelation function for the variable $y_i = x_i + \xi_i$ is

$$C_y(\tau) = \frac{C_x(\tau)}{1 + \langle \xi_i^2 \rangle / \langle x_i^2 \rangle} \tag{6.1}$$

where $C_x(\tau)$ is the autocorrelation for the variable x_i.

For the noisy "amplitude modulation" $y_i = x_i(1 + \xi_i)$, we get

$$C_y(\tau) = \frac{C_x(\tau)}{1 + \langle \xi_i^2 \rangle} \tag{6.2}$$

In both cases the autocorrelation function of the noisy observable is obtained from the autocorrelation function of the original signal by uniform (τ-independent) contraction. The contraction factor depends on the distribution of noise and is non-zero for the noise with bounded mean square amplitude.

Accordingly, the integrated autocorrelation $C_{\rm int}(\tau)$ of the observable y_i differs from $C_{\rm int}(\tau)$ of x_i by the constant factor, and has the same decay rate. Hence, the correlation dimension D_2 of the spectral measure of y_i coincides with D_2 of the spectral measure of x_i. Furthermore, as shown in Chapter 2, all generalized dimensions D_q with integer $q \geq 2$ for the spectral measure are prescribed by the growth rate of products of values of the autocorrelation function; hence, if the power spectrum of x_i is multifractal, this multifractality in the domain $q \geq 2$ is quantitatively reproduced by the power spectrum of the observed variable y_i. On the other hand, the signal y_i includes the noisy component ξ; since the power spectrum of the latter is absolutely continuous, $D_q = 1$ for $q \leq 1$.

Now consider the instrumental noise on the symbolic level: in the course of observation some of the symbols can be identified wrongly. Let $X = x_1 x_2 x_3 ...$ and $Y = y_1, y_2, y_3 \ldots$ be binary symbolic strings:

$$y_i = \begin{cases} x_i & \text{with probability } 1-p \\ \overline{x_i} & \text{with probability } p \end{cases} \tag{6.3}$$

where $\overline{A}$ denotes a symbol complementary to A. Then: $C_y(\tau) = (1-2p)^2\, C_x(\tau)$ For $p \neq \frac{1}{2}$ the pattern of $C_x(\tau)$ is uniformly vertically compressed. Accordingly, if the spectral measure of original symbolic sequence is fractal, its qualitative and quantitative structure for $q \geq 2$ is recovered in the measured symbolic signal. An example: if each individual symbol in the Thue-Morse sequence is "flipped" with probability $p \neq \frac{1}{2}$, the correlation dimension for the Fourier spectral measure of the symbolic sequence thus obtained, equals the same value $D_2 = 3 - \log(1 + \sqrt{17})/\log 2$ (cf. Eq.(2.10)).

6.2 Interaction between additive noise and geometric mechanism

Now let us allow the noise to interfere into dynamics. This inevitably leads to the onset of absolutely continuous spectral background and ultimate decay of autocorrelation. However, as we will see, in the pattern of autocorrelations it is possible to recover certain "remnants" which allow to conclude that the power spectrum of purely deterministic process is singular continuous. This effect is especially well pronounced in the situations when the fractal spectral component owes to the geometric mechanism. To elucidate this, consider the noisy version of the Eq.(1.6)

$$\begin{aligned} \dot{x} &= \sigma(y-x) + \sigma D y(z-R) + E\zeta(t) \\ \dot{y} &= Rx - y - xz \\ \dot{z} &= xy - bz \end{aligned} \tag{6.4}$$

with the values of the parameters σ, D, R, b corresponding to the accumulation of homoclinic doublings. Here, E is the amplitude of the noisy term, and $\zeta(t)$ is a random variable; for computational reasons it is convenient to take the variable uniformly distributed on the interval $(-1, 1)$.

Recall that in the absence of noise the universal properties of the bifurcation scenario are entirely determined by the saddle index $\nu = |\lambda_2|/\lambda_1$: the ratio of two eigenvalues of the linearization of the flow near the trivial equilibrium $x = y = z = 0$; to enable the sequence of homoclinic doublings, the inequality $\nu > 1$ should hold. To single out the action of the geometric mechanism, we will concentrate on the observables built from the variable x. Reduction of the deterministic flow to one-dimensional mapping on the Poincaré plane yields the discontinuous recursion relation (3.3). At the accumulation point of the bifurcation sequence, the Fourier spectrum of this mapping is singular continuous due to the geometric mechanism. The noisy counterpart of the return mapping (3.3) is

$$\xi_{i+1} = (|\xi_i|^\nu - \mu + E\zeta_i)\,\mathrm{sign}(\xi_i), \tag{6.5}$$

ζ_i being a random function of the discrete argument.

In the deterministic case the attracting sets of Eq.(6.4) and Eq.(6.5) are self-similar and possess scaling properties. Introduction of noise "washes out" the fine structure of the attractors, and the approximate self-similarity can be recovered only beyond a certain level of resolution. The very same process takes place when additive noise acts on dynamical systems at the onset of chaos through period-doublings. It is convenient to characterize the system through the noise sensitivity β which has a transparent meaning: in order to be able to resolve each next level of the fine structure of the attracting set (that is, to see twice as many "bands" in the attractor of the flow, or twice as many "clusters" in the attractor of the map), the noise level should be reduced by a factor β. The value of $\beta = 6.61\ldots$ for the period-doubling scenario was found by direct computations and with the help of the renormalization formalism [98, 99].

Since both the period-doubling scenario and the onset of chaos through the homoclinic doublings can be described within the framework of the same renormalization operator (see e.g. [13, 14, 16, 17]), under the same values of ν the

sensitivity to noise for the discontinuous mappings (6.5) and continuous mappings (3.4) is characterized by the same values of β. Whereas in the discontinuous case all values of ν are equally relevant, for non-degenerate continuous mappings only the quadratic extrema (ν=2) are important. The dependence $\beta(\nu)$ is presented in Fig.6.1; to our knowledge this is the first computation for $\nu \neq 2$. It turns out that the systems with $\nu \approx 2$ are the least sensitive ones; the minimum is reached at $\nu \approx 1.91$.

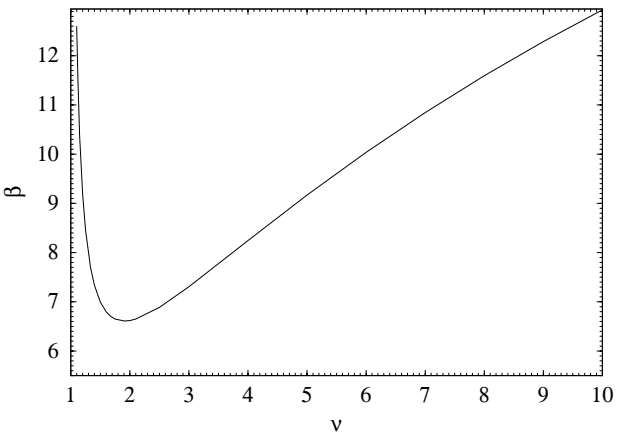

Figure 6.1: Sensitivity to noise as function of the saddle index ν.

The action of noise on the pattern of autocorrelation function of the mapping (6.5) is illustrated in Fig.6.2; the value $\nu = 2$ chosen for this set of computations, corresponds to the sensitivity $\beta = 6.61904\ldots$ [1]. The plot in Fig.6.2a shows the familiar pattern in the absence of noise; the panel (b) presents autocorrelation for the noise with the amplitude $E_0 = 10^{-11}$, and the lower panels (c), (d), (e), (f) and (g) correspond to the intensities of noise βE_0, $\beta^2 E_0$, $\beta^3 E_0$, $\beta^4 E_0$ and βE_0, respectively.

From these plots it can be seen that the original log-periodic pattern of autocorrelation persists almost intact until a certain threshold value of time $t_{\rm n}$; beyond t_n autocorrelation rapidly decays. We observe in plots (b)-(g) that each increase of the noise intensity by the factor β is accompanied by the shift of the right boundary of the correlation pattern "one big peak to the left": in other words, it decreases $t_{\rm n}$ by factor 2. Accordingly, the length of time interval during which the autocorrelations largely behave in the same way as in the absence of noise, is related to the noise intensity by means of the power law:

$$t_{\rm n} \approx CE^{-\kappa}, \quad \kappa \equiv \frac{\log \beta(\nu)}{\log 2} \tag{6.6}$$

This is also well corroborated by computations for other values of ν.

[1] Strictly speaking, the value of sensitivity depends on the particular kind of noise [100]; the procedure employed for the calculations in Fig. 6.1 assumes that the noise is Gaussian. However, from our numerical results on the scaling of autocorrelation functions, it appears that the values for uniformly distributed random variables are close to the respective values for Gaussian noise.

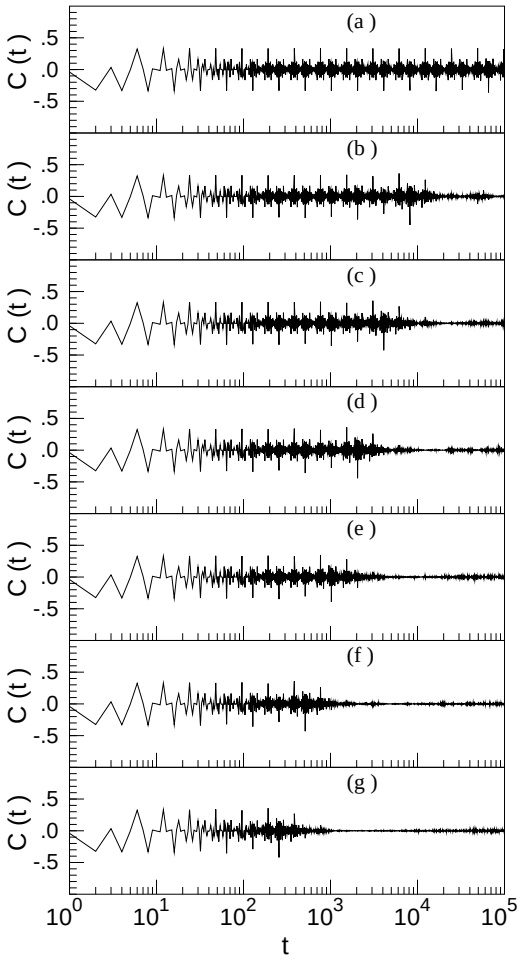

Figure 6.2: Autocorrelation for the mapping (6.5) with ν=2:
(a) $E = 0$; (b) $E = E_0 = 10^{-11}$; (c) $E = \beta E_0 = 6.61904 \times 10^{-11}$;
(d) $E = \beta^2 E_0 = 4.38117 \times 10^{-10}$; (e) $E = \beta^3 E_0 = 2.89991 \times 10^{-9}$;
(f) $E = \beta^4 E_0 = 1.91946 \times 10^{-8}$; (g) $E = \beta^5 E_0 = 1.27050 \times 10^{-7}$.

The similar picture is found in case of continuous-time dynamics. Results obtained by integration of Eq.(6.4) under different noise intensities are presented in Fig.6.3. Again we observe the persistence of the pattern of the autocorrelation function within a certain interval of time, whose duration is interrelated with the noise intensity by means of the power law (6.6). This allows us to expect that the same scaling of the length $t_{\rm n}$ of "singular continuous" autocorrelation pattern can be measured in sufficiently accurate real physical experiments by introducing the controlled amount of noise.

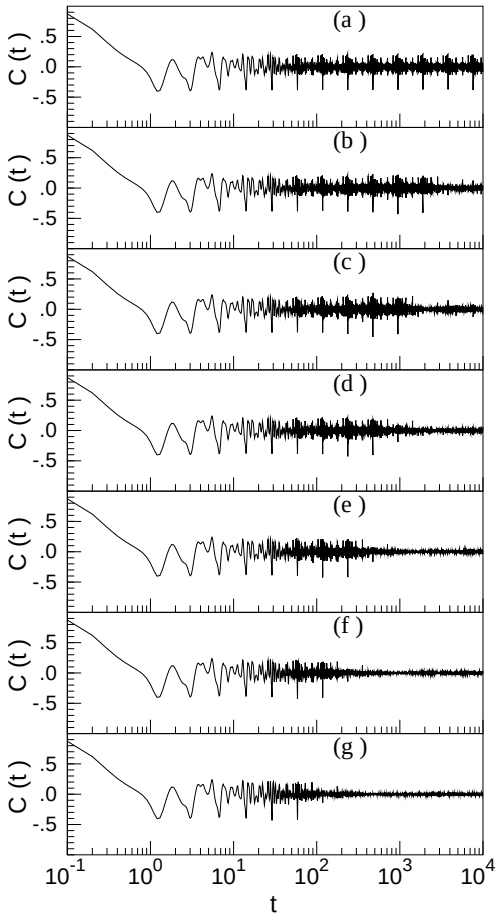

Figure 6.3: Autocorrelation for the equations (6.4) with ν=2:
(a) $E = 0$; (b) $E = E_0 = 10^{-6}$; (c) $E = \beta E_0 = 6.61904 \times 10^{-6}$;
(d) $E = \beta^2 E_0 = 4.38117 \times 10^{-5}$; (e) $E = \beta^3 E_0 = 2.89991 \times 10^{-4}$;
(f) $E = \beta^4 E_0 = 1.91946 \times 10^{-3}$; (g) $E = \beta^5 E_0 = 1.27050 \times 10^{-2}$.

6.3 Multifractal Fourier spectra and power-law decay of correlations in random substitution sequences

Discrete patterns (vortices, crystals, spins, ..., nucleotides, ...) occur on the continuous background in almost every natural system. This makes such systems amenable to discretized description, the ultimate step of which is the reduction to a finite set of symbols, without restricting the generality [101, 102]. For example, in nonlinear dynamics a common practice is to define the partition of the state space, assign labels to partition cells, and mimic continuous evoilution by a sequence of letters. In many important cases the resulting symbolic code is invariant under replacement of certain blocks of several letters by one letter. Such self-similar codes are recovered e.g. at the onset of chaos through the period-doubling scenario[61, 103], quasiperiodicity [84] or homoclinic bifur-

cations [15]. In a wider context, self-similar symbolic sequences stand behind many phenomena in physics of critical states. Often exact similarity is marred by imperfections caused by various reasons, from noise to influence of the boundaries.

Inversely, symbolic codes are unfolded from a single initial symbol by repeated substitutions (inflations) which replace each letter by the prescribed block. Viewed as dynamical systems, deterministic substitution sequences have long been an object of intensive studies [21, 101]. By analyzing the distributions of different combinations of symbols in these sequences, the measure of their complexity can be characterized in terms of word frequencies, entropies and transinformation [102]. On assigning numerical values to letters, a symbolic string turns into a time series and its metric characteristics: Fourier spectra, correlation functions, etc. can be computed. For periodic and quasiperiodic sequences the power spectrum is a set of discrete δ-peaks; spectra of chaotic sequences are absolutely continuous with respect to the Lebesgue measure. One of the classical substitution sequences, the Thue-Morse code [18, 19] produced by the action of a substitution $\left\{ {A \to AB \atop B \to BA} \right.$ on a two-letter alphabet, is neither periodic nor chaotic; accordingly, its power spectrum is neither discrete nor absolutely continuous, but was proved to be singular continuous [40]: the spectral measure is supported by the fractal set.

Influence of noise results in imperfections in the structure of a symbolic string. Action of different kinds of noise on entropic characteristics of symbolic sequences was considered in [104, 105]. In this Chapter, we introduce randomness into the very core of the substitution process: for each symbol, the substitution pattern is chosen among several candidates. We show how this leads to the power-law decay of correlations; for a class of such sequences, the Fourier spectrum is a multifractal mixture of absolutely continuous and singular parts.

We restrict ourselves to substitutions in which the alphabet is binary, all letters are updated simultaneously, and each one is replaced by two letters, so that one global update doubles the length of the symbolic string. The process starts with one letter and creates the infinite sequence $\{\xi_j\}$. In the biological context, this can be viewed as a toy model of linear growth: a cell divides into two which divide again and so on. If there are only two kinds of cells, the process is a sequence of binary substitutions. Without mutations, all cells obey the same "built-in" division rule, e.g. a duplication $A \to AA$. With random mutations allowed, some of the divisions follow different rules, introducing disorder into the growing pattern.

To conclude on the nature of spectral measure, we use the same tools as in purely deterministic dynamical systems from the preceding chapters: the autocorrelation function $C(\tau)$ and the integrated autocorrelation $C_{\rm int}(t)$.

6.3.1 Random mixture of two substitution rules

We start with two inflation rules which randomly alternate. At each individual place the replacing pattern is chosen among two candidates: with probability p the symbol is duplicated and with probability 1–p the complementary symbol

is written after it:

$$\begin{array}{l} A \to \left\{ \begin{array}{ll} AA & \text{with probability } p \\ AB & \text{with probability } 1-p \end{array} \right. \\ B \to \left\{ \begin{array}{ll} BB & \text{with probability } p \\ BA & \text{with probability } 1-p \end{array} \right. \end{array} \tag{6.7}$$

The rule for each letter is chosen independently of the choices made elsewhere. Deterministic case p=0 yields the Thue-Morse code; its autocorrelation has a typical pattern of a system with purely singular power spectra (Fig.6.4a), built around a log-periodic lattice of moderate peaks $C(3 \times 2^n) = -C(2^n) = 1/3$. The trivial opposite limit p=1 results in repetition of one symbol. For $p \neq 0{,}1$ the statistical treatment is required; statements below refer to the expectations of the corresponding values, and assume averaging over ensembles of infinite symbolic strings.

Assigning numerical values to symbols (i.e. $A{=}{-}B\,{=}1$) and demanding invariance of the averaged products $\langle \xi_j \xi_{j+\tau} \rangle$ with respect to inflation (6.7), we obtain two recurrent relations for the autocorrelation function:

$$\begin{array}{lcl} C(2\tau) & = & k_{\rm e} C(\tau) \\ C(2\tau+1) & = & k_{\rm o}\left(C(\tau)+C(\tau+1)\right), \end{array} \tag{6.8}$$

$$k_{\rm e} = 1 - 2p + 2p^2,\ k_{\rm o} = p - \frac{1}{2}$$

which, together with the "initial condition"

$$C(1) = (2p-1)/(3+4p-4p^2),$$

determine $C(\tau)$ for any τ. For $p \neq 0{,}1$ the prefactor $k_{\rm e}$ in the first of Eqs.(6.8) lies between 0 and 1; hence, autocorrelation decays. The highest peaks obey the power law: $|C(\tau)| \sim \tau^{\kappa}$ with $\kappa = \log(1-2p+2p^2)/\log 2$. For $p < 1/2$ the second prefactor $k_{\rm o}$ is negative and the decay is oscillatory (Fig.6.4b); for $p > 1/2$ the values of $C(\tau)$ stay positive (Fig.6.4c).

The relations (6.8) allow us to determine the decay rate of the integrated autocorrelation $C_{\rm int}$. The evolution of the sums

$$U_n \equiv \sum_{\tau=2^n}^{2^{n+1}-1} C^2(\tau),\ W_n \equiv \sum_{\tau=2^n}^{2^{n+1}-1} C(\tau)C(\tau+1) \tag{6.9}$$

is governed by recurrent relations

$$\begin{array}{lcl} U_{n+1} & = & (k_{\rm e}^2 + 2k_{\rm o}^2)U_n + 2k_{\rm o}^2 W_n + k_{\rm o}^2 \zeta_n \\ W_{n+1} & = & 2k_{\rm e}k_{\rm o}(U_n + W_n) + k_{\rm e}k_{\rm o}\zeta_n \end{array} \tag{6.10}$$

where $\zeta_n = (C(1))^2(k_{\rm e}^2 - 1)k_{\rm e}^{2n}$. If U_n and W_n as functions of n do not decrease, the terms with ζ_n in the equations (6.10) can be neglected, and for large values of n both sums (6.9) are proportional to λ^n where λ is the larger root of the quadratic equation:

$$\begin{array}{ll} \lambda^2 & -(4p^4 - 4p^3 + 4p^2 - 2p + \frac{1}{2})\lambda \\ & -(1-2p)(2p^2 - 2p + 1)^3 = 0. \end{array} \tag{6.11}$$

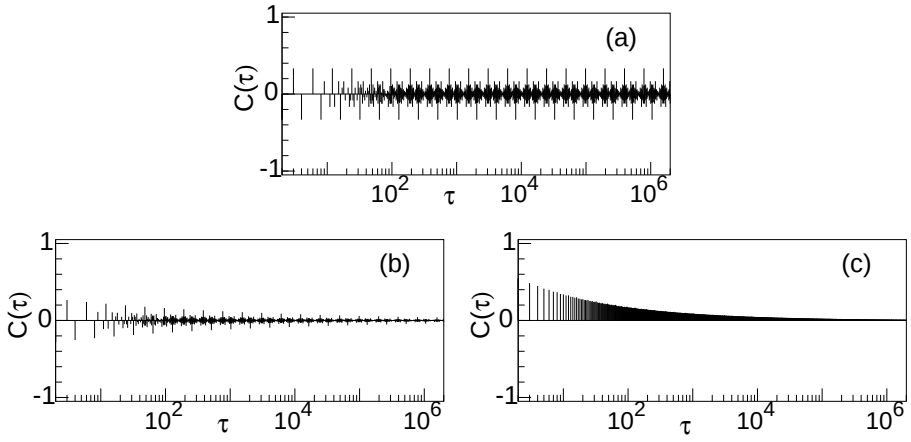

Figure 6.4: Autocorrelation function for the substitution (6.7).
(a): p=0 (Thue-Morse sequence); (b) p=0.05; (c): p=0.9.

Accordingly, the decay of the integrated autocorrelation $C_{\rm int}(t)$ is described by the power law with the exponent $\max(\log\lambda/\log 2-1,-1)$. This yields the correlation dimension of the spectral measure:

$$D_2 = \min(1,\ 1-\frac{\log\lambda}{\log 2}\ ) \tag{6.12}$$

Since for $p < 0.06123$ and for $p >0.84079$ $D_2(p)$ is smaller than 1, the spectral measure in these intervals of p is fractal or, at least, includes a singular component (Fig.6.5).

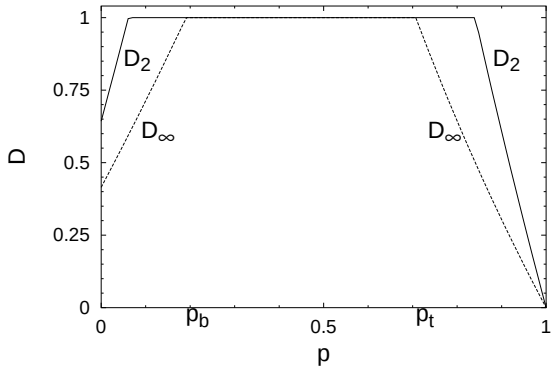

Figure 6.5: Dependence of fractal dimensions of the spectral measure on probability p.

To get a better idea of the distribution of spectral measure as a function of p, consider dynamics of finite-length Fourier sums $S_n(\omega)=2^{-n}|\sum_{k=1}^{2^n}\xi_k\exp(\mathrm{i}2\pi\omega k)|^2$ under the increase of n. Due to periodicity, analysis can be restricted to the interval $0\leq\omega<1$. For the absolutely continuous spectrum, $S_{n\to\infty}(\omega)$ converges to a bounded curve. Pointwise divergence of $S_n(\omega)$ indicates presence of singularities in the spectral measure. For the pure-point measure, $S_{n\to\infty}(\omega)$ vanishes

everywhere outside the countable set of points; in these points which correspond to δ-peaks in the spectrum, S_n diverges, and the ratio S_{n+1}/S_n tends to 2.

For the substitution (6.7), the Fourier sums are interrelated by the functional equation

$$S_{n+1}(\omega) \;=\; 2p-2p^2 \;+\; \left(1-2p+2p^2-(1-2p)\cos 2\pi\omega\right) S_n(2\omega) \qquad (6.13)$$

with the initial condition S_0=1.

At p=0 this gives $S_{n+1}(\omega) = (1-\cos 2\pi\omega)\; S_n(2\omega)$. The sum $S_n(\omega)$ vanishes at $\omega = m/2^{n-1}$, $m = 0, 1, 2, \ldots$. The values of ω with the highest local growth rate $\gamma_{\max} = S_{n+1}(\omega)/S_n(\omega)$ lie at $\omega = m/(3\times 2^{n-1}), m = 1, \ldots, 3\times 2^{n-1}-1$; since $\gamma_{\max} = 1-\cos 2\pi/3 = 3/2 < 2$, the highest peaks grow slower than the δ-peaks would do. Numerically, the multifractal spectral measure of the Thue-Morse sequence was analyzed in [50]; exact expressions for the generalized dimensions were derived in [77].

Under $p \neq 0, 1$ the factor before $S_n(2\omega)$ in Eq.(6.13) is positive. Hence, $S_{n+1}(\omega) > 2p-2p^2 > 0$, and the absolutely continuous part is present in the power spectrum.

The curve $S_n(\omega)$, typical for small p (here, p=0.1, n=11) is plotted in Fig.6.6a. For $p < 1/2$, the rate $\gamma_{\max}$ equals $2p^2-3p+3/2$ and is attained at the same values of ω as for the Thue-Morse code; the highest peak for all n lies at $\omega = 1/3$. Presence of the dense set of singularities is guaranteed if $\gamma_{\max} > 1$; absence of discrete component is ensured by $\gamma_{\max} < 2$. The latter inequality holds for all p, and from the former it follows that for $p < p_b = (3-\sqrt{5})/2 = 0.1909\ldots$ the power spectrum is a mixture of absolutely continuous and singular continuous components. To the support of the latter belongs the disjoint continuum of ω-values which, written in the binary notation, contain the infinite number of sufficiently long segments ...101010101....

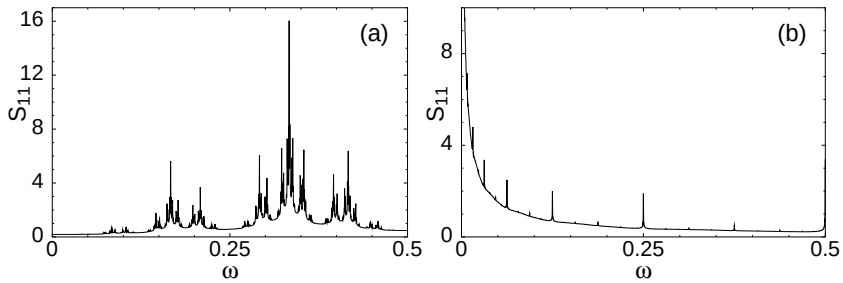

Figure 6.6: Finite-length approximations $S_n(\omega)$ to spectral curves.
(a): p=0.1, n=11; (b): p=0.9, n=11.

When p exceeds 1/2, the picture is different (Fig.6.6b). Now $\gamma_{\max}$ equals $2p^2$ and is reached at $\omega = m/2^{n-1}, m = 0, 1, 2, \ldots$. For $p > p_t = \sqrt{2}/2 = 0.707\ldots$, the inequalities $1 < \gamma_{\max} < 2$ are fulfilled, and the power spectrum includes a dense set of singularities; the highest peak for each n lies at $\omega = 0$. The background of the spectrum is formed by the continuous component which obeys a power law: for the non-singular small values of ω,

$$S_{n\to\infty}(\omega) \sim \omega^{-1-2\log p/\log 2} \qquad (6.14)$$

Accordingly, for $p_t < p < 1$ the spectrum is again a mixture of absolutely continuous and singular components. The fractal support of the latter includes the continuum of ω-values whose binary expansions contain infinitely many segments ...0000....

For the values of p between p_b and p_t, the power spectrum contains no singularities; it is absolutely continuous. In the simplest case of $p = 1/2$ when substitutions in (6.7) have equal probabilities, Eq.(6.13) results in $S_n(\omega) = 1$: the spectral measure is uniform. According to Eq.(6.8), the autocorrelation $C(\tau)$ in this case vanishes identically.

For $0 < p < p_b$ and for $p_t < p < 1$ the distribution of the spectral measure is multifractal. The formalism of multifractal analysis [106, 107] has been adapted for Fourier spectra in [50, 49]: the range of values of ω between 0 and 1 is partitioned into the boxes of the size ε, and the partition function for a real q is introduced as $U(q, \varepsilon) = \sum_{i=1}^{1/\varepsilon} \rho_i^q$ where ρ_i is the probability to locate the measure in the i-th box. Since spectral measure itself is not explicitly available, one can use as approximations the finite-length sums $S_n(\omega)$; as shown in [77], the refinement of the partition should be accompanied by the increase of n. Assuming the scaling $U(q, \varepsilon) \sim \varepsilon^{\tau(q)}$, we arrive in the usual way at the definition of generalized dimensions D_q: $D_q = (q-1)^{-1}\tau(q)$. Due to the presence of continuous background, $D_q = 1$ for $q \leq 1$. For large positive q the partition function is dominated by the contribution of boxes in which $S_n(\omega)$ grows with the rate $\gamma_{\max}$; accordingly,

$$D_{q\to\infty} \cong \frac{q}{q-1}\left(1 - \frac{\log \gamma_{\max}}{\log 2}\right)$$

For $0 < p < p_b$, as shown above, $\gamma_{\max} = 2p^2 - 3p + 3/2$; hence

$$D_{q\to\infty} \to D_\infty = 1 - \frac{\log(2p^2 - 3p + 3/2)}{\log 2}$$

In the interval $p_t < p < 1$, the rate $\gamma_{\max}$ equals $2p^2$; therefore, $D_\infty = -2\log p/\log 2$. Numerically found dependencies D_q for several values of p are plotted in Fig.6.7a,b.

The dependence $\tau(q)$ yields the spectrum of singularities $f(\alpha)$ [107]: $\alpha = d\tau/dq$ and $f(\alpha) = q\alpha - \tau$. Presence of continuous component makes the distribution, in terms of [50], "half a multifractal": the curve $f(\alpha)$ has only an ascending branch (Fig.6.7c,d). For each p, the values of α lie in the range $(D_\infty, 1)$ (in the exceptional case of purely singular-continuous spectrum at $p = 0$, the right border reaches $\alpha = 2$ [50]). With increase of p from zero, this range monotonically decreases and at $p = p_b$ shrinks to a point; up from p_t the range of α regains the finite width.

6.3.2 Four alternating substitution rules

Now consider random choice among all possible two-letter words. Fix non-negative p_1, p_2, and p_3 so that $p_4 \equiv 1 - p_1 - p_2 - p_3 \geq 0$, and inflate each symbol

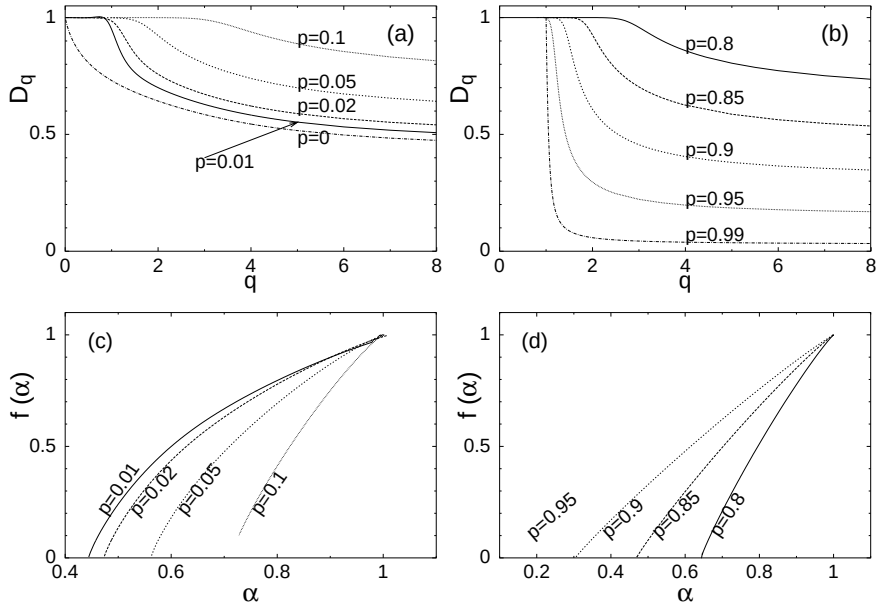

Figure 6.7: Multifractal characteristics of the spectral measure of substitution (6.7). (a),(b): generalized fractal dimensions; (c),(d): spectra of singularities.

according to:

$$
\begin{aligned}
A \rightarrow & \begin{cases} AA & \text{with probability } p_1 \\ AB & \text{with probability } p_2 \\ BA & \text{with probability } p_3 \\ BB & \text{with probability } p_4 \end{cases} \\
B \rightarrow & \begin{cases} BB & \text{with probability } p_1 \\ BA & \text{with probability } p_2 \\ AB & \text{with probability } p_3 \\ AA & \text{with probability } p_4 \end{cases}
\end{aligned}
\tag{6.15}
$$

The values of the autocorrelation function $C(\tau)$ for the substitution (6.15) are related through the recurrence

$$
\begin{aligned}
C(2\tau) &= K_{\mathrm{e}} C(\tau), \\
C(2\tau+1) &= K_{\mathrm{o}} \left(C(\tau) + C(\tau+1) \right)
\end{aligned}
\tag{6.16}
$$

with $K_{\mathrm{e}}{=}(p_1-p_4)^2+(p_2-p_3)^2$ and $2K_{\mathrm{o}}{=}(p_1-p_4)^2-(p_2-p_3)^2$. The starting point of this recurrence is given by

$$
C(1) = \frac{p_1 - p_2 - p_3 + p_4}{2(1-K_{\mathrm{o}})} \tag{6.17}
$$

This, again, ensures the power-law decay of autocorrelation: $|C(\tau)| \sim \tau^{\log K_{\mathrm{e}}/\log 2}$. The correlation dimension of the spectral measure is given by $D_2 = \min(1, 1 - \log\lambda/\log 2)$ where λ is the larger root of

$$
\lambda^2 - (2K_{\mathrm{o}}^2 + 2K_{\mathrm{e}}K_{\mathrm{o}} + K_{\mathrm{e}}^2)\lambda + 2K_{\mathrm{e}}^3 K_{\mathrm{o}} = 0 \tag{6.18}
$$

In the case of "rare mutations" when one of the probabilities p_i is sufficiently close to 1, and the other three are small, the inequality $\lambda > 1$ (which, in turn, implies $D_2 < 1$) holds. Accordingly, the presence of the singular continuous component is typical for such situations.

Multifractal properties of the spectral measure can be recovered from finite-length sums $S_n(\omega)$ which, for the substitution (6.15), obey the recurrent relation

$$\begin{aligned} S_{n+1}(\omega) = \quad & 1 - K_\mathrm{e} + (K_\mathrm{e} + 2K_\mathrm{o}\cos 2\pi\omega)S_n(2\omega) \\ & +(p_1 + p_4 - p_2 - p_3 - 2K_\mathrm{o})\cos 2\pi\omega \end{aligned} \tag{6.19}$$

If at least two of the probabilities p_i do not vanish, the spectral background is everywhere (except, perhaps, at $\omega = 0,\, 1/2$) bounded away from zero. Hence, the absolutely continuous component is present, and the power spectrum is either purely absolutely continuous or mixed.

The detailed analysis of the substitution (6.15) and the recurrent relation (6.19) will be presented elsewhere. The case $p_3 = p_4 = 0$ has been considered above. Here we briefly comment on two other combinations of two substitutions. Under $p_1 = p_4 = 0$, the substitution rules which alternate, are the Thue-Morse rule, and the "reordered Thue-Morse". For each of them, taken alone, the Fourier spectrum is purely singular continuous. As soon as they are mixed together, the absolutely continuous component appears. In order for the spectrum to be multifractal, probabilities of the substitutions should strongly differ. If $p \equiv \min(p_2, p_3)$ exceeds 0.03, the dimension D_2 of the spectral measure equals 1. For $p > 1/2 - \sqrt{6}/6$, the dimension D_∞ turns into 1, and the power spectrum is absolutely continuous.

In the opposite case $p_2 = p_3 = 0$ each of two competing rules produces the periodic symbolic sequence. For $p \equiv \min(p_1, p_4) < p_b = 1/2 - \sqrt{2}/2$, spectral measure has a singularity at $\omega = 0$; at small ω the power law holds:

$$S_{n\to\infty}(\omega) \sim \omega^{-1-2\log(1-2p)/\log 2} \tag{6.20}$$

Above p_b the singularity is absent; the spectrum is absolutely continuous.

Summarizing, random combination of binary substitutions always leads to the power-law decay of autocorrelation and is, in many cases, a cause of singularities in the spectral measure.

6.3.3 Implications for observational data

The power-law correlation decay ("long range correlations") is abundant in natural processes, from physical systems near critical points [108] to human walking [109] and standing [110], atmospheric variability [111, 112] and sequences of nucleotides in the DNA [113, 114, 115, 116, 117]. A decade ago W. Li recognized that many properties of such processes were reproduced by randomly alternating substitutions; in his "expansion-modification system", the choice was made between a duplication and a mutation to a complementary symbol [118, 119]. Compared to the substitution (6.15), such systems are reminiscent of the case p_2=p_3=0: when mutations are rare, the power spectrum decays as $1/\omega^\alpha$ with $\alpha \sim 1$.

Processes with long-range correlations are often explained in terms of ran-

dom walks [108, 109, 110, 111, 112, 113], by means of squared fluctuation

$$F^2(l) = \langle (\sum_{j+1}^{j+l} \xi_i)^2 \rangle$$

averaged over the position j. In the scaling dependency $F^2(l) \sim l^{2\alpha}$, the value $\alpha = 1/2$ is interpreted as an attribute of a genuine non-correlated random walk, whereas $\alpha > 1/2$ indicates the presence of correlations. Calculation for Eq.(6.15) yields

$$2\alpha = \max\left(\mathrm{sign}(p_1 + p_4),\, 2 + 2\frac{\log|p_1 - p_4|}{\log 2}\right) \tag{6.21}$$

Thereby, the criterion does not distinguish substitutions with $|p_1 - p_4| < \sqrt{2}/2$ from random walk; in particular, all sequences with a big proportion of Thue-Morse-like inflations (and slow correlation decay) look from this point of view as completely disordered.

Alternatively, in dynamics the degree of irregularity is usually expressed in terms of ergodic characteristics like mixing, which, in their turn, are related to spectral properties [101]. Analysis of observables built on 2-letter words of inflations (6.7) and (6.15) shows that corresponding dynamical systems are neither mixing nor even weakly mixing. This means that, in spite of the continuous component in the Fourier spectrum, the actual level of disorder in the substitution sequences is relatively low.

Simple random substitution rules allow us to arrive at explicit scaling laws and exact values of fractal dimensions. Corresponding characteristics of more realistic models can be reasonably close to these laws and values. In this respect, it can be noticed that the strongly pronounced peak exactly at the frequency $\omega = 1/3$ in Fig.6.6a (as well, as in power spectra of the substitution (6.15) with dominating values of p_2 or p_3) is reminiscent of the "period-three" pattern recovered in the structure of correlation functions and mutual information of the DNA [120, 121].

As seen from our analysis, power-law decay of correlations does not necessarily imply that the spectral measure is multifractal; however, in situations when one of the substitution patterns is strongly preferred, presence of fractal component is quite probable. To our knowledge, decomposition of spectral measure in processes with power-law correlations did not yet receive the proper attention. Presented results allow to expect the fingerprints of fractal power spectra in many of such processes.

Conclusions

1. It is demonstrated that singular continuous Fourier spectra can be met in dynamical systems of different nature: symbolic sequences, continuous and discontinuous one-dimensional mappings, time-continuous flows governed by ordinary differential equations, and in systems described by partial differential equations.

2. Two mechanisms can be responsible for the onset of fractal Fourier spectra:

   (a) the "geometrical" mechanism which owes to the mirror symmetry of the attracting set: passage through each of the halves of the attractor is encoded by a symbol, and the binary sequence produced by symbolic encoding of the orbit can have singular continuous spectrum;

   (b) the "dynamical" mechanism which is related to presence of saddle points in the attracting sets of time-continuous flows: near the stable manifold of such points the return times onto the Poincaré plane diverge logarithmically or following the power law.

3. Continuous dynamical systems with saddle states of equilibrium possess fractal power spectra at the point of transition from order to chaos through different sequences of homoclinic bifurcations. For the continuum of scenarios of such transition, the dynamical mechanism is in action; additional symmetries in the system can enable also the action of the geometrical mechanism.

4. Spectral properties of continuous dynamical systems with unbounded return times are not necessarily correctly reproduced by spectral properties of their Poincaré mappings: if the power spectra of the flows are singular continuous, the power spectra of the corresponding mappings can be purely discrete. Thereby the dynamics of the mapping can be simpler than the dynamics of the underlying continuous flows.

5. For a class of substitution sequences, estimation of dimensions of their multifractal spectral measure is reduced to the computation of the largest eigenvalue of the corresponding matrix.

6. Generalized fractal dimensions of spectral measure with positive integer indices can be evaluated from the growth rates of the corresponding products of autocorrelations.

7. Discrepancy between the spectral properties of continuous flows with unbounded return times and spectral properties of symbolic sequences generated by the partition of the phase space is removed, if the symbols in

the sequence are endowed with "residence times", proportional to the durations of stay of the system in the cells of the partition. In defining these residence times, taking into account the exponential or superexponential scaling properties of the attractor can be helpful.

8. Continuous dynamical systems on two-dimensional tori with points of equilibrium and irrational rotation numbers – so-called Cherry flows – possess singular continuous component in the Fourier spectra of generic observables. This property is not shared by symbolic sequences obtained from one-dimensional Poincaré mappings of such flows; however, the introduction of residence times for individual symbols allows to reconstruct symbolic dynamics with qualitatively correct spectral characteristics.

9. For observables, built from the motion of a Lagrangian tracer particle in steady plane flows of viscous incompressible fluid over domains with doubly periodic boundary conditions, power spectra can be multifractal. In particular, in flows past the lattice of stationary eddies excited by spatially periodic forcing, presence of singular continuous spectral component is typical, and autocorrelation function decays in spite of the non-chaotic nature of the motion.

10. Binary substitution sequences built with the help of random choice of a substitution pattern among several candidates, display, in general, power-law decay of correlations. If one of the substitution patterns is strongly preferred ("weak mutations"), the Fourier spectra of such sequences are multifractal.

Bibliography

[1] P. Bergé, Y. Pomeau, C. Vidal, *Order within chaos* (J. Whiley, New York, 1986).

[2] H. G. Schuster, *Deterministic Chaos, An Introduction* (VCH – Verlag, Weinheim, 1988).

[3] A. J. Lichtenberg, M. A. Lieberman, *Regular and Chaotic Dynamics* (Springer, New York, 1992).

[4] J. Argyris, G. Faust, M. Haase, *An Exploration of Chaos* (North-Holland, Amsterdam, 1994).

[5] S. Aubry, C. Godrèche, J. M. Luck, A structure intermediate between quasi-periodic and random, Europhys. Lett. **4**, 639–643 (1987).

[6] C. Godrèche, J.M. Luck, F. Vallet, Quasiperiodicity and types of order: a study in one dimension, J. Phys. A: Math.Gen. **20**, 4483-4499 (1987).

[7] S. Aubry, C. Godrèche, J. M. Luck, Scaling properties of a structure intermediate between quasiperiodic and random, J. Stat. Phys. **51**, 1033–1075 (1988).

[8] R. Artuso G. Casati, F. Borgonovi, L. Rebuzzini, I. Guarneri, Fractal and dynamical properties of the kicked Harper model, Int. J. of Modern Physics B **8**, 207–235 (1994).

[9] J. M. Luck, H. Orland, U. Smilansky, On the response of a two-level quantum system to a class of time-dependent quasi-periodic perturbations, J. Stat. Phys. **53**, 551–564 (1988).

[10] U. Feudel, A. S. Pikovsky, M. A. Zaks, Correlation properties of quasiperiodically forced two-level system, Phys. Rev. E **51**, 1762–1769 (1994).

[11] A. Pikovsky, U. Feudel, Correlations and spectra of strange nonchaotic attractors, J. Phys. A: Math.,Gen. **27**, 5209–5219 (1994).

[12] U. Feudel, A. Pikovsky, A. Politi, Renormalization of correlations and spectra of a strange nonchaotic attractor, J. Phys. A: Math.,Gen. **29**, 5297–5311 (1996).

[13] D. V. Lyubimov, M. A. Zaks, Two mechanisms of the transition to chaos in finite-dimensional models of convection, Physica D **9**, 52–64 (1983).

[14] A. Arneodo, P. Coullet, C. Tresser, A possible new mechanism for the onset of turbulence, Phys. Lett. A **81**, 197–201 (1981).

[15] J.-M. Gambaudo, I. Procaccia, S. Thomae, C. Tresser, New universal scenarios for the onset of chaos in Lorenz-type flows, Phys. Rev. Lett **57**, 925–928 (1986).

[16] I. Procaccia, S. Thomae, C. Tresser, First return maps as a unified renormalization scheme for dynamical systems, Phys. Rev. A **35**, 1884–2001 (1987).

[17] D. V. Lyubimov, A. S. Pikovsky, M. A. Zaks, Universal scenarios of transition to chaos via homoclinic bifurcations, Mathematical Physics Review, vol.**8**, edited by S. P. Novikov (Gordon and Breach, Chur, 1989), 221–292.

[18] A. Thue, Über unendliche Zeichenreihen, Norske vid. Selsk. Skr. I. Mat. Nat. Kl. Christiania **7**, 1–22 (1906).

[19] M. Morse, Recurrent geodesics on a surface of negative curvature, Trans. A. M. S. **22**, 84–100 (1921).

[20] I. P. Cornfeld, S. V. Fomin, Ya. G. Sinai, *Ergodic Theory* (Springer, New York, 1982).

[21] M. Queffélec, *Substitution Dynamical Systems – Spectral Analysis*, Lecture Notes in Mathematics, **1294** (Springer, Berlin, 1987).

[22] H. Broer, F. Takens, Mixed spectra and rotational symmetry, Arch. Rational Mech. Anal. **124**, 13–42 (1993).

[23] R. Ketzmerick, G. Petschel, T. Geisel, Slow decay of temporal correlations in quantum systems with Cantor spectra, Phys. Rev. Lett. **69**, 695–698 (1992).

[24] M. Holschneider, Fractal wavelet dimensions and localization, Commun. Math. Phys. **160**, 457–473 (1994).

[25] K. A. Makarov, Asymptotic expansions for Fourier transform of singular self-affine measure, J. Math. Anal. Appl. **187**, 259–286 (1994).

[26] G. Z. Gershuni, E. M. Zhukhovitsky, *Convective Stability of Incompressible Fluid* (Keter Press, Jerusalem, 1976).

[27] V. S. Afraimovich, V. V. Bykov, L. P. Shilnikov, On the appearance and the structure of the Lorenz attractor, Sov. Phys. Doklady **22**, 253–255 (1977).

[28] C. Sparrow, *The Lorenz Equations: Bifurcations, Chaos, and Strange Attractors* (Springer, Berlin, 1982).

[29] M. J. Feigenbaum, The transition to aperiodic behaviour in turbulent systems, Comm.Math.Phys. **77**, 65–86 (1980).

[30] M. A. Zaks, Scaling properties and renormalization invariants for the "homoclinic quasi-periodicity", Physica D **62**, 300–316 (1993).

[31] Z. Cheng, R. Savit, R. Merlin, Structure and electronic properties of Thue-Morse lattices, Phys. Rev. B **37**, 4375–4382 (1988).

[32] F. Axel, H. Terauchi, High-resolution X-ray-diffraction spectra of Thue-Morse GaAs-AlAs heterostructures: towards a novel description of disorder, Phys. Rev. Lett. **66**, 2223–2226 (1991).

[33] M. Combescure, Recurrent versus diffusive dynamics for a kicked quantum system, J. Stat. Phys. **62**, 779–791 (1991).

[34] A. N. Kolmogorov, On dynamical systems with an integral invariant on a torus, Dokl. Akad. Nauk SSSR Ser. Mat. **93**, 763–766 (1953).

[35] A. S. Pikovsky, Evolution of the power spectrum in the period doubling route to chaos, Radiophys. Quantum Electr. **29**, 1076–1083 (1986).

[36] J. von Neumann, Zur Operatorenmethode in der klassischen Mechanik, Ann. Math. **33**, 587–642 (1932).

[37] A. V. Kochergin, Nondegenerate saddle-points and absence of mixing, Math. Notes **19**, 453–468 (1976).

[38] Ya. G. Sinai, K. M. Khanin, Mixing for certain classes of special flows over the circle shift, Func. Anal. and Appl. **26**, 155 (1992).

[39] M. Keane, Generalised Morse sequences, Z. Wahr. **10**, 335–353 (1968).

[40] K. Mahler, On the translation properties of a simple class of arithmetical functions, J. Math. and Phys. **6**, 158–163 (1926).

[41] C. R. de Oliveira, Numerical study of the long-time behaviour of quantum systems driven by Thue-Morse forces. Application to two-level systems, Europhys. Lett. **31**, 63–68 (1995).

[42] A. van Enter, J. Miękisz, Breaking of periodicity at positive temperatures, Commun. Math. Phys. **134**, 647–651 (1990).

[43] C. Gardner, J. Miękisz, C. Radin, A. van Enter, Fractal symmetry in an Ising model, J. Phys. A: Math.Gen. **22**, L1019–L1023 (1989).

[44] J. M. Luck, Critical behavior of the aperiodic quantum Ising chain in a transverse magnetic field, J. Stat. Phys. **72**, 417–458 (1993).

[45] L. Turban, F. Igloi, B.Berche, Surface magnetization and critical behavior of aperiodic Ising quantum chains, Phys. Rev. B **49**, 12695–12702 (1994).

[46] F. Igloi, P. Lajko, Surface magnetization and surface correlations in aperiodic Ising models, J. Phys. A: Math., Gen. **29**, 4803–4814 (1996).

[47] J. Peyrière, E. Cockayne, F. Axel, Spectra of finite-size Thue-Morse GaAs-AlAs multilayer heterostructures, J. de Phys. I **5**, 111–128 (1995).

[48] A. Bovier, J.-M. Ghez, Remarks on the spectral properties of tight-binding and Kronig-Penney models with substitution sequences, J. Phys. A: Math., Gen. **28**, 2313–2324 (1995).

[49] A. S. Pikovsky, M. A. Zaks, U. Feudel, J. Kurths, Singular continuous spectra in dissipative dynamical systems, Phys. Rev. E **52**, 285–296 (1995).

[50] C. Godrèche, J. M. Luck, Multifractal analysis in reciprocal space and the nature of the Fourier transform of self-similar structures, J. Phys. A: Math., Gen. **23**, 3769–3797 (1990).

[51] E. Liviotti, A study of the structure factor of Thue-Morse and period-doubling chains by wavelet analysis, J. Phys. Condens. Matter **8**, 5007–5015 (1996).

[52] C.-A. Guerin, M. Holschneider, On equivalent definitions of the correlation dimension for a probability measure, J. Stat. Phys. **86**, 707–720 (1997).

[53] N. Wiener, The spectrum of an array, J. Math. and Phys. **6**, 145–157 (1926).

[54] M. Kolar, New class of one-dimensional quasicrystals, Phys. Rev. B **26**, 5489–5492 (1993).

[55] M. Kolar, B. Iochum, L. Raymond, Structure factor of 1D systems (superlattices) based on two-letter substitution rules, J. Phys. A: Math., Gen. **26**, 7343–7366 (1993).

[56] A. Chakrabarti, S. N. Karmakar, R. K. Moitra, Role of a new type of correlated disorder in extended electronic states in the Thue-Morse lattice, Phys. Rev. Lett. **74**, 1403–1406 (1995).

[57] M. A. Zaks, A. S. Pikovsky, J. Kurths, On the correlation dimension of the spectral measure for the Thue-Morse sequence, J. Stat. Phys. **88**, 1387–1392 (1997).

[58] E. N. Lorenz, Deterministic nonperiodic flow, J. Atmos. Sci., **20**, 130–141 (1963).

[59] J.-P. Eckmann, H. Epstein, Bounds on the unstable eigenvalue for period doubling, Comm. Math. Phys. **128**, 427–435 (1990).

[60] P. Collet, J.-P. Eckmann, *Iterated Maps on the Interval as Dynamical System* (Birkhäuser, Basel, 1980).

[61] M. J. Feigenbaum, Quantitative universality for a class of nonlinear transformations, J. Stat. Phys., **19**, 25 (1978).

[62] E. Bombieri, J. Taylor, Which distributions of matter diffract ? An initial investigation, J. Phys., Colloq. **C3**, **47**, C3-19 – C3-28 (1986).

[63] R. Artuso, D. Belluzzo, C. Casati, Thermodynamic analysis of the spectral measure for kicked quantum-systems, Europhys. Lett. **25**, 181–186 (1994).

[64] A. V. Kochergin, On mixing in special flows over translation of intervals and in smooth flows on surfaces, Math. Sbornik **96**, 471–502 (1975).

[65] M. A. Zaks, A. S. Pikovsky, J. Kurths, Steady viscous flow with fractal power spectrum, Phys. Rev. Lett. **77**, 4338–4341 (1996).

[66] J. H. Misguich, R. Nakach, Guiding center chaotic motion in three electrostatic waves, Phys. Rev. A **44** 3869–3888 (1991).

[67] G. Petschel, T. Geisel, Unusual manifold structure and anomalous diffusion in a Hamiltonian model for chaotic guiding center motion, Phys. Rev. A **44** 7959–7967 (1991).

[68] S. H. Strogatz, C. M. Markus, R. M. Westervelt, R. E. Mirollo, Collective dynamics of coupled oscillators with random pinning, Physica D **36** 23–50 (1989).

[69] A. I. Khibnik, Y. Braiman, T. A. B. Kennedy, K. Wiesenfeld, Phase model analysis of two lasers with injected field, Physica D **111**, 295–310 (1998).

[70] M. D. Shklover, On dynamical systems on a torus with continuous spectrum, Izv. Vyssh. Uchebn. Zaved. Mat. 10, 113–124 (1967).

[71] A. V. Kochergin, On the absence of mixing for special flows over rotations on the circle and for flows on the two-dimensional torus, Sov.Math.Dokl. **13**, 949–952 (1972).

[72] T. M. Cherry, Analytic quasi-periodic curves of discontinuous type on a torus, Proc. London Math. Soc. **44**, 175–215 (1938).

[73] J. Palis, W. de Melo, *Geometric theory of dynamical systems: An introduction*, (Springer, New York,1982)

[74] I. Nikolaev, E. Zhuzhoma, Flows on 2-dimensional manifolds, Lecture Notes in Mathematics, **1705** (Springer, Berlin, 1999).

[75] C. Baesens, J. Guckenheimer, S. Kim, R. S. MacKay, Three Coupled Oscillators: Mode-locking, Global Bifurcations and Toroidal Chaos, Physica D **49**, 387–475 (1991).

[76] M. Reed, B. Simon, *Methods of modern mathematical physics*, Academic Press, NY, 1972.

[77] M. A. Zaks, A. S. Pikovsky, J. Kurths, On the generalized dimensions for the Fourier spectrum of the Thue-Morse sequence, J. Phys. A: Math.Gen. **32**, 1523–1530 (1999).

[78] C. Boyd, On the structure of the family of Cherry fields on the torus, Ergod. Th. & Dynam. Sys. **5**, 27–46 (1985).

[79] J. J. P. Veerman, Irrational rotation numbers, Nonlinearity **2**, 419–428 (1989).

[80] J. Graczyk, L. B. Jonker, G. Świątek, F. M. Tangerman, J. J. P. Veerman, Differentiable circle maps with a flat interval, Commun. Math. Phys. **173**, 599–622 (1995).

[81] P. Glendinning, Bifurcations and rotation numbers for maps of the circle associated with flows on the torus and models of cardiac arrhythmias, Dynam. Stability Systems **10**, 367–386 (1995).

[82] M. A. Zaks, A. S. Pikovsky, J. Kurths, Symbolic dynamics behind the singular continuous power spectra of continuous flows, Physica D **117**, 77–94 (1998).

[83] E. Zeckendorf, Répresentation des nombres naturels par une somme des nombres de Fibonacci ou de nombres de Lucas, Bull. Soc. Roy. Sci. Liège **41**, 179–182 (1972).

[84] D. Rand, S. Ostlund, J. Sethna, E. Siggia, Universal properties of the transition from quasi-periodicity to chaos in dissipative systems, Physica D **8**, 303–342 (1982).

[85] J. P. Gollub, H. L. Swinney, Onset of turbulence in a rotating fluid, Phys. Rev. Lett., **35**, 927–930 (1975).

[86] J. P. Gollub, S. V. Benson, Many routes to turbulent convection, J. Fluid Mech., **100**, 449–470 (1980).

[87] W. de Melo, On the cyclicity of recurrent flows on surfaces, Nonlinearity **10**, 311–319 (1997).

[88] H. Aref, Stirring by chaotic advection, J. Fluid Mech. **143**, 1–21 (1984).

[89] J. M. Ottino, *The kinematics of mixing: stretching, chaos and transport* (University Press, Cambridge, 1989).

[90] N. F. Bondarenko, M. Z. Gak, F. V. Dolzhansky, Laboratory and theoretical models of a plane periodic flow, Izvestiya, Atmos. Ocean Phys., **15**, 1017–1026 (1979).

[91] J. Sommeria, Experimental study of the two-dimensional inverse energy cascade in a square box, J. Fluid Mech. **170**, 139–168 (1986).

[92] O. Cardoso, D. Marteau, P. Tabeling, Quantitative experimental study of the free decay of quasi-two-dimensional turbulence, Phys. Rev. E, **49**, 454–461 (1994).

[93] L. D. Meshalkin, Ya. G. Sinai, Investigation of the stability of a stationary solution of a system of equations for the plane movement of an incompressible viscous liquid, J. Appl. Math. Mech. (Prikl. Mat. Mekh.), **25**, 1700–1705 (1961).

[94] A. A. Nepomnyaschy, On the stability of secondary flows of the viscous fluid in the unbounded space, J. Appl. Math. Mech. (Prikl. Mat. Mekh.), **40**, 836–841 (1976).

[95] J. Guckenheimer, P. Holmes, *Nonlinear oscillations, dynamical systems and bifurcations of vector fields* (Springer, New York, 1983)

[96] S. Jana, G. Metcalfe, J. Ottino, Experimental and computational studies of mixing in complex Stokes flows: the vortex mixing flow and multicellular cavity flows, J. Fluid Mech. **269**, 199–246 (1994).

[97] V. I. Arnold, Topological and ergodic properties of closed 1-Forms with incommensurable periods, Func. Anal. and Appl. **25**, 81–90 (1991).

[98] J. Crutchfield, M. Nauenberg, J. Rudnick, Scaling for external noise at the onset of chaos, Phys. Rev. Lett. **46**, 933–935 (1981).

[99] B. Shraiman, C. E. Wayne, P. C. Martin, Scaling theory for noisy period-doubling transitions to chaos, Phys. Rev. Lett. **46**, 935–939 (1981).

[100] A. Hamm and R. Graham, Scaling for small random perturbations of golden critical circle maps, Phys. Rev. A **46**, 6323–6333 (1992).

[101] R. Badii, A. Politi, *Complexity: hierarchical structures and scaling in physics* (Cambridge University Press, Cambridge, 1997).

[102] W. Ebeling, J. Freund, F. Schweitzer, *Komplexe Strukturen: Entropie und Information* (B. G. Teubner, Stuttgart, Leipzig, 1998).

[103] B. Derrida, A. Gervois, Y. Pomeau, Universal metric properties of bifurcations of endomorphisms, J. Phys. A: Math., Gen. **12**, 269 (1979).

[104] J. Freund, W. Ebeling, K. Rateitschak, Self-similar sequences and universal scaling of dynamical entropies, Phys. Rev. E, **54**, 5561–5566 (1996).

[105] J. Freund, K. Rateitschak, Entropy analysis of noise contaminated sequences, Int. J. Bifurcation and Chaos **8**, 933–940 (1998).

[106] U. Frisch, G. Parisi, On the similarity structure of fully developed turbulence. In: *Turbulence and predictability in geophysical fluid dynamics and climate dynamics*, Edited by M. Ghil *et al*, 84 (North-Holland, NY, 1985).

[107] T. C. Halsey, M. H. Jensen, L. P. Kadanoff, I. Procaccia, B. I. Shraiman, Fractal measures and their singularities: The characterization of strange sets, Phys. Rev. A, **33**, 1141 (1986).

[108] H. E. Stanley, S. V. Buldyrev, A. L. Goldberger, S. Havlin, C.-K. Peng, M. Simons, Long-range power-law correlations in condensed matter physics and biophysics, Physica A **200**, 4–24 (1993).

[109] J. M. Hausdorff, C.-K. Peng, Z. Ladin, J. Wei, A. Goldberger, Is walking a random walk ? Evidence for long-range correlations in stride interval of human gait, J. Appl. Physiol. **78**, 349–358 (1995).

[110] M. Duarte, V. Zatsiorsky, Long-range correlations in human standing, Phys. Lett. A **283**, 124–128 (2001).

[111] E. Koscielny-Bunde, A. Bunde, S. Havlin, H. E. Roman, Y.Goldreich, H.-J. Schellnhuber, Indication of a universal persistence law governing atmospheric variability, Phys. Rev. Lett. **81**, 729–731 (1998).

[112] R. B. Govindan, D. Vjushin, S. Brenner, A. Bunde, S. Havlin, H.-J. Schellnhuber, Long-range correlations and trends in global climate models: comparison with real data, Physica A **294**, 239–248 (2001).

[113] C.-K. Peng, S. V. Buldyrev, A. L. Goldberger, S. Havlin, F. Sciortino, M. Simons, H. E. Stanley, Long-range correlations in nucleotide sequences, Nature **356**, 168–170 (1992).

[114] W. Li, K. Kaneko, Long-range correlation and partial $1/f^{\alpha}$ spectrum in a noncoding DNA sequence, Europhys. Lett. **17**, 655–660 (1992).

[115] W. Li, R. Marr, K. Kaneko, Understanding long-range correlations in DNA sequences, Physica D **75**, 392–416 (1992).

[116] A. Arneodo, E. Bacry, P. Graves, J. Muzy, Characterizing long-range correlations in DNA sequences from wavelet analysis, Phys. Rev. Lett. **74**, 3293–3296 (1995).

[117] B. Audit, C. Thermes, C. Vaillant, Y. d'Auberon-Carafa, J. F. Muzzy, A. Arneodo, Long-range correlations in genomic DNA: a signature of the nucleosomal structure, Phys. Rev. Lett. **86**, 2471–2474 (2001).

[118] W. Li, Spatial $1/f$ spectra in open dynamical systems, Europhys. Lett. **10**, 395–400 (1989).

[119] W. Li, Expansion-modification systems: a model for spatial $1/f$ spectra, Phys. Rev. A **43**, 5240–5260 (1991).

[120] V. R. Chechetkin, A. Yu. Turygin, On the spectral criteria of disorder in non-periodic sequences: application to inflation models, symbolic dynamics and DNA sequences, J. Phys. A: Math. Gen. **27**, 4875–4898 (1994).

[121] H. Herzel, I. Große, Correlations in DNA sequences: the role of protein coding segments, Phys. Rev. E **55**, 800–809 (1997).

[122] M. A. Zaks, Fractal Fourier spectra of Cherry flows, Physica D **149** (2001), 237–247 (2001).

[123] M. A. Zaks, Multifractal Fourier spectra and power-law decay of correlations in random substitution sequences, Phys. Rev. E **65** (2002), 011111, 1–5.

[124] M. A. Zaks, Influence of noise on dynamics with fractal Fourier spectra, Physica A **310** (2002), 285–307.